

NOCTURNAL PROCESSING OF NITROGEN OXIDE POLLUTION AT HIGH
LATITUDES: OFF-AXIS CAVITY RING-DOWN SPECTROSCOPY METHOD
DEVELOPMENT AND FIELD MEASUREMENT RESULTS

A
THESIS

Presented to the Faculty
of the University of Alaska Fairbanks

In Partial Fulfillment of the Requirements

For the Degree of

DOCTOR OF PHILOSOPHY

By

Randy Lee Apodaca, M.S.

Fairbanks, Alaska

August 2008

UMI Number: 3337639

INFORMATION TO USERS

The quality of this reproduction is dependent upon the quality of the copy submitted. Broken or indistinct print, colored or poor quality illustrations and photographs, print bleed-through, substandard margins, and improper alignment can adversely affect reproduction.

In the unlikely event that the author did not send a complete manuscript and there are missing pages, these will be noted. Also, if unauthorized copyright material had to be removed, a note will indicate the deletion.

UMI[®]

UMI Microform 3337639

Copyright 2009 by ProQuest LLC.

All rights reserved. This microform edition is protected against unauthorized copying under Title 17, United States Code.

ProQuest LLC
789 E. Eisenhower Parkway
PO Box 1346
Ann Arbor, MI 48106-1346

NOCTURNAL PROCESSING OF NITROGEN OXIDE POLLUTION AT HIGH
LATITUDES: OFF-AXIS CAVITY RING-DOWN SPECTROSCOPY METHOD
DEVELOPMENT AND FIELD MEASUREMENT RESULTS

By

Randy Lee Apodaca, M.S.

RECOMMENDED:









Advisory Committee Chair



Chair, Department of Chemistry and Biochemistry

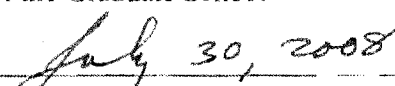
APPROVED:



Dean, College of Natural Science and Mathematics



Dean of the Graduate School



Date

July 30, 2008

Abstract

Nitrogen oxides, or NO_x , play a central role in ozone and nitric acid (HNO_3) pollution in the troposphere. Reactions of nitrate radical (NO_3) and dinitrogen pentoxide (N_2O_5) result in the removal of NO_x and ozone from the nighttime atmosphere. In this thesis, we describe the configuration, operation, and performance of an off-axis cavity ring-down spectroscopy (oa-CRDS) field instrument designed for measuring NO_3 and N_2O_5 . Furthermore, we report results of an N_2O_5 instrument intercomparison conducted using an atmospheric simulation chamber in Jülich, Germany. The results of the intercomparison demonstrate that the oa-CRDS instrument is an excellent tool for measuring NO_3 and N_2O_5 . Also reported in this thesis are the results of two field campaigns aimed at characterizing NO_x removal from the nocturnal pollution plume arising from Fairbanks, AK. The results from the field campaigns suggest ice is responsible for catalyzing N_2O_5 heterogeneous hydrolysis in cold, high-latitude plumes. When air masses are sub-saturated with respect to ice, the data show longer lifetimes (~ 20 minutes) and elevated N_2O_5 levels while ice-saturated air masses show shorter lifetimes (~ 6 minutes) and suppressed N_2O_5 levels. Lastly, we present vertical profiles of N_2O_5 measured above the seasonal snow pack. The results of the profiling studies suggest that N_2O_5 can be removed by heterogeneous hydrolysis on ice in the snow pack. Our findings indicate that catalysis on ice surfaces is largely responsible for nocturnal processing of N_2O_5 leading to nitric acid production and loss of NO_x in high latitude plumes.

Table of Contents

	Page
Signature Page	i
Title Page	ii
Abstract	iii
Table of Contents	iv
List of Figures	viii
List of Tables	x
List of Appendices	xi
Acknowledgements	xii
Chapter 1 Atmospheric nitrogen oxide chemistry and measurement techniques	1
1.1 Introduction	1
1.2 NO _x oxidation in the troposphere	4
1.3 NO ₃ and N ₂ O ₅ Observation Techniques	7
1.4 Statement of purpose	11
1.5 References	14
Chapter 2 The configuration and operation of the NO₃-N₂O₅ field instrument	18
2.1 Introduction	18
2.2 The NO ₃ -N ₂ O ₅ Field instrument	19
2.2.1 Measuring NO ₃ and N ₂ O ₅ with oa-CRDS	19
2.2.2 NO ₃ absorption cross sections	21
2.2.3 Field instrument configuration	23

	Page
2.2.4 Chemical zeroing	27
2.3 NO ₃ and N ₂ O ₅ sampling losses	30
2.4 Final field data reduction	33
2.4.1 Bypass manifold loss correction for Spring 2007 campaign	34
2.4.2 Conversion of ambient measurements to mixing ratios.....	35
2.4.3 Correction to the NO ₃ data from the instrument intercomparison.....	36
2.5 Performance of the oa-CRDS field instrument.....	38
2.6 Conclusions.....	39
2.7 References.....	41
Chapter 3 Intercomparison of two N₂O₅ field instruments	42
3.1 Introduction.....	42
3.2 Experiment.....	45
3.2.1 Instrument descriptions.....	45
3.2.1.1 The UAF oa-CRDS field instrument	46
3.2.1.2 The NOAA CaRDS field instrument	47
3.2.2 The SAPHIR chamber	47
3.2.3 Chamber experiments	49
3.3 Results and discussion	50
3.3.1 UAF-NOAA Intercomparison	50
3.3.2 Initial 2 hour data	56
3.3.3 Instrument accuracy and detection sensitivities.....	58

	Page
3.4 Conclusions.....	60
3.5 References.....	63
Chapter 4 The role of ice in N₂O₅ heterogeneous hydrolysis at high latitudes	66
4.1 Introduction.....	66
4.2 Measurements	69
4.3 Nocturnal nitrogen oxide partitioning.....	72
4.4 Steady state lifetimes and other considerations	73
4.5 Results.....	74
4.6 Discussion.....	76
4.6.1 Validity of the steady state approximation	76
4.6.2 Loss of N ₂ O ₅ and relative humidity with respect to ice.....	79
4.6.3 Loss of N ₂ O ₅ with respect to aerosol particles.....	85
4.7 Conclusions and atmospheric implications.....	89
4.8 References.....	92
Chapter 5 Vertical profiles of N₂O₅ in the Fairbanks pollution plume	96
5.1 Introduction.....	96
5.2 Experimental.....	98
5.3 Results.....	100
5.4 Ratios of N ₂ O ₅ levels at 1 m and 4 m	102
5.5 Conclusions.....	106
5.6 References.....	109

	Page
Chapter 6 Conclusions and future outlook	110
6.1 High latitude nocturnal nitrogen oxide oxidation.....	110
6.2 References.....	116
Appendices	117

List of Figures

	Page
Fig. 1.1 Simplified illustration of the “light” and “dark” NO _x oxidation pathways.....	4
Fig. 2.1 Examples of cavity ring-down spectroscopy.....	19
Fig. 2.2 Example NO ₃ absorption cross section	23
Fig. 2.3 The NO ₃ -N ₂ O ₅ field instrument	25
Fig. 2.4 Example of baseline determination by chemical zeroing with nitric oxide	28
Fig. 2.5 Example of a flow experiment that was conducted during the Fall 2007 field campaign and used for determining $E(ts)$	32
Fig. 3.1 Photograph of the SAPHIR atmospheric simulation chamber	48
Fig. 3.2 Selected data from the UAF and NOAA instruments on 10, 15, 16 June.....	51
Fig. 3.3 A plot of filter transmission against filter age.....	53
Fig. 3.4 UAF vs NOAA correlations plots	55
Fig. 3.5 Correlation plots of the initial 2 hours of the experiments conducted on 10, 15, and 16 June	57
Fig. 3.6 Correlation of the combined 2 hour data set for all 12 experimental days	58
Fig. 3.7 Histograms of N ₂ O ₅ measurements made subsequent to the chamber being purged with zero air, precluding significant levels of N ₂ O ₅	59
Fig. 4.1 A satellite image showing the study site location and its relationship to Fairbanks and the surrounding area	70
Fig. 4.2 Time series of N ₂ O ₅ , NO, NO ₂ , and ozone mixing ratios from the campaign ...	75
Fig. 4.3 N ₂ O ₅ steady state lifetimes, source rates, and mixing ratios for two representative periods of the campaign.....	77
Fig. 4.4 N ₂ O ₅ abundance and relative humidity with respect to ice	80
Fig. 4.5 The dependence of $\tau(N_2O_5)$ on relative humidity with respect to ice	81

	Page
Fig. 4.6 Normalized histograms of $\tau(\text{N}_2\text{O}_5)$	82
Fig. 4.7 Timeseries of N_2O_5 mixing ratios and aerosol properties	86
Fig. 4.8 The relationship between aerosol surface area N_2O_5 and lifetime	88
Fig. 5.1 Examples of vertical gradients in O_3 , NO_3 , and N_2O_5 adapted from Brown et al.(2007a)	97
Fig. 5.2 Study site and experimental set up	99
Fig. 5.3 N_2O_5 vertical profiles	101
Fig. 5.4 An example of the temperature difference between the 1 m and 4 m elevations taken from the profiling study conducted on 30 March 2007.....	104
Fig. 5.5 The relationship between the average ratio of N_2O_5 and the average temperature difference measured at the two elevations	105
Fig. 5.6 The relationship between the average ratio of N_2O_5 and the average temperature measured during the individual profiling experiments	105
Fig. 5.7 The relationship between the average ratio of N_2O_5 and the overall average N_2O_5 abundance measured during the individual profiling studies	106
Fig. 6.1 Annual relative humidity with respect to ice in Fairbanks, AK.....	112
Fig. A-1 (a) A photograph of the off-axis CRDS instrument.....	125
Fig. A-2 Measured $\text{NO}_3+\text{N}_2\text{O}_5$ mixing ratios as a function of time (given in fractional day of year, noon 1 Jan 05 AKDT = fdoy 1.50)	126
Fig. A-3 Correlation between measurements made with oa-CRDS (bottom axis) and cw-CRDS (left axis).....	127

List of Tables

	Page
Table 3.1 Experimental conditions and chemical composition of the chamber volume during the intercomparison exercise	50
Table 3.2 Results of the correlations and regression from the 12 experimental days.....	52
Table 3.3 Results of the correlations and regression from the initial 2 hours of each experiment.....	57
Table 5.1 A summary of the average ratio of N ₂ O ₅ (1 m:4 m) for the nightly profiling studies	103

List of Appendices

	Page
Appendix A Off-axis cavity ring-down spectroscopy: Application to atmospheric nitrate radical detection	117
Appendix B Copyright permission letters	128

Acknowledgements

My sincere appreciation goes to my advisor and scientific mentor Professor William Simpson. I am extremely fortunate to have studied atmospheric chemistry under his guidance and to have benefited from his knowledge in our field and beyond. I would also like to acknowledge Professors Catherine Cahill, Thomas Trainor, and Falk Huettmann for providing guidance throughout my time at UAF and for serving on my graduate committee. I am also very fortunate to have received guidance from Professor James Ayers, whom I consider a mentor and a great friend. Special appreciation is due to Deanna Huff, who assisted invaluablely in collecting the NO_x, ozone, and aerosol data presented in chapter 4 of this thesis. My warmest appreciation and affection is offered to my wife Kendra, who assisted in proof-reading various drafts of this thesis, tolerated my absenteeism during field campaigns and writing sessions, and always possessed the ability to put a smile on my face; all while carrying our first child. I am grateful.

This work was supported by the National Science Foundation (Grants CHE-0094038 and ATM-0624448), as well as by the United States Department of Energy (Grant DE-FG02-03ER83695).

Chapter 1:

Atmospheric nitrogen oxide chemistry and measurement techniques

1.1 Introduction

Air pollution and the role it plays in climate and ecological change are of increasing concern as anthropogenic pollution sources continue to proliferate in both abundance and geographical coverage. Many chemical species contribute to the atmospheric pollution problem, but NO_x ($= \text{NO} + \text{NO}_2$) is arguably one of the most influential species of the atmospheric pollutants (Finlayson-Pitts and Pitts, 2000). The United States Environmental Protection Agency lists NO_x as one of its six criteria pollutants, meaning that NO_x emissions are regulated to permissible levels determined by science-based guidelines. The goal of regulating criteria pollutants is to minimize their health and environmental impacts. The detrimental health and environmental impacts associated with NO_x pollution are manifest in its contributions to the production of photochemical ozone (O_3) and nitric acid (HNO_3) in the troposphere (Andersen and Hovmand, 1995; Heintz et al., 1996; Allan et al., 1999; Finlayson-Pitts and Pitts, 2000).

Ozone plays a significant role in the oxidizing capacity of the troposphere and contributes strongly to diminishing air quality. Ozone is a strong respiratory irritant and has been shown to cause decreases in crop yield and could potentially cause declines in global food quality and supply by damaging tissues in plants (Chameides, 1989; McDonnell, 2001; Walker, 2001; Vollenweider et al., 2003). Additionally, tropospheric ozone has been found to significantly contribute to climate forcing that perturbs the

Earth's energy balance and influences current trends in global warming (Hansen and Sato, 2001).

Nitric acid deposition is the consequence of removal of NO_x from the atmosphere. Nitric acid is a significant contributor to acid rain and subsequently leads to acidification of surface waters and soils, harming biota residing in such ecosystems (Andersen and Hovmand, 1995; Bergholm et al., 2003). Nitric acid can also directly damage foliage and property through direct wet or dry deposition processes, and, maybe more importantly, the deposition of nitric acid can act as a source of fixed nitrogen. Thus, nitric acid can serve as a potent fertilizer in nitrogen-limited regions, particularly in sensitive ecosystems found at high latitudes. Ultimately, nitric acid deposition can alter plant species abundance and composition, subsequently affecting change in wildlife habitat and biodiversity as a whole (Fenn et al., 2003).

Anthropogenic sources of NO_x , primarily from fossil fuel combustion and biomass burning, are 5-10 times higher than natural sources (Wayne et al., 1991). Because industrialized nations have a strong dependence on fossil fuel combustion as a primary energy source, NO_x emissions are not likely to decline appreciably in the foreseeable future. Therefore, it is important to understand the transformation of NO_x to nitric acid and how the products of this transformation affect health and environmental change. Two important intermediates in the oxidation of NO_x to nitric acid are the nitrate radical (NO_3) and dinitrogen pentoxide (N_2O_5). In recent years, technological advances have allowed the detection of NO_3 and N_2O_5 at ambient levels. Platt et al. (1980) first measured NO_3 in polluted air masses near Los Angeles, and, since this time, a growing

number of studies have been aimed at characterizing the role of NO_3 and N_2O_5 in the NO_x oxidation process.

The large majority of these studies have been conducted at lower latitudes.

Brown and co-workers have constructed an extensive body of work examining the spatial distribution of NO_3 and N_2O_5 in the atmosphere, as well as the efficiency with which reactions of NO_3 and N_2O_5 remove NO_x from the nighttime atmosphere in urban, rural, and marine environments (Brown et al., 2003; 2004; 2005; 2006; Aldener et al., 2006; Osthoff et al., 2006). Additionally, works by Wood et al. (2003; 2005) conducted in the San Francisco Bay Area, Matsumoto et al. (2005) and Nakayama et al. (2008) conducted in Japan, are 3 recent examples of a growing number of studies aimed at examining ambient N_2O_5 abundances and lifetimes in locations around the world. Until two recent studies (Simpson, 2003; Ayers and Simpson, 2006), N_2O_5 abundances and lifetimes had not been reported for high latitudes, leaving a considerable gap in the understanding of the NO_x oxidation process in cold regions.

The motivation of this work was to fill that gap by investigating the mechanisms controlling NO_x oxidation in high latitude pollution plumes. Secondly, we wanted to elucidate the roles that NO_3 and N_2O_5 play in that process. Following this general introduction, the relevant reactions that result in the formation and removal of NO_x are outlined. Additionally, we briefly describe the history of instrumentation designed for probing the role of NO_3 and N_2O_5 in atmospheric NO_x chemistry. Lastly, we define the specific goals of this work and outline the chapters of this thesis.

After the conversion of NO to NO₂, there are two possible pathways for the completion of the oxidation process. One pathway, referred to as the “light” oxidation pathway, occurs in the presence of sunlight (fig 1.1, top panel). Daytime NO_x removal is primarily driven by the presence of the hydroxyl radical (OH) in the reaction



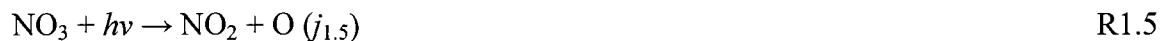
where M is a third body. Most of the resultant HNO₃ is removed from the atmosphere by wet or dry deposition.

The second pathway occurs in the absence of daylight and is termed the nocturnal or “dark” NO_x oxidation pathway (fig. 1.1, bottom panel). This dark pathway results in the formation of NO₃ and N₂O₅ through the reactions:



NO₃, formed in reactions R1.2 and R1.4, is a potent oxidizer and controls the fate of many compounds in the nighttime atmosphere (Heintz et al., 1996; Allen et al, 1999). Oxidation of organic compounds via the nitrate radical generates various organic free radicals and, subsequently, produces the hydroxyl radical in the absence of daylight (Finlayson-Pitts and Pitts, 2000). Therefore, the nitrate radical directly and synergistically enhances the oxidation potential of the nighttime atmosphere (Wayne et al., 1991).

Daytime formation of NO₃ in reaction R1.2 is of little consequence because NO₃ undergoes rapid photolysis through the reactions:



Orlando et al. (1993) estimated a daytime lifetime of only 5 s for NO_3 with an overhead sun and a clear sky at sea level.

At typical nighttime NO_3 mixing ratios, ranging from a couple of parts per trillion by volume (pptv) to several hundred pptv, NO_3 lifetimes have been reported to range from less than one minute to more than 100 minutes (Allen et al, 1999; Wood et al., 2005; Ayers and Simpson, 2006; Brown, 2006). The most common NO_3 sinks include reaction with NO (to form 2 NO_2), reaction with volatile organics (such as alkenes), or conversion to N_2O_5 by reaction with NO_2 as illustrated above (Wayne et al., 1991).

Reactions R1.2 through R1.6 demonstrate the critical role that the nitrate radical plays in the production of several atmospheric pollutants. First, Reaction R1.2 not only forms NO_3 , but also demonstrates that NO_x can act as a sink for ozone in the nighttime atmosphere. Reaction R1.3 indicates that, upon its formation in the nighttime atmosphere, NO_3 rapidly establishes equilibrium with NO_2 and N_2O_5 . Reaction R1.3 also illustrates the important role that NO_3 plays in the nighttime removal of NO_x to reservoirs of nitrogen oxides. Typical nighttime N_2O_5 mixing ratios range from sub-pptv to a few ppbv (parts per billion by volume), and the N_2O_5 lifetimes can range from sub-minute to greater than 400 minutes (Ayers and Simpson, 2006; Brown et al., 2006; Nakayama et al., 2008). It is important to note that reaction R1.3 is the only known source of N_2O_5 .

The equilibrium between NO_3 and N_2O_5 is strongly dependent on temperature and NO_2 levels. Elevated pollution levels (~5 ppbv NO_2) and colder temperatures favor the

formation of N_2O_5 (reaction R1.3) while warmer temperatures favor NO_3 (reaction R1.4). The decomposition of N_2O_5 from warming acts as a source of NO_3 in the absence of sunlight or as a source of NO_x during the day via reaction R1.4, followed by reactions R1.5 or R1.6. The major nighttime loss for N_2O_5 is heterogeneous hydrolysis,



Both, N_2O_5 as well as HNO_3 , are readily removed from the atmosphere via wet and dry deposition processes, indicating that reaction R1.7 ultimately serves as the terminal step in the nocturnal NO_x oxidation process. The influential modeling study by Dentener and Crutzen (1993) suggests that the dark oxidation pathway is the predominant NO_x removal mechanism during high latitude winters. Furthermore, their modeling study suggests that the nocturnal removal of NO_x from the atmosphere would reduce the production of O_3 by up to 25 percent and serve as a significant source of fixed nitrogen as the result of nitric acid deposition.

1.3 NO_3 and N_2O_5 Observation Techniques

Until recently, NO_3 mixing ratios were primarily determined through various applications of differential optical absorption spectroscopy or DOAS (Platt et al., 1980; Heintz et al., 1996; Allen et al., 1999; Stutz et al., 2004). This technique measures path-averaged mixing ratios of NO_3 along vertical or horizontal light paths passing through the atmosphere. Pathlengths required for DOAS are on the order of 1-15 km for detection of typical ambient NO_3 levels (typically ≤ 400 pptv). Heintz et al. (1996) utilized such an instrument to detect NO_3 on the order of 25 pptv over land, while Allen et al. (1999) utilized a similar technique to detect NO_3 mixing ratios ranging from 5 to 15 pptv in a

marine environment. The DOAS technique has repeatedly been proven robust, with advantages including reasonable sensitivity as well as capability for simultaneously measuring multiple species. The disadvantages of this technique include slow time resolution (on the order of 1 to 5 minutes) and poor spatial, both due to the required long pathlength. An additional and highly significant limitation of DOAS is the inability to detect N_2O_5 , because NO_3 does not possess a strong absorption feature in the visible spectral region.

Kleffmann et al. (2007) recently demonstrated the performance of a new instrument for measuring the sum of $\text{HNO}_3 + 2 \cdot \text{N}_2\text{O}_5$, termed the long path liquid absorption photometer or LOPAP. This method samples ambient air through a temperature controlled stripping coil, converting gas phase nitrogen species to a liquid-phase dye that is subsequently measured for the sum of $\text{HNO}_3 + 2 \cdot \text{N}_2\text{O}_5$. The LOPAP instrument has the advantage of relatively high spatial and temporal resolution. Furthermore, LOPAP demonstrates high sensitivity with a reported detection limit of 5–30 pptv for a time response of 6–2 min, respectively. The major disadvantage to LOPAP is that concurrent independent measurement of HNO_3 is required in order to derive a mixing ratio of N_2O_5 .

Improved frequency and wavelength modulation techniques in tunable diode lasers allow lasers to be smaller, cheaper, and more portable without sacrificing quality. These advances in laser technologies have led to the development of two additional techniques for probing the nocturnal NO_x oxidation pathway: optical absorbance spectroscopy and laser induced fluorescence (LIF). The primary optical absorbance

technique for NO_3 and N_2O_5 detection is termed cavity ring-down spectroscopy or CRDS (Schulz and Simpson, 1998; King et al., 2000; Ball et al., 2001; Brown et al., 2002; Simpson, 2003; Ball et al., 2004; Ayers et al., 2005; Dube' et al., 2006; Nakayama et al., 2008). Many variations exist, but in general, CRDS measures light absorption by observing the rate of light loss within an optical cavity. Cavity losses occur from mirror losses and absorption or scattering in the medium within the optical cavity. As NO_3 is a known absorber in visible wavelengths with a very strong absorption feature at 662 nm, CRDS is proving to be a highly viable technique for quantification of this radical.

Furthermore, CRDS instruments may be designed with heated inlets that allow for the quantification of ambient N_2O_5 through the thermal decomposition to NO_3 . A full description of using CRDS to determine mixing ratios of NO_3 and N_2O_5 is given in chapter 2 of this thesis. Briefly, the result of heating the sample is conversion of N_2O_5 to NO_3 which is subsequently probed with 662 nm light. Thus, the sum of $\text{NO}_3 + \text{N}_2\text{O}_5$ can be measured, which represents a critically important result for examining the nocturnal NO_x oxidation pathway. Additionally, NO_2 is formed in this thermal conversion process. However, NO_2 absorbs weakly at the detection wavelength.

By utilizing an optical cavity, CRDS achieves the long effective pathlengths (~50 km, but with short base pathlengths < 1 m) that are required for high sensitivity to NO_3 . CRDS instruments demonstrate reported detection limits ranging from less than 1.0 pptv to a few pptv, which is more than sufficient for detecting ambient NO_3 and N_2O_5 (Brown et al., 2002; Simpson, 2003; Ayers et al., 2005; Nakayama et al., 2008). Additionally, the temporal resolution can range from sub-second to a couple of seconds (versus several

minutes for DOAS and LOPAP). When CRDS instruments are constructed with small and light-weight diode lasers as the light source, they become highly portable and provide measurements with excellent spatial and temporal resolution. This is the case with the instrument we have built (see chapter 2). Furthermore, such portability allows for the measurement of NO_3 and N_2O_5 from stationary or mobile platforms.

One of the primary disadvantages of CRDS is the sensitivity to particulate matter. The ability of particulates to extinguish light within the cavity requires the filtration of sampled air at the inlet. Therefore, the reactive losses of NO_3 and N_2O_5 with the filter or particles trapped on the filter, as well as losses caused by surface reactions within the instrument, must be considered. Additionally, certain optical cavity configurations require a precise alignment. Maintaining such alignment is often a challenge in field deployment situations and considerable engineering is required to isolate vibration and prevent thermal destabilization of the cavity (King et al., 2000; Brown et al., 2002; Simpson, 2003).

Finally, instruments employing LIF were also developed for detection of NO_3 and N_2O_5 (Wood et al., 2003; 2005; Matsumoto et al., 2005). In this technique, a laser is used to bring NO_3 to an excited electronic state and the subsequent spontaneous emission or fluorescence is measured. High selectivity is achieved in this technique because the compound must both absorb the chosen excitation frequencies and emit within a constrained spectroscopic window. In LIF, the detected fluorescence signal is proportional to the mixing ratio, allowing for quantification of NO_3 and N_2O_5 *via* a heated inlet.

The advantages of this technique include moderate sensitivity, with detection limits reported at about 76 pptv, high selectivity, minimal surface losses due to sampling, and moderate portability. One disadvantage to this technique is that it often requires the use of a dye-laser, increasing the costs of construction and somewhat limiting portability (as compared to the diode lasers used in some CRDS configurations). The sensitivity of LIF is limited by collisional quenching, and, therefore, LIF instruments must be operated at low pressure. Due to this collisional quenching effect, it is not likely that LIF instruments will be able to obtain the same level of sensitivity that is obtained by CRDS instruments. Furthermore, the use of large high-vacuum pumps adds considerable weight and energy consumption, making LIF instruments less portable than other techniques. Lastly, LIF requires external calibration in order to quantify ambient levels of NO_3 , a non-trivial requirement for which there are no reliable and established methods.

1.4 Statement of purpose

The fundamental purpose of this work is to investigate the nocturnal NO_x oxidation pathway in high latitude pollution plumes. Furthermore, we seek to elucidate the roles that NO_3 and N_2O_5 play in this process. Until recently, the answers to these questions have in large part been based on mathematical models and computer simulations utilizing estimated parameters because N_2O_5 had not been measurable and NO_3 measurements had not been well-resolved spatially (Dentener and Crutzen, 1993; Heintz et al., 1996). As a result, the methods of estimation were not likely to accurately reflect the spatial and temporal concentration variations of NO_3 and N_2O_5 in the atmosphere and, subsequently, not accurately predict the controls on the nocturnal NO_x

oxidation process. To achieve the over-arching goals of this project, three major components were required: 1) development of a field instrument for measuring NO_3 and N_2O_5 ; 2) validation of the performance of the field instrument; and 3) applications of the instrument to examining the nocturnal NO_x oxidation pathway.

Therefore, we developed a field instrument, utilizing off-axis cavity ring-down spectroscopy (oa-CRDS), for measuring ambient NO_3 and N_2O_5 . The first application of a prototype oa-CRDS instrument to measuring NO_3 and N_2O_5 was described in Ayers, Apodaca, Simpson, and Baer (2005). This manuscript is included in this thesis as appendix A. Subsequently, a field instrument was constructed using oa-CRDS.

With the advent of oa-CRDS technology, we improved our ability to make real-time NO_3 and N_2O_5 mixing ratio measurements with high spatial and temporal resolution. Subsequently, the oa-CRDS instrument was included in an NO_3 and N_2O_5 instrument intercomparison in Juelich, Germany. The purpose of the intercomparison was to validate the performance of all measurement techniques for NO_3 and N_2O_5 detection under a variety of atmospheric conditions as well as to increase the confidence of the atmospheric chemistry community in the ability of existing technology to measure NO_3 and N_2O_5 . Lastly, we conducted multiple field campaigns examining NO_x oxidation in the pollution plume that arises from the high latitude city of Fairbanks, Alaska.

From this body of work, novel and important insight was gained into the nocturnal NO_x oxidation pathway. We seek to make these findings available to the general scientific community by publishing them in full detail in peer-reviewed journals, and, therefore, all but the introductory and conclusions chapters of this thesis were

prepared as manuscripts for publication. Chapter 2 of this thesis describes the new oa-CRDS field instrument and the methodology used for determining NO_3 and N_2O_5 mixing ratios. Chapter 3 describes the results from the NO_3 and N_2O_5 instrument intercomparison. Lastly, chapters 4 and 5 report on results from field campaigns and describe the unique processes that govern NO_x oxidation at high latitudes. Chapter 4 is published in Atmospheric Chemistry and Physics Discussion, and chapter 3 will be submitted to the same journal, shortly.

1.5 References

- Aldener, M., Brown, S. S., Stark, H., Williams, E. J., Lerner, B. M., Kuster, W. C., Goldan, P. D., Quinn, P. K., Bates, T. S., Fehsenfeld, F. C., and Ravishankara, A. R., 2006. Reactivity and loss mechanisms of NO_3 and N_2O_5 in a polluted marine environment: Results from in situ measurements during New England air quality study 2002, *Journal of Geophysical Research-Atmospheres*, 111.
- Allan, B. J., Carslaw, N., Coe, H., Burgess, R. A., and Plane, J. M. C., 1999. Observations of the nitrate radical in the marine boundary layer, *Journal of Atmospheric Chemistry*, 33, 129-154.
- Andersen, H. V., and Hovmand, M. F., 1995. Ammonia and nitric acid dry deposition and throughfall, *Water Air and Soil Pollution*, 85, 2211-2216.
- Ayers, J. D., Apodaca, R. L., Simpson, W. R., and Baer, D. S., 2005. Off-axis cavity ringdown spectroscopy: Application to atmospheric nitrate radical detection, *Applied Optics*, 44, 7239-7242.
- Ayers, J. D., and Simpson, W. R., 2006. Measurements of N_2O_5 near Fairbanks, Alaska, *Journal of Geophysical Research-Atmospheres*, 111, D14309
Artn d14309.
- Ball, S. M., Povey, I. M., Norton, E. G., and Jones, R. L., 2001. Broadband cavity ringdown spectroscopy of the NO_3 radical, *Chemical Physics Letters*, 342, 113-120.
- Ball, S. M., Langridge, J. M., and Jones, R. L., 2004. Broadband cavity enhanced absorption spectroscopy using light emitting diodes, *Chemical Physics Letters*, 398, 68-74.
- Bergholm, J., Berggren, D., and Alavi, G., 2003. Soil acidification induced by ammonium sulphate addition in a norway spruce forest in southwest Sweden, *Water Air and Soil Pollution*, 148, 87-109.
- Brown, S. S., Stark, H., Ciciora, S. J., McLaughlin, R. J., and Ravishankara, A. R., 2002. Simultaneous in situ detection of atmospheric NO_3 and N_2O_5 via cavity ring-down spectroscopy, *Review of Scientific Instruments*, 73, 3291-3301.
- Brown, S. S., Stark, H., Ryerson, T. B., Williams, E. J., Nicks, D. K., Trainer, M., Fehsenfeld, F. C., and Ravishankara, A. R., 2003. Nitrogen oxides in the nocturnal boundary layer: Simultaneous in situ measurements of NO_3 , N_2O_5 , NO_2 , NO , and O_3 , *Journal of Geophysical Research-Atmospheres*, 108, 4299.

Brown, S. S., Dibb, J. E., Stark, H., Aldener, M., Vozella, M., Whitlow, S., Williams, E. J., Lerner, B. M., Jakoubek, R., Middlebrook, A. M., DeGouw, J. A., Warneke, C., Goldan, P. D., Kuster, W. C., Angevine, W. M., Sueper, D. T., Quinn, P. K., Bates, T. S., Meagher, J. F., Fehsenfeld, F. C., and Ravishankara, A. R., 2004. Nighttime removal of NO_x in the summer marine boundary layer, *Geophysical Research Letters*, 31.

Brown, S. S., Osthoff, H. D., Stark, H., Dube, W. P., Ryerson, T. B., Warneke, C., de Gouw, J. A., Wollny, A. G., Parrish, D. D., Fehsenfeld, F. C., and Ravishankara, A. R., 2005. Aircraft observations of daytime NO_3 and N_2O_5 and their implications for tropospheric chemistry, *Journal of Photochemistry and Photobiology a-Chemistry*, 176, 270-278.

Brown, S. S., Ryerson, T. B., Wollny, A. G., Brock, C. A., Peltier, R., Sullivan, A. P., Weber, R. J., Dube, W. P., Trainer, M., Meagher, J. F., Fehsenfeld, F. C., and Ravishankara, A. R., 2006. Variability in nocturnal nitrogen oxide processing and its role in regional air quality, *Science*, 311, 67-70.

Chameides, W. L.: The chemistry of ozone deposition to plant-leaves - role of ascorbic acid, 1989. *Environmental Science & Technology*, 23, 595-600.

Dentener, F. J., and Crutzen, P. J., 1993. Reaction of N_2O_5 on tropospheric aerosols impact on the global distributions of NO_x , O_3 , and OH, *Journal of Geophysical Research Atmospheres*, 98, 7149-7163.

Dube, W. P., Brown, S. S., Osthoff, H. D., Nunley, M. R., Ciciora, S. J., Paris, M. W., McLaughlin, R. J., and Ravishankara, A. R., 2006. Aircraft instrument for simultaneous, in situ measurement of NO_3 and N_2O_5 via pulsed cavity ring-down spectroscopy, *Review of Scientific Instruments*, 77.

Fenn, M. E., Baron, J. S., Allen, E. B., Rueth, H. M., Nydick, K. R., Geiser, L., Bowman, W. D., Sickman, J. O., Meixner, T., Johnson, D. W., and Neitlich, P., 2003. Ecological effects of nitrogen deposition in the western United States, *Bioscience*, 53, 404-420.

Finlayson-Pitts, B. J. and J. N. Pitts Jr. (2000), *Chemistry of the Upper and Lower Atmosphere*, pp. 969, Elsevier, New York.

Hansen, J. E., and Sato, M., 2001. Trends of measured climate forcing agents, *Proceedings of the National Academy of Sciences of the United States of America*, 98, 14778-14783.

Heintz, F., Platt, U., Flentje, H., and Dubois, R., 1996. Long-term observation of nitrate radicals at the tor station, Kap Arkona (Rugen), *Journal of Geophysical Research-Atmospheres*, 101, 22891-22910.

- King, M. D., Dick, E. M., and Simpson, W. R., 2000. A new method for the atmospheric detection of the nitrate radical (NO_3), *Atmospheric Environment*, 34, 685-688.
- Kleffmann, J., Gavriloaiei, T., Elshorbany, Y., Rodenas, M., and Wiesen, P., 2007. Detection of nitric acid (HNO_3) in the atmosphere using the LOPAP technique, *Journal of Atmospheric Chemistry*, 58, 131-149.
- Matsumoto, J., Kosugi, N., Imai, H., and Kajii, Y., 2005. Development of a measurement system for nitrate radical and dinitrogen pentoxide using a thermal conversion/laser-induced fluorescence technique, *Review of Scientific Instruments*, 76, 064101
Artn 064101.
- McDonnell, W. F., 2001. A method for identifying exposure-response models for the acute respiratory effects of inhaled irritants in humans: Effects of concentration, minute ventilation, and duration, *Human and Ecological Risk Assessment*, 7, 1133-1144.
- Nakayama, T., Ide, T., Taketani, F., Kawai, M., Takahashi, K., and Matsumi, Y., 2008. Nighttime measurements of ambient N_2O_5 , NO_2 , NO and O_3 in a sub-urban area, Toyokawa, Japan, *Atmospheric Environment*, 42, 1995-2006.
- Orlando, J. J., Tyndall, G. S., Moortgat, G. K., and Calvert, J. G., 1993. Quantum yields for NO_3 photolysis between 570 and 635 nm, *Journal of Physical Chemistry*, 97, 10996-11000.
- Osthoff, H. D., Sommariva, R., Baynard, T., Pettersson, A., Williams, E. J., Lerner, B. M., Roberts, J. M., Stark, H., Goldan, P. D., Kuster, W. C., Bates, T. S., Coffman, D., Ravishankara, A. R., and Brown, S. S., 2006. Observation of daytime N_2O_5 in the marine boundary layer during new england air quality study - intercontinental transport and chemical transformation 2004, *Journal of Geophysical Research-Atmospheres*, 111.
- Platt, U., Perner, D., Winer, A. M., Harris, G. W., and Pitts, J. N., 1980. Detection of NO_3 in the polluted troposphere by differential optical-absorption, *Geophysical Research Letters*, 7, 89-92.
- Schulz, K. J., and Simpson, W. R., 1998. Frequency-matched cavity ring-down spectroscopy, *Chemical Physics Letters*, 297, 523-529.
- Simpson, W. R., 2003. Continuous wave cavity ring-down spectroscopy applied to in situ detection of dinitrogen pentoxide (N_2O_5), *Review of Scientific Instruments*, 74, 3442-3452.

Stutz, J., Alicke, B., Ackermann, R., Geyer, A., White, A., and Williams, E., 2004. Vertical profiles of NO_3 , N_2O_5 , O_3 , and NO_x in the nocturnal boundary layer: 1. Observations during the Texas air quality study 2000, *Journal of Geophysical Research-Atmospheres*, 109, D16398.

Vollenweider, P., Woodcock, H., Kelty, M. J., and Hofer, R. M., 2003. Reduction of stem growth and site dependency of leaf injury in Massachusetts black cherries exhibiting ozone symptoms, *Environmental Pollution*, 126, 458-458.

Walker, H. A., 2001. Understanding and managing the risks to health and environment from global atmospheric change: A synthesis, *Human and Ecological Risk Assessment*, 7, 1195.

Wayne, R. P., Barnes, I., Biggs, P., Burrows, J. P., Canosamas, C. E., Hjorth, J., Lebras, G., Moortgat, G. K., Perner, D., Poulet, G., Restelli, G., and Sidebottom, H., 1991. The nitrate radical - physics, chemistry, and the atmosphere, *Atmospheric Environment Part a-General Topics*, 25, 1-203.

Wood, E. C., Wooldridge, P. J., Freese, J. H., Albrecht, T., and Cohen, R. C., 2003. Prototype for in situ detection of atmospheric NO_3 and N_2O_5 via laser-induced fluorescence, *Environmental Science & Technology*, 37, 5732-5738.

Wood, E. C., Bertram, T. H., Wooldridge, P. J., and Cohen, R. C., 2005. Measurements of N_2O_5 , NO_2 , and O_3 east of the San Francisco bay, *Atmospheric Chemistry and Physics*, 5, 483-491.

Chapter 2:

The configuration and operation of the NO_3 - N_2O_5 field instrument

2.1 Introduction

Off-axis cavity ring-down spectroscopy, oa-CRDS, is a highly sensitive technique that we apply here for measuring atmospheric mixing ratios of NO_3 and N_2O_5 . Appendix A contains a previously published manuscript in which we describe the oa-CRDS technique and its application to measuring NO_3 and N_2O_5 (Ayers, et al., 2005). In oa-CRDS, a variant of traditional CRDS, an off-axis alignment is employed to couple laser light into an optical cavity constructed of two highly reflective mirrors. The off-axis configuration simplifies the operation of the instrument by reducing the spatial and spectral optical alignment required with traditional CRDS (see Fig 2.1 for examples of both alignment configurations). Furthermore, the off-axis alignment makes oa-CRDS significantly less sensitive to mechanical vibration and temperature-induced optical drift. Through its simplicity of operation and tolerance of a wide range of ambient conditions, oa-CRDS has proven to be a robust field technique for measuring NO_3 and N_2O_5 . In this chapter, we describe the configuration of an oa-CRDS-based field instrument and its application to measuring NO_3 and N_2O_5 . Furthermore, we describe the operational procedures, data reduction, and data correction that allows for quantification of ambient NO_3 and N_2O_5 mixing ratios. Chapter 3 of this thesis describes the successful intercomparison of our instrument with another instrument designed for measuring NO_3 and N_2O_5 .

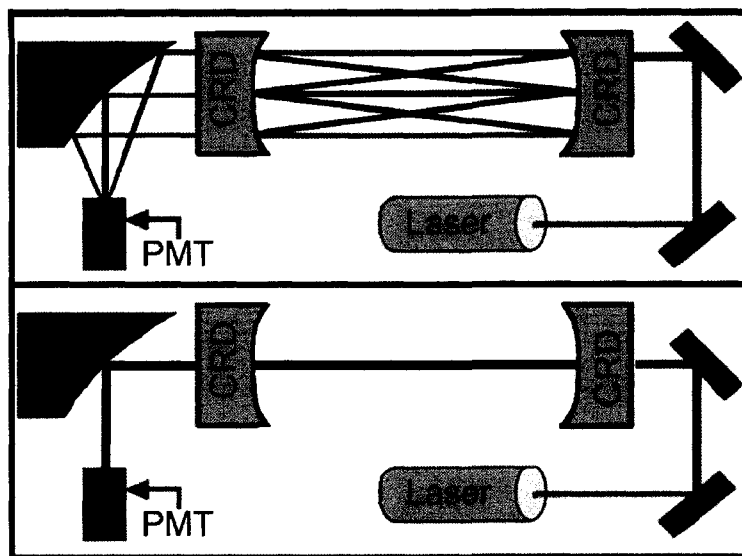


Fig. 2.1 Examples of cavity ring-down spectroscopy. Top panel: schematic representation of off-axis cavity ring-down spectroscopy. Laser light is shown entering the optical cavity, constructed of 2 highly reflective cavity ring-down mirrors (CRD), through an off-axis alignment. Each time the light beam hits the curved, reflective surface of a CRD mirror, a small fraction of light leaks from the cavity (typically $<0.00005\%$). The cavity output light from one mirror is focused onto a photomultiplier tube (PMT) by a 90° off-axis parabolic mirror. For comparison, the bottom panel shows a schematic representation of cavity ring-down spectroscopy employing an on-axis optical alignment. To maintain the traditional on-axis alignment, considerable effort is required to isolate the optical components from mechanical vibration and thermal fluctuations.

2.2 The $\text{NO}_3\text{-N}_2\text{O}_5$ Field instrument

2.2.1 Measuring NO_3 and N_2O_5 with oa-CRDS

In all forms of CRDS, including oa-CRDS, light of a certain wavelength is injected into an optical cavity constructed of two highly reflective mirrors. Typical mirror reflectivity, R , is greater than 99.99%. After sufficient light intensity is built up between the mirrors, the light source is turned off and the exponential decay rate of light trapped in the cavity is measured. The circulating intensity of light within the cavity can be described by:

$$I(t) = I_0 e^{(-t/\tau)}. \quad \text{eqn. 2.1}$$

Here, I_0 is the initial intensity in the cavity, $I(t)$ is the intensity at time t , and τ is the ring-down time of the cavity. The ring-down time is the result of two primary optical loss processes: (a) imperfect mirror reflection, and (b) scattering and absorption by gases and particles within the cavity. When the cavity is void of any absorbing or scattering chemical species, the ring down time (τ_b ; b for baseline) is determined by mirror reflectivity, R , and the length of the cavity, L :

$$\tau_b = \frac{L}{c(1-R)}. \quad \text{eqn. 2.2}$$

The presence of an absorbing or scattering species will result in increased optical loss. The greater the optical loss, the faster the ring-down that occurs. The ring-down time (τ_m ; m for measure) in the presence of an absorbing species is described by

$$\tau_m = \frac{L}{c[(1-R) - \alpha L_a]}. \quad \text{eqn. 2.3}$$

Here, c is the speed of light, α is the absorption coefficient, and L_a is the portion of the cavity filled with the absorbing chemical species. The measurement of the ring-down time in the presence (τ_m) and absence (τ_b) gives an absolute measurement of the molecular density (molecules cm^{-3}) of the absorbing species, $[A]_{\text{detected}}$.

$$[A]_{\text{detected}} = \frac{1}{c\sigma} \frac{L}{L_a} \left(\frac{1}{\tau_m} - \frac{1}{\tau_b} \right) \quad \text{eqn. 2.4}$$

Here, σ is the absorption cross section and L/L_a is the ratio of the cavity length (L) to the length of the cavity which is filled by the absorber (L_a).

In our oa-CRDS application, we measure the direct absorption of NO_3 around 662 nm. N_2O_5 is not optically active at 662 nm, but when heated above 70°C , N_2O_5 is rapidly dissociated to $\text{NO}_3 + \text{NO}_2$ with an efficiency near 100% (Simpson, 2003; Brown et al., 2003). By operating the instrument in the heated configuration described below, we are able to measure the ambient sum of $\text{NO}_3 + \text{N}_2\text{O}_5$ as NO_3 . Alternatively, the sampling cell can be operated at ambient temperature allowing for NO_3 -only measurements. We refer to the heated configuration as the “sum channel” indicating that the sum of $\text{NO}_3 + \text{N}_2\text{O}_5$ is being measured and the ambient-temperature configuration as the “ NO_3 channel” indicating that only NO_3 is being measured. By simultaneously operating a sum channel and an NO_3 channel, N_2O_5 -only measurements can be derived by taking the difference between the two channels. Because ambient N_2O_5 levels are typically a few orders of magnitude higher than NO_3 levels, this difference is not subject to large measurement noise.

2.2.2 NO_3 absorption cross sections

The NO_3 absorption cross section (σ) used in our application is taken from Yokelson et al. (1994) and has a 298 K peak cross section equal to 2.23×10^{-17} $\text{cm}^2/\text{molecule}$. Due to the dependence of the NO_3 absorption cross sections on temperature and wavelength, the cross sections used must be adjusted for the operating temperature of each channel and for the spectral range of the diode laser light source. First, the cross section is corrected for the spectral range of the laser output. The laser’s output is wavelength calibrated in reference to known wavelengths of neon lines emitted from a low-pressure lamp. The laser’s wavelength distribution is measured by an Ocean

Optics spectrometer (USB2000). Next, the weighted average of the cross section is calculated over the range of the laser spectrum. In order to capture the inherent fluctuations of the diode laser output, this procedure is repeated multiple times throughout a measurement campaign and the adjusted cross sections are used in conjunction with eqn 2.4 to determine NO₃ and N₂O₅ molecular densities. In the sum channel, the wavelength-averaged 298K cross section is typically around 1.94x10⁻¹⁷ cm² molecule⁻¹; while the NO₃ channel's 298 K cross section is near 1.90x10⁻¹⁷ cm²/molecule.

Second, the NO₃ absorption cross section is adjusted for its temperature dependence using the formula described by Yokelson et al. (1994):

$$\sigma(T) = \sigma(298K) \frac{\left(1 - \exp\left(\frac{-1096.4K}{T}\right) - 2 \exp\left(\frac{-529.5K}{T}\right)\right)}{\left(1 - \exp\left(\frac{-1096.4K}{298K}\right) - 2 \exp\left(\frac{-529.5K}{298K}\right)\right)}. \quad \text{eqn. 2.5}$$

Here, $\sigma(T)$ is the absorption cross section at the operating temperature (T) of the measurement cell and $\sigma(298K)$ is the absorption cross section at 298 K (Yokelson et al., 1994). The final, temperature-adjusted cross section for the sum channel is typically around 1.52x10⁻¹⁷ cm² molecule⁻¹, while the NO₃ channel's temperature corrected cross section is around 1.91x10⁻¹⁷ cm² molecule⁻¹.

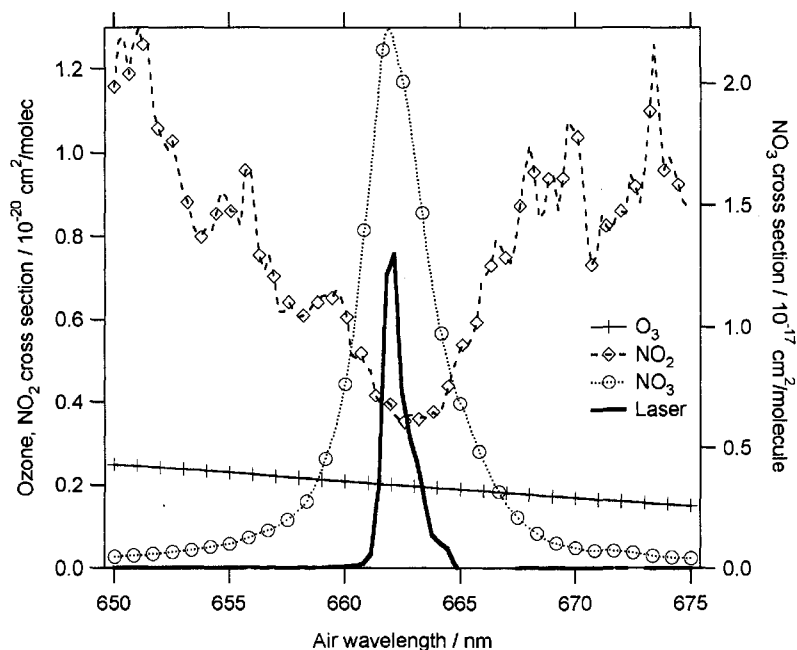


Fig. 2.2 Example NO_3 absorption cross section. Similar data is used for temperature and laser wavelength cross section corrections described in the text. The NO_3 absorption cross section is represented by the dashed trace with open circles (right axis). Using the laser spectrum (solid black trace), the weighted average of the NO_3 absorption cross section is calculated over the bandwidth of the laser. The resultant weighted average is used for σ in equation 2.4. Also included in the figure are the absorption cross sections for O_3 and NO_2 . Note that the NO_3 absorption cross section is approximately 4 orders of magnitude stronger than those of O_3 and NO_2 within the spectral range of the diode laser.

2.2.3 Field instrument configuration

The field instrument is housed in a lightweight, portable, weatherproof case (Pelican 1700) containing all of the optical and electronic components required for operation (fig. 2.3). The 662 nm light from a continuous-wave diode laser (Power Technology, IQ1A-series) is directed into an optical cavity consisting of two highly reflective cavity ring-down mirrors (CRD mirrors in fig. 2.3; $R > 0.99995$ at 662 nm, Los Gatos Research). The optical cavity is 68.5 cm long as measured from reflective surface to reflective surface of the 2 CRD mirrors. The output wavelength of the diode laser is

tunable over an approximate range of 5 nm by adjusting the operating temperature with a small trim pot external to the laser module.

One of the two turning mirrors directing the laser light into the cavity is mounted on a translation stage, which is used in achieving the off-axis optical alignment. The optics mount is maintained at 32°C by a resistive heater and temperature controller (TC in fig. 2.3). This thermal stabilization assists in minimizing temperature induced optical drift and prevents condensation from accumulating on the optical components. The diode laser is powered by an Acopian power supply (LPS in fig. 2.3), and the diode module is housed within the temperature controlled optical mount. The diode module is mounted in this way to aid in stabilizing the operating temperature of the laser, which prevents inadvertent temperature tuning of the output wavelength. To prevent the accumulation of debris on the reflective surfaces of the CRD mirrors, they are continuously purged by a small diaphragm pump (PP in fig. 2.3) at 0.2 liters per minute with filtered ambient air.

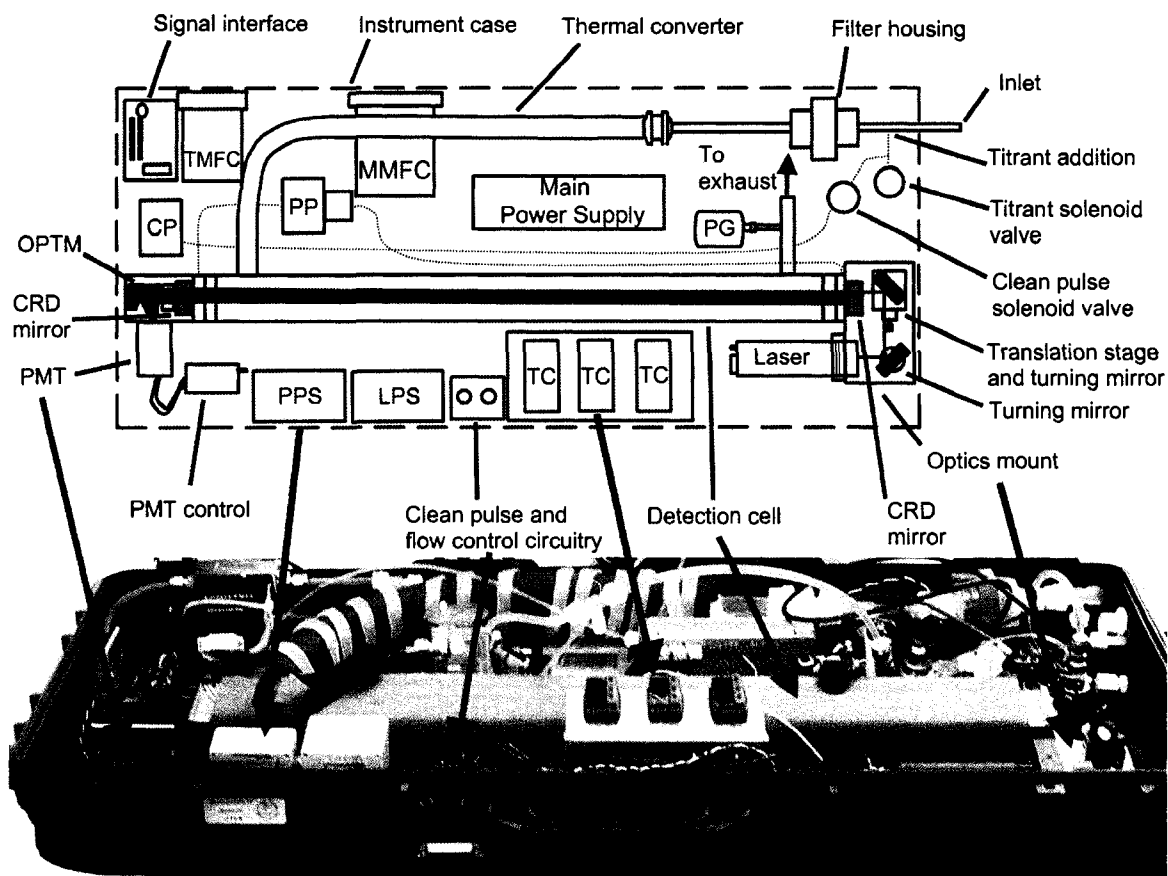


Fig. 2.3 The $\text{NO}_3\text{-N}_2\text{O}_5$ filed instrument. The schematic layout (top) is referenced to an instrument photograph (bottom). See text for detailed description.

The light output at one end of the cavity is collected by a 90° off-axis parabolic turning mirror (OPTM in fig. 2.3; $f = 25.4$ mm, Edmund Optics) and directed into a photomultiplier tube (PMT in fig. 2.3; Hamamatsu H6780-20) which is powered by an Acopian power supply (PPS in fig. 2.3). The output current of the photomultiplier tube is converted to a voltage by a $10\text{ k}\Omega$ terminating resistor and digitized (at a $5\text{ megasample s}^{-1}$ rate) using a 12-bit Gage 1250 Compuscope card mounted in a personal computer. The computer is connected to a signal interface (fig. 2.3) by a selectable length umbilical which allows the instrument to be placed outdoors while the computer is housed in a

temperature-controlled environment. The computer also controls the diode laser operation through a data acquisition and control card (NI PCI-6023E) that modulates the laser output intensity on-off repetitively at a user selected rate, typically ≥ 500 -Hz. Under typical operating conditions, baseline ring-down times are on the order of 160 μ s, resulting in an effective optical pathlength of about 50 km.

Ambient air is continuously pulled through a sampling cell, constructed entirely of PFA Teflon tubing (3/4" outer diameter, 5/8" inner diameter), at 8 standard liters per minute (slpm). The sample flow is controlled by a mass flow controller (MMFC in fig. 2.3), and the sample cell pressure is measured by a pressure transducer (PM in fig. 2.3). First, the ambient air sample passes through a 16.5 cm long inlet with a 47 mm Teflon filter (Pall Teflo membrane, 2.0 μ m pore size) housed at the mouth to minimize particulate flow into the cavity. The filter is changed every 3 to 4 hours to prevent sample loss due to soiled filters. Second, the sampled air enters a 52 cm long thermal converter which is temperature controlled (TC in fig. 2.3) at 100 °C. Heating of the sample allows for the detection of the sum of $\text{N}_2\text{O}_5 + \text{NO}_3$, as described above. Third, the heated air is flowed through the 68.5 cm long detection cell which is temperature controlled (TC in fig. 2.3) at 85 °C to prevent the re-partitioning of NO_3 back to N_2O_5 . It is in the detection cell where the sample is probed by measuring the direct absorption of NO_3 *via* oa-CRDS. The linear flow velocity of the sample through the sampling cell is approximately 66 cm/s, resulting in an instrument residence time of approximately 2 s. Raw ring-down times, instrument temperatures, flow rates, and sampling cell pressures are recorded at user selected intervals, typically on the order of every 2 s.

2.2.4 Chemical zeroing

Determination of the baseline ring-down time (τ_b), is achieved by periodically adding nitric oxide (NO) to the flowing sample at the inlet (titrant addition in fig. 2.3). The titrant flow rate is controlled by a mass flow controller (TMFC in fig 2.3) and directed into or away from the main flow *via* the titrant solenoid valve. NO reacts rapidly with NO₃ to produce 2 nitrogen dioxide molecules (NO₂), effectively removing all of the NO₃ from the sample. Because the absorption cross section of NO₂ is approximately 10⁻⁴ of that of NO₃ (fig. 2.2), the optical loss in the cavity is decreased by the addition of NO and results in a modulation of the NO₃ signal. Figure 2.4 shows NO₃ signal modulation by chemical zeroing with NO.

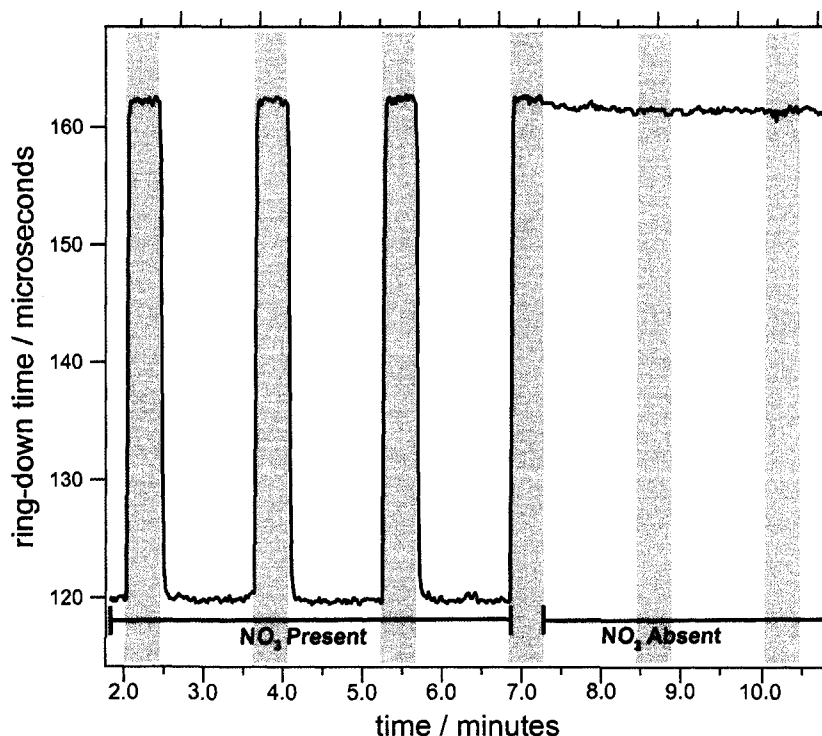


Fig. 2.4 Example of baseline determination by chemical zeroing with nitric oxide. The black trace is the ring-down time (τ) shown as a function of time. During the shaded periods, the baseline ring-down time (τ_b) is measured by adding NO to the inlet, destroying all NO_3 in the sample. During the periods with white backgrounds, ambient air ring-down times (τ_m) are being measured. When NO_3 is present, τ_m is decreased due to the strong optical absorbance of NO_3 (left-hand side of plot). When NO_3 is absent, there is no difference between τ_b and τ_m (right-hand side of plot).

Under typical operating conditions, NO is added to the sample flow for 30 seconds out of every 150 seconds so that the mixing ratio is approximately 50 parts per billion by volume (ppbv) in the measurement cell. The NO-titration cycle described here results in 120 seconds of measurement and 30 seconds of zeroing. Immediately following each NO titration, a 0.5 second “clean pulse” of NO-free air is generated by a small diaphragm pump (CP in fig 2.3) and added to the NO-delivery line to prevent residual NO from slowly leaking into the sample flow. A slow leak of NO would falsely

increase the measurement ring-down time (τ_m), subsequently resulting in an under-determination of the NO_3 concentration. The clean pulse solenoid valve (fig 2.3) stops the clean pulse flow at all times except during the clean pulse.

The first 5 seconds of every zeroing period and the first 10 seconds of every measurement period are discarded to allow titrant (NO) to fill or be removed from the cell, respectively. This procedure further ensures that transient titrant concentrations do not impact baseline or measurement ring-down time determination. The zeroing efficiency of titration with NO is discussed in detail in several locations, and has been determined to be essentially 100% under conditions similar to our operating protocol (Dick, 2002; Brown et al., 2002; Simpson, 2003; Brown et al., 2003; Dube, 2006).

Particulate aerosol, water vapor, ozone (O_3), and NO_2 may either scatter or absorb light near 662 nm, and, therefore, they act as potential interferences with the determination of the instrument zero. As described by Simpson (2003), the only interference of consequence is from the formation of NO_2 by the reaction of NO added for titration with ambient O_3 within the sampled air. Under typical operating conditions, this reaction generates a small negative offset (from -0.06 to -0.05 pptv NO_3 /ppbv O_3) in the baseline. This offset is easily quantified and subtracted from the data based on ambient measurements of O_3 , known abundance of NO added, and the operating temperature and residence time of the sampling cell. At 40 ppbv O_3 (typical ambient air values), the offset is about -2 pptv NO_3 .

2.3 NO₃ and N₂O₅ sampling losses

Losses of NO₃ and N₂O₅ can be induced as the sample contacts various surfaces while being transported through the instrument. NO₃ may be removed by reactions with the inlet filter, aerosol particles trapped on the inlet filter, or with the walls of the sampling cell. Similarly, N₂O₅ may be removed by reacting with water adsorbed to the surfaces of the instrument or on aerosol particles trapped on the filter. Regardless of the cause, the end result of unaccounted for sample loss is the inaccurate quantification of ambient NO₃ and N₂O₅.

The equilibrium between NO₃ and N₂O₅, achieved in the nighttime atmosphere, can be described by:



The equilibrium reaction R2.1 is highly dependent on temperature and NO₂ abundance. Under typical field deployment conditions at high latitudes, ambient temperature and NO₂ levels shift the NO₂/NO₃/N₂O₅ equilibrium strongly in favor of N₂O₅ (see full discussion in chapter 4, section 6). Therefore, while in use during high latitude field campaigns, the sampling cell is heated to detect N₂O₅, and, for this reason, we use N₂O₅ in the following example describing our procedure for quantifying sample loss.

However, the procedure described below is also fully applicable to NO₃ measurements.

The ambient N₂O₅ concentration, denoted as [N₂O₅]_{ambient}, will experience reactive losses of N₂O₅ due to sampling. Losses after sampling will cause a lower concentration of N₂O₅ to be detected, which we call [N₂O₅]_{detected}. Equation 2.4 describes the measurement of ambient N₂O₅ less the sampling losses. In determining the

cell transmission efficiency (E_{cell}) for N_2O_5 , we can quantify the ambient mixing ratio prior to losses as:

$$[N_2O_5]_{ambient} = \frac{[N_2O_5]_{detected}}{E_{cell}}. \quad \text{eqn. 2.6}$$

In the absence of sample loss, $E_{cell} = 1$ and $[N_2O_5]_{ambient} = [N_2O_5]_{detected}$. Conversely, when sample loss is present, $E_{cell} < 1$ and $[N_2O_5]_{detected}$ does not accurately represent the ambient concentration. However, if E_{cell} is quantified, equation 2.6 can then be used to correct data to take into account this effect.

We quantify E_{cell} during field campaigns by conducting frequent experiments where the N_2O_5 concentration is recorded for a series of inlet flow rates. We refer to these tests as flow experiments. These flow experiments must be conducted under the conditions that N_2O_5 is present in ambient air at relatively stable levels. The transmission efficiency of the cell as a function of residence time, $E(t)$, is defined as:

$$E(t) = \frac{[N_2O_5]_t}{[N_2O_5]_0}. \quad \text{eqn. 2.7}$$

Here, $[N_2O_5]_0$ is the N_2O_5 concentration at zero residence time in the cell and $[N_2O_5]_t$ is the concentration measured in the cell at some residence time, t . At the standard residence time (ts) the transmission efficiency of the cell, $E(ts)$, is defined as:

$$E(ts) = \frac{[N_2O_5]_{ts}}{[N_2O_5]_0}. \quad \text{eqn. 2.8}$$

Here, $[N_2O_5]_{ts}$ is the N_2O_5 concentration measured in the cell at the standard residence time.

Clearly, a measurement of N_2O_5 at zero residence time is not attainable, but by referencing cell transmissions (at various residence times) to the measurement of $[\text{N}_2\text{O}_5]_{st}$ a relative cell transmission, $E_{rel}(t)$, can be determined:

$$E_{rel}(t) = \frac{E(t)}{E(ts)} = \frac{[\text{N}_2\text{O}_5]_t}{[\text{N}_2\text{O}_5]_{ts}} \quad \text{eqn. 2.9}$$

In our case, $[\text{N}_2\text{O}_5]_{ts}$ is measured at 8 slpm flow, while $[\text{N}_2\text{O}_5]_t$ is measured at both 2 and 4 slpm (left panel fig. 2.5). Assuming first order losses, a plot of $\text{Ln} \frac{[\text{N}_2\text{O}_5]_t}{[\text{N}_2\text{O}_5]_{ts}}$ against residence time provides a means for determining E_{ts} . Here, a linear fit to the data gives a y-intercept that is equal to $\text{Ln}(1/E(ts))$; see fig. 2.5.

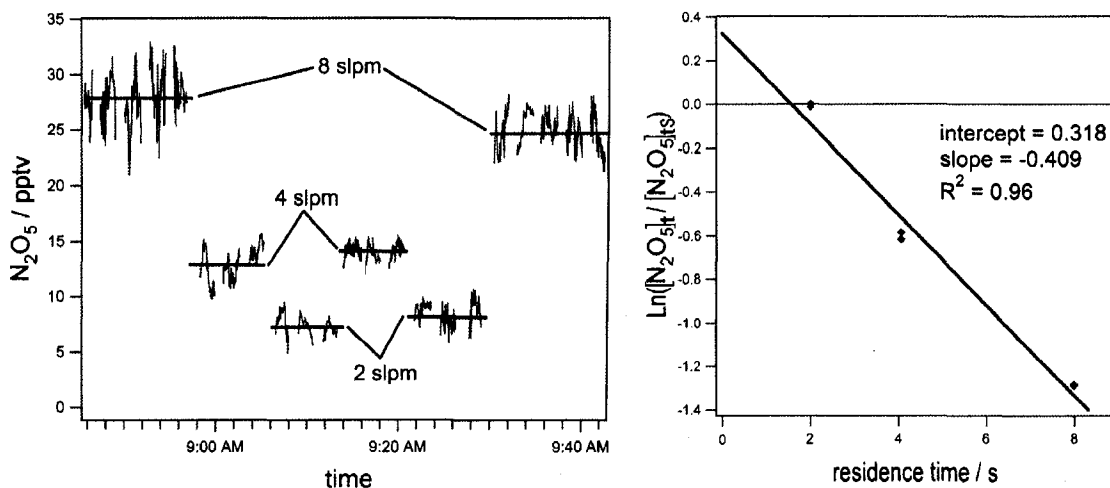


Fig. 2.5 Example of a flow experiment that was conducted during the Fall 2007 field campaign and used for determining $E(ts)$. The left panel shows duplicate measurements of N_2O_5 levels measured at 8 slpm, 4 slpm, and 2 slpm. The measured N_2O_5 levels were averaged over each period indicated by the black horizontal bars and then used to construct the $\text{Ln}([\text{N}_2\text{O}_5]_t / [\text{N}_2\text{O}_5]_{ts})$ plot in the right panel. Here, the red diamonds are the data points, and the blue trace is the linear fit to the data extrapolated to zero residence time. The zero line is shown in black for reference.

The right panel of fig. 2.5 shows an example of the determination of $\text{Ln}(1/E(ts))$ from a flow experiment conducted during a field campaign in the Fall of 2007 (described in chapter 4). It should be noted that at our standard sampling flow rate of 8 slpm, $E(ts) = E_{cell}$. The red diamonds are the actual data, and the blue trace is the linear fit to the data. From the y-intercept of the linear fit, E_{cell} on this particular experimental day was taken as equal to 0.73 ± 0.02 . An averaged $E_{cell} = 0.75 \pm 0.04$ (1- σ error) was obtained from 6 valid flow experiments that were conducted during the Fall 2007 field campaign. The application of this averaged E_{cell} to the field data is described below.

2.4 Final field data reduction

Combining the notation of eqns. 2.4 and 2.6, we can now express the ambient measurement of N_2O_5 as:

$$[\text{N}_2\text{O}_5]_{\text{ambient}} = \frac{1}{c \sigma} \frac{L}{L_a} \frac{1}{E_{cell}} \left(\frac{1}{\tau_m} - \frac{1}{\tau_b} \right). \quad \text{eqn. 2.10}$$

Equation 2.10 provides a means for quantifying ambient concentrations of N_2O_5 and was generally used in processing the data collected during the campaigns described in this thesis. However, we did not conduct flow tests to examine N_2O_5 losses during the Spring 2007 campaign presented in chapter 5, and, as a result, experimentally-determined cell transmissions were not available for the Spring 2007 campaign. Therefore, we applied the $E_{cell} = 0.75$ (described above) to the Spring 2007 data set in order to correct all field data in a uniform manner.

2.4.1 Bypass manifold loss correction for Spring 2007 campaign

The experimental set up for the Spring 2007 campaign required the use of a 10 meter-long bypass manifold constructed of 1/2" O. D. (outer diameter), 3/8" I.D. (inner diameter) Teflon tubing. A full description of the manifold can be found in chapter 5. Briefly, during the Spring 2007 campaign, the N₂O₅ instrument was housed in a temperature controlled building. In order to obtain an ambient sample that was not perturbed by the building, a high volume pump was used to draw ambient air along the 10 m long manifold and into the building for sampling. The manifold flow was maintained at about 115 slpm, and the instrument sampled from the manifold using a 1/2" T –union made of Teflon at a rate of 8 slpm.

The additional 10 m of Teflon tubing used in the manifold presented a potential loss source that was not previously quantified. To assess sample losses induced by the manifold, we estimated the manifold transmission efficiency (E_{mani}) based on the cell transmission (E_{cell}) described in section 2.3. Assuming first order losses, we can re-write eqn. 2.7 as:

$$E_{cell} = \exp(-k_{cell} R_{cell}). \quad \text{eqn. 2.11}$$

Here, k_{cell} is the first order cell loss rate coefficient, and R_{cell} is the residence time of the sample in the cell. With E_{cell} equal to 0.75 and R_{cell} equal to 2 s, as described above, k_{cell} is calculated as 0.144 s^{-1} .

Similarly, the manifold transmission efficiency is defined as:

$$E_{mani} = \exp(-k_{mani} R_{mani}), \quad \text{eqn. 2.12}$$

where, the residence time of the manifold, R_{mani} , = 0.34 seconds. Because the manifold and the sampling cell are both constructed of Teflon tubing, we assume the losses are similar, and, subsequently, we assume $k_{mani} = k_{cell}$. Based on these assumptions, eqn. 2.12 gives $E_{mani} = 0.95$, which is applied as a correction factor in the same manner that T_{cell} is applied to the data.

2.4.2 Conversion of ambient measurements to mixing ratios

The corrected N_2O_5 number densities ($[N_2O_5]_{ambient}$), described above, are converted to mixing ratios ($X_{N_2O_5}$) using:

$$X_{N_2O_5} = \frac{[N_2O_5]_{ambient}}{[air]} \quad \text{eqn. 2.13}$$

Here, $[air]$ is the number density of air and is given by:

$$[air] = \frac{A_v P}{RT} \quad \text{eqn. 2.14}$$

In eqn. 2.13, $A_v = 6.022 \times 10^{23}$ molecules mol^{-1} is Avogadro's number, P is the sampling pressure, R is the universal gas constant, and T is the sampling cell temperature. The N_2O_5 mixing ratios are generated at instrument-native time intervals, typically around 2 seconds, and averaged to 60 seconds for subsequent analysis. Mixing ratios for the duration of both the Fall and Spring 2007 campaigns can be seen in chapters 4 and 5, respectively. Furthermore, NO_3 and N_2O_5 mixing ratios from an instrument intercomparison can be seen in chapter 3. The conversion of raw ring-down times to mixing ratios, including the application of all correction factors, has been automated through software developed in LabView by our research group.

2.4.3 Correction to the NO₃ data from the instrument intercomparison

The complete experimental set up for the instrument intercomparison campaign is described in chapter 3. During the campaign, NO₃ measurements were affected by small temperature differences between the SAPHIR chamber and the oa-CRDS measurement cell. The equilibrium between NO₂, NO₃, and N₂O₅ (reaction R2.1) is highly dependent on temperature and NO₂ abundance. Thus, the temperature differences resulted in a re-partitioning of the NO₂/NO₃/N₂O₅ equilibrium. The rate of re-partitioning was often fast enough to be significant during the residence time of the sample in the measurement cell; therefore, a correction was applied to the measured NO₃ levels. In this section, we describe our method for correcting the NO₃ measurement error.

When the NO₂/NO₃/N₂O₅ equilibrium (R2.1) within the SAPHIR chamber is in a fully relaxed state the equilibrium constant ($K_{\text{eq,SAPHIR}}$) is given by:

$$K_{\text{eq,SAPHIR}} = \frac{[\text{N}_2\text{O}_5]_{\text{SAPHIR}}}{[\text{NO}_3]_{\text{SAPHIR}} [\text{NO}_2]_{\text{SAPHIR}}} = A \exp\left[-\frac{B}{T_{\text{SAPHIR}}}\right]. \quad \text{eqn. 2.15}$$

Here, A and B are thermodynamic constants describing the equilibrium. The values, $A = 2.7 \times 10^{-27} \text{ cm}^3 \text{ molec}^{-1}$ and $B = 11000 \text{ K}$ were taken from the JPL data set (Sander et al., 2006). Similarly, the expression for the equilibrium constant for R2.1 in the measurement cell ($K_{\text{eq,cell}}$) is given by:

$$K_{\text{eq,cell}} = \frac{[\text{N}_2\text{O}_5]_{\text{cell}}}{[\text{NO}_3]_{\text{cell}} [\text{NO}_2]_{\text{cell}}} = A \exp\left[-\frac{B}{T_{\text{cell}}}\right]. \quad \text{eqn. 2.16}$$

Assuming $[\text{N}_2\text{O}_5]_{\text{cell}} = [\text{N}_2\text{O}_5]_{\text{SAPHIR}}$ (which is reasonable because $[\text{N}_2\text{O}_5] > [\text{NO}_3]$), $[\text{NO}_2]_{\text{cell}} = [\text{NO}_2]_{\text{SAPHIR}}$, and by dividing eqn. 2.16 by eqn. 2.15 we arrive at the temperature dependent correction factor:

$$\frac{[\text{NO}_3]_{\text{SAPHIR}}}{[\text{NO}_3]_{\text{cell}}} = \exp\left[-\frac{B}{T_{\text{cell}}} + \frac{B}{T_{\text{SAPHIR}}}\right]. \quad \text{eqn. 2.17}$$

Furthermore, assuming that NO_2 is in excess in R2.1, we can define the pseudo-first order rate coefficient (k_p) for the formation of N_2O_5 as:

$$k_p = k_f[\text{NO}_2], \quad \text{eqn. 2.18}$$

where, k_f is the forward rate coefficient for R2.1. Following a temperature-induced perturbation, the system relaxes at an exponential rate determined by:

$$k_{\text{total}} = k_p + k_d. \quad \text{eqn. 2.19}$$

Here, k_d is the rate coefficient for the dissociation of N_2O_5 (reverse of R2.1). Assuming that $k_d \ll k_p$, the total rate coefficient (k_{total}) is approximately equal to k_p .

As described by Engel and Reid (2006), the fraction of NO_3 that re-equilibrates (f_r) due to the temperature difference is given by:

$$f_r = 1 - \exp[-k_p R_{\text{cell}}], \quad \text{eqn. 2.20}$$

where R_{cell} is the residence time of the measurement cell. The fraction of NO_3 that does not re-equilibrate (f_u) is given by:

$$f_u = 1 - f_r = \exp[-k_p R_{\text{cell}}]. \quad \text{eqn. 2.21}$$

Finally, the total correction factor, determined as a weighted average of f_r and f_u , is given by:

$$\frac{[\text{NO}_3]_{\text{SAPHIR}}}{[\text{NO}_3]_{\text{cell}}} = \exp(-k_p R_{\text{cell}}) + (1 - \exp(-k_p R_{\text{cell}})) \left(\exp\left(\frac{B}{T_{\text{cell}}} - \frac{B}{T_{\text{SAPHIR}}}\right) \right). \quad \text{eqn. 2.22}$$

This re-equilibration model blends between no corrections for low NO_2 , where the re-equilibration is slower than the residence time, to complete re-equilibration at high NO_2 .

The typical correction is around 13% per Kelvin of temperature difference (ΔT , typically < 2 K) between the chamber and analysis cell.

2.5 Performance of the oa-CRDS field instrument

As described by Simpson (2003), the sensitivity of the $\text{NO}_3\text{-N}_2\text{O}_5$ instrument can be estimated from the variability of the ring-down time or by actual measurements when NO_3 and N_2O_5 are absent. We use the former method here to describe the noise-equivalent optical sensitivity and detection limit of the oa-CRDS field instrument. For a description of the field instrument's performance using the later method, we refer the reader to chapter 3 where a $2\text{-}\sigma$ detection limit was quantified using observed data for an instrument intercomparison.

As described in Appendix A, the noise-equivalent optical sensitivity of the field instrument can be estimated using:

$$\alpha_{min} = \frac{L}{cL_a} \frac{\Delta\tau_{min}}{\tau_b^2}, \quad \text{eqn. 2.23}$$

where α_{min} is the minimum detectable absorbance coefficient, c is the speed of light, $L/L_a \approx 1.2$ (defined above), and τ_b is the baseline ring-down time (taken as $160 \mu\text{s}$). We estimate $\Delta\tau_{min}$, defined as the smallest measurable difference between τ and τ_b , to be the 2σ uncertainty in the measure of τ_b times $2^{1/2}$. The resulting 2σ sensitivity of the $\text{NO}_3\text{-N}_2\text{O}_5$ field instrument is $1.6 \times 10^{-10} \text{ cm}^{-1} \text{ Hz}^{-1/2}$. For operation at 1 atm, 85°C and an estimated NO_3 absorption cross section of $1.5 \times 10^{-17} \text{ cm}^2/\text{molecule}$, the noise-equivalent 2σ detection limit is calculated as 0.5 pptv in 1 second. This detection limit is

approximately four times lower than the one described for the prototype instrument (see Appendix A) when both detection limits are averaged to 1 second.

2.6 Conclusions

We have described the configuration and operation of a new field instrument for measuring ambient NO_3 and N_2O_5 . Furthermore, we have described a means for quantifying the losses of NO_3 and N_2O_5 that result from the sample coming into contact with the surfaces of the sampling equipment. The field instrument uses an optical technique that we developed, called off-axis cavity ring-down spectroscopy, to measure NO_3 and N_2O_5 . Furthermore, the new instrument was constructed based on improvements made to a prototype instrument. These improvements have resulted in a field instrument with a very high sensitivity.

There are two changes in the construction of the instrument and one change in the operational procedure which are primarily responsible for the improved performance of the new system when compared to the prototype. The field instrument was designed so that all of the surfaces contacted by the sample are made of Teflon. NO_3 and N_2O_5 sampling cells constructed in this way have been tested extensively, showing Teflon to be the material of choice for minimizing sample loss (Dube, 2006). By utilizing an all-Teflon sampling cell, we have minimized our surface losses compared to the halocarbon-coated stainless steel cell used in the prototype instrument. Secondly, significant gains have been made in improving the sensitivity and detection limit of the new instrument compared to the prototype instrument. The gains were made after incorporating an off-axis 90° parabolic turning mirror in the new system. Both of these changes in

construction have resulted in significant improvement in the performance of the system, but, perhaps, the most important improvement was the procedural change of monitoring the output wavelength of the laser. By monitoring the laser output with a portable spectrometer, we were able to capture inherent width and fluctuations in the bandwidth and peak wavelength of the light probing the sample. In doing so, we were able to make the appropriate adjustments in the wavelength-dependent absorption cross section for NO_3 and correspondingly improve our ability to quantify ambient NO_3 and N_2O_5 .

The new field instrument described here has been successfully tested and deployed in multiple research campaigns (detailed in the following chapters) and has proven to be highly effective in measuring ambient NO_3 and N_2O_5 . In addition to the effectiveness of oa-CRDS in measuring NO_3 and N_2O_5 , our field instrument is highly portable in that it is small, light weight (25 kg compared to the approximate 135 kg of instruments with similar capabilities), and weather resistant. Furthermore, the simplicity of operation and high tolerance of fluctuations in a variety of ambient conditions has made oa-CRDS a powerful tool for atmospheric field studies.

2.7 References

- Ayers, J. D.; Apodaca, R. L.; Simpson, W. R.; Baer, D. S., 2005. Off-axis cavity ringdown spectroscopy: application to atmospheric nitrate radical detection. *Applied Optics*, 44, (33), 7239-7242.
- Brown, S. S.; Stark, H.; Ryerson, T. B.; Williams, E. J.; Nicks, D. K.; Trainer, M.; Fehsenfeld, F. C.; Ravishankara, A. R., 2003. Nitrogen oxides in the nocturnal boundary layer: Simultaneous in situ measurements of NO_3 , N_2O_5 , NO_2 , NO , and O_3 . *Journal of Geophysical Research-Atmospheres*, 108, (D9).
- Brown S.S., Stark H., Ciciora S.J., McLaughlin R.J., and Ravishankara A.R., 2002. Simultaneous in situ detection of atmospheric NO_3 and N_2O_5 via cavity ring-down spectroscopy. *Rev Sci Instr.* 73 (9): 3291-3301.
- Dick, E.M., 2002. The application of cavity ring-down spectroscopy to determine nitrate radical concentrations in the atmosphere [Master's Thesis], University of Alaska Fairbanks, 109 Pp.
- Dube, W. P.; Brown, S. S.; Osthoff, H. D.; Nunley, M. R.; Ciciora, S. J.; Paris, M. W.; McLaughlin, R. J.; Ravishankara, A. R., 2006. Aircraft instrument for simultaneous, in situ measurement of NO_3 and N_2O_5 via pulsed cavity ring-down spectroscopy. *Rev Sci Inst*, 77, (3).
- Engel, T. and Reid, P., 2006. *Physical chemistry*. Pearson Benjamin Cummings; San Francisco. 1060 pp.
- Sander, S. P., Friedl, R. R., Golden, D. M., Kurylo, M. J., Moortgat, G. K., Keller-Rudek, H., Wine, P. H., Ravishankara, A. R., Kolb, C. E., Molina, M. J., Finlayson-Pitts, B. J., Huie, R. E., and Orkin, V. L., 2006. Chemical kinetics and photochemical data for use in atmospheric studies, Tech. rep., JPL Publication 06-2.
- Simpson W.R., 2003. Continuous wave cavity ring-down spectroscopy applied to in situ detection of dinitrogen pentoxide (N_2O_5). *Rev Sci Instr.* 74 (7): 3442-3452.
- Yokelson, R. J.; Burkholder, J. B.; Fox, R. W.; Talukdar, R. K.; Ravishankara, A. R., 1994. Temperature-dependence of the NO_3 absorption-spectrum. *Journal of Physical Chemistry*, 98, (50), 13144-13150.

Chapter 3:

Intercomparison of two N₂O₅ field instruments

3.1 Introduction

Reactions of dinitrogen pentoxide (N₂O₅) and nitrate radical (NO₃) play important roles in the nocturnal processing of nitrogen oxides (NO_x = NO + NO₂). Nitrogen oxide chemistry can impact the tropospheric ozone budget, control the concentration of volatile organic compounds (VOCs), and can result in the formation of nitric acid (HNO₃) which then may deposit (Finlayson-Pitts and Pitts, 2000). Furthermore, atmospheric reactions of NO_x have broad impacts on environmental pollution and human health, keeping tropospheric NO_x chemistry at the center of atmospheric research.

The primary removal mechanism for NO_x is the formation and subsequent deposition of HNO₃. During the day, HNO₃ formation is accomplished *via* reaction of NO₂ with hydroxyl radical (OH). At night, the oxidation process consists of several steps and begins with NO₂ reacting with ozone to form NO₃ (Finlayson-Pitts and Pitts, 2000). NO₃ is highly reactive and can act as the primary oxidant for numerous trace gases in the atmosphere, or it can react with NO₂ to form N₂O₅:



where, M can be any molecule and is typically N₂, O₂, or H₂O. The equilibrium reaction described in reaction R3.1 is highly dependent on temperature and NO₂ abundance in such a way that colder temperatures and moderate pollution (i.e. elevated NO₂) favor the formation of N₂O₅. Heterogeneous hydrolysis of N₂O₅ is the final steps in this nocturnal NO_x removal pathway:



Our understanding of nocturnal nitrogen oxide chemistry relies upon accurate and reliable observation of N_2O_5 and NO_3 .

Measurement of N_2O_5 dates back over twenty years, when long-path infrared (IR) absorption spectroscopy employing limb viewing geometries was used to observe stratospheric N_2O_5 levels (Kunde et al., 1988; Rinsland et al., 1989). Similarly, measurement of atmospheric NO_3 dates back nearly three decades to when differential optical absorption spectroscopy (DOAS) was first employed (Platt et al., 1980; Noxon et al., 1980a; 1980b). Because of the high sensitivity of DOAS NO_3 spectroscopy and only moderate pathlengths (~ 10 km), NO_3 can be detected in the troposphere. The longer paths needed for N_2O_5 IR spectroscopy are not achievable in the troposphere due to light scattering at atmospheric pressure and relatively high aerosol loads. The difficulty with these long-path techniques is that they cannot capture the highly variable spatial and temporal distributions of N_2O_5 and NO_3 . Only recently have techniques been developed for *in situ* tropospheric observations that are sensitive and fast enough to be useful in characterizing the dynamic reactions of nocturnal nitrogen oxides (King et al., 1999; Ball et al., 2001; Brown et al., 2002; Simpson, 2003; Wood et al., 2003; Ball et al., 2004; Ayers et al., 2005; Matsumoto et al., 2005; Wood et al., 2005; Dube' et al., 2006; Nakayama et al., 2008).

The most common methods used for *in situ* measurement of N_2O_5 employ some variant of cavity ring-down spectroscopy (CRDS), a highly sensitive direct absorption technique (King et al., 1999; Ball et al., 2001; Brown et al., 2002; Simpson, 2003; Ball et

al., 2004; Ayers et al., 2005; Dube' et al., 2006; Nakayama et al., 2008). Field instruments employing CRDS were first developed to measure NO_3 , as it possesses a very strong absorption band centered at 662 nm. When heated, N_2O_5 decomposes to NO_3 + NO_2 (see reaction R3.1), and can therefore be measured as NO_3 . CRDS techniques report sensitivities ranging from about 0.1 to 3 pptv for N_2O_5 and NO_3 , and can typically operate with time resolutions ranging from a couple of seconds to sub-second (Brown et al., 2002; Simpson, 2003; Ball et al., 2004; Ayers et al., 2005; Dube' et al., 2006; Nakayama et al., 2008). Another technique used for measuring N_2O_5 is laser-induced fluorescence (LIF), which has been applied with varying degrees of success. Reported sensitivities for LIF instruments are in the range of 50 to 100 pptv in 3 to 5 minutes (Wood et al., 2003; 2005; Matsumoto et al., 2005). Lastly, chemical ionization mass spectrometry has been applied to measuring the sum of NO_3 + N_2O_5 , with a sensitivity of about 12 pptv in 1s (Slusher et al. 2004). To the best of our knowledge, no intercomparison of N_2O_5 and NO_3 measurement techniques has reported in current literature.

In June 2007, research groups from Germany, Ireland, Japan, the United Kingdom, and the United States participated in a large-scale intercomparison of field instruments designed for measuring N_2O_5 , NO_3 , and NO_2 . The instrument intercomparison exercise was conducted in Jülich, Germany from 9 June 2007 through 21 June 2007 at the SAPHIR atmospheric simulation chamber on the campus of Forschungszentrum Jülich. The full results of the N_2O_5 , NO_3 and NO_2 portions of the intercomparison will be presented in companion papers that are in preparation and are

planned for submission to the journal *Atmospheric Chemistry and Physics* (Apodaca et al., 2008; Dorn et al., 2008; Fuchs et al., 2008).

In this work, we compare the performance of two of the six instruments that participated in the first N_2O_5 instrument intercomparison. The N_2O_5 instruments from the University of Alaska Fairbanks (UAF) and from the National Oceanic and Atmospheric Administration (NOAA) were selected for comparison in this manuscript for multiple reasons. First, both instruments employ variants of CRDS, but with differing and independent calibration procedures. Second, the UAF and NOAA instruments have similar sensitivities and time resolutions, while the other instruments that participated in the intercomparison are less sensitive and have slower time resolutions. Lastly, of all of the participants in the intercomparison, only the UAF and NOAA instruments were capable of independently producing N_2O_5 -only measurements. The other participants either reported sum-measurements of $\text{NO}_3 + \text{N}_2\text{O}_5$ or $\text{HNO}_3 + 2\text{N}_2\text{O}_5$. Comparing the N_2O_5 -only measurements produced by UAF and NOAA will give the clearest picture of our ability to understand the role that N_2O_5 plays in nocturnal nitrogen oxide chemistry.

3.2 Experiment

3.2.1 Instrument descriptions

As stated above, the two instruments described in this intercomparison are both based on the direct absorption technique called cavity ring-down spectroscopy. Cavity ring-down spectroscopy has been described in detail in many places (O’Keefe and Deacon, 1988; Ball et al., 2001; Brown et al., 2002; Atkinson, 2003; Ayers et al., 2005) as well as in chapter 2 of this thesis. Furthermore, the UAF instrument was fully

characterized in chapter 2, while a complete description of the NOAA instrument can be found in Dube et al. (2006). A brief summary description is given here, highlighting the fundamental similarities and key differences between the two instruments.

3.2.1.1 The UAF oa-CRDS field instrument

The UAF instrument employs off-axis cavity ring-down spectroscopy, oa-CRDS, as the optical technique for measuring N_2O_5 . Appendix A contains a previously published manuscript in which we first describe the oa-CRDS technique as applied to measuring NO_3 and N_2O_5 (Ayers, et al., 2005). In oa-CRDS, an off-axis alignment is employed to couple light near 662 nm into an optical cavity constructed of two highly reflective mirrors. The light source is a light-weight, high-intensity (~35 mW) diode laser. The off-axis alignment reduces the rigorous spatial and spectral optical alignment required with traditional CRDS. Furthermore, the off-axis alignment makes oa-CRDS less sensitive to mechanical vibration and temperature-induced optical drift.

The UAF instrument, housed in a weather proof case, pulls ambient air through a filtered (Pall Teflo membrane, 2.0 μm pore size) sampling cell constructed entirely of PFA Teflon at a rate of 8 standard liters per minute (slpm). During the intercomparison, a clean filter was placed in the instrument once daily, at the beginning of each experiment. After passing through the filter, the sample is flash heated to 100°C, and subsequently maintained at 85°C, to convert N_2O_5 to NO_3 for measurement in the optical cavity. As described in chapter 2, the UAF oa-CRDS field instrument has a calculated noise-equivalent detection limit of 0.5 pptv in 1 second. The UAF instrument is highly portable due to its small size and light-weight construction (25 kg).

3.2.1.2 The NOAA CaRDS field instrument

The NOAA instrument utilizes a traditional approach to cavity ring-down spectroscopy and was designed for deployment in the NOAA WP-3D Orion aircraft. The light source is a pulsed, Nd:YAG pumped dye laser. The beam from the dye laser, tuned near 662 nm, is coupled into an optical cavity using an on-axis alignment (Dube, 2006).

The NOAA instrument pulls ambient air through a filtered (Pall Teflo membrane, 2.0 μm pore size) fast-flow manifold at 40-50 slpm. From this manifold, air is sampled at 8 slpm and heated in various stages (at temperatures ranging from 120°C to 75°C) to thermally decompose N_2O_5 to NO_3 for measurement. Both the fast-flow manifold and the sampling cell are constructed of PFA Teflon.

The NOAA instrument is equipped with an automated filter changer, a feature that allowed the filters to be replaced on an hourly basis throughout the intercomparison exercise, without significant interruption in data acquisition. The NOAA instrument is reported to have a calculated sensitivity of 0.1 pptv in 1 s, and an actual sensitivity for N_2O_5 of approximately 1 pptv in 1 s (Dube, 2006). Because the NOAA instrument was designed for aircraft deployment, it is not housed in a weather proof case. Furthermore, because of the weight of the automated filter changer, pulsed Nd:YAG laser pumped dye laser, and the vibration isolation equipment required to maintain the on-axis alignment of the cavity, the NOAA instrument is only moderately portable at 125 kg (Dube, 2006).

3.2.2 The SAPHIR chamber

SAPHIR is a large volume (270 m^3) reaction chamber designed for the investigation of simulated tropospheric chemical systems under realistic conditions. The

chemical and aerosol composition, as well as the relative humidity within the chamber are readily controlled and monitored, making SAPHIR the ideal location for an instrument intercomparison. The chamber is constructed of double-walled fluorine-ethene-propene (FEP) Teflon foil (Dupont) that has a light transmission of 85% for visible, UV-A, and UV-B (Schlosser, et al., 2007). The space between the two foils is flushed continuously with high-purity N_2 and the inner chamber is operated with synthetic air (N_2 , O_2 , purity > 99.9999 %). A flow controller regulates the replenishment of chamber air lost due to extractive sampling and wall leakage and the chamber is kept at 40 to 60 Pa above ambient pressure in order to prevent contamination with outside air. The replenishment flow can be operated at rates up to $500 \text{ m}^3 \text{ h}^{-1}$ to purge trace gas levels in the chamber below detectable levels.

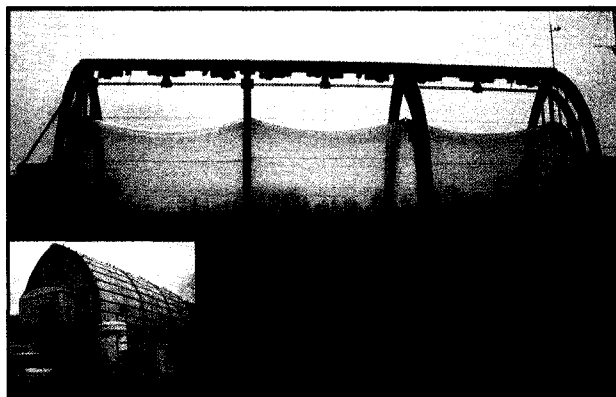


Fig. 3.1 Photograph of the SAPHIR atmospheric simulation chamber. The shutter system is open, exposing the FEP-walled cylindrical chamber to ambient sunlight levels. Below the chamber are the shipping containers that were used to house the instruments during the intercomparison. The inset shows SAPHIR with the shutter system closed.

The chamber is of cylindrical shape (fig. 3.1) with a 5 m diameter and an 18 m length. SAPHIR is equipped with a shutter system that keeps the chamber volume in darkness when required, but can also be opened to allow for daylight exposure and the

measurement of photolysis reactions. Trace gases (NO_x , O_3 , H_2O , CO , VOCs, etc.) can be added as desired to simulate a variety of conditions (urban, rural, marine, etc.) to investigate the chemistry of compounds of interest. An internal fan mixes the chamber air within 1 min or less and several instruments are installed allowing for the measurement of a large set of relatively stable trace gases (NO_x , O_3 , CO , VOCs). Ozone is measured by an instrument based on absolute UV absorption at 254 nm (Ansyco); NO and NO_2 are measured by a chemiluminescence detector; and hydrocarbons are detected by a gas chromatograph (Chrompack) which is described in detail by Wegener et al. (2007). Furthermore, the chamber set-up includes standard instruments for measuring temperature, pressure, humidity, and gas replenishment flow.

3.2.3 Chamber experiments

The instruments were located beneath the chamber and sampled the chamber air through individual ports in the wall, spaced approximately 10 m apart. Eleven chamber experiments were conducted where the instruments measured concurrently under well controlled chemical conditions designed to test the instrumental performance as a function of varying concentrations of N_2O_5 , NO_3 , O_3 , NO_2 , water vapor, reactive hydrocarbons, and inorganic and organic aerosols. Table 3.1 outlines the experimental conditions on each day of the intercomparison.

Table 3.1 Experimental conditions and chemical composition of the chamber volume during the intercomparison exercise. NO₂, O₃, VOC, and aerosol levels listed are the maximum values achieved during each experiment. SOA represents the presence of secondary organic aerosol particles.

June 2007	Experiment type	NO ₂ ppbv	O ₃ Ppbv	VOC/ Ppbv	Aerosol	RH
9	NO ₂ interference	5	100	-	-	<1%
10	Water/ozone interference	5	70	-	-	<1%
11	Ambient air	20	70	-	Ambient aerosol	60%
12 13	Clean air/photolysis	9	200	-	-	<1%
14	Butanal and secondary organic aerosol (SOA) interference	21	130	Butanal/10	SOA	<1%
15	Inorganic aerosol (NH ₄) ₂ SO ₄	9	180	-	(NH ₄) ₂ SO ₄	60%
16 17	Limonene and SOA interference	20	80	Limonene/20	SOA	<1%
18	Isoprene and SOA interference	38	70	Isoprene/10	SOA	57%
20	β-pinene and SOA interference/dry	80	100	B-pinene/15	SOA	<1%
21	β-pinene and SOA interference/humid	80	100	B-pinene/15	SOA	<50%

3.3 Results and discussion

3.3.1 UAF-NOAA Intercomparison

Simultaneous N₂O₅ measurements by the UAF and NOAA instruments are shown in fig. 3.2 for 3 selected days of the intercomparison. The upper row in fig. 3.2 consists of N₂O₅ (in pptv) time series for the full duration of the individual experiments conducted on 10, 15, and 16 June 2007. In each time series, UAF data are represented by the filled circles and colored from yellow to purple with progressing time. The NOAA data are represented in each time series by grey lines. The time series data are presented at full time resolution (2 s for UAF data; 1 s for NOAA data) to show the dynamic response of each instrument to changing mixing ratios of N₂O₅.

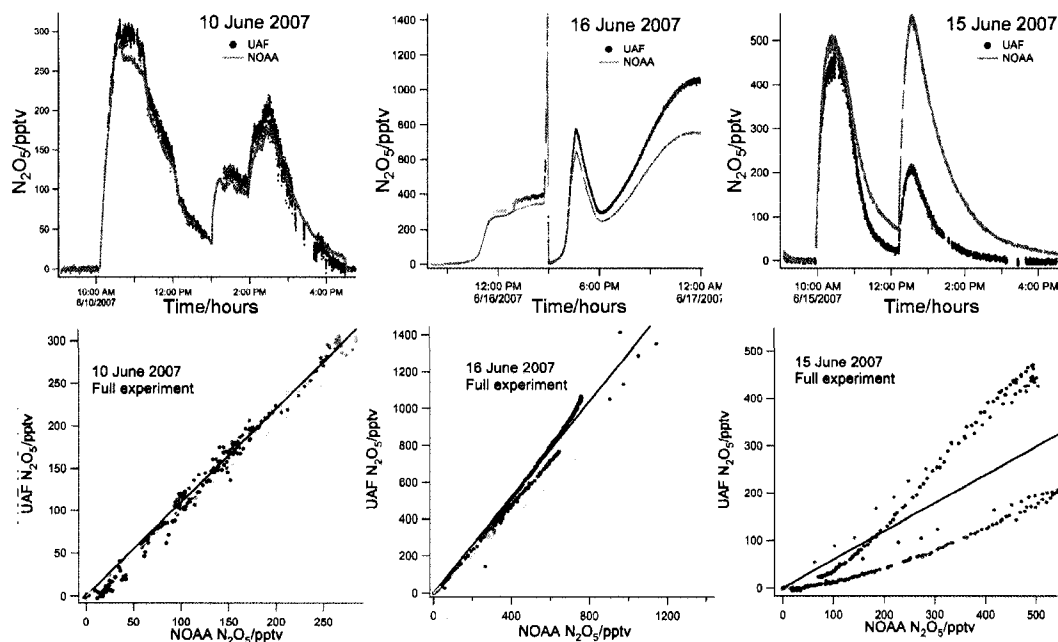


Fig. 3.2 Selected data from the UAF and NOAA instruments on 10, 15, 16 June. In the top row are time series of N_2O_5 mixing ratios, with UAF data colored with increasing time and NOAA data in grey. The bottom row shows correlation plots of UAF data vs. NOAA data. In the correlations, the black line is the regression and dashed grey line represents a 1:1 ratio.

Example correlation plots showing the agreement of measurement between the UAF (vertical axes) and NOAA (horizontal axes) are shown in the bottom row of fig. 3.2. Here, all data are averaged to 60 s for comparison purposes. In the correlation plots, the solid black lines are the linear regressions, the dashed grey lines are the 1:1 ratio, and the data are colored for progressing time (using the same color/time coding presented in the time series for each day). The correlations and regressions from the entire campaign are presented in table 3.2. The regressions yield slopes ranging from 0.59 ± 0.015 ($1-\sigma$ error) to 1.30 ± 0.003 .

Table 3.2 Results of the correlations and regression from the 12 experimental days. Note that 8 out of the 12 days demonstrate slopes that are within 15% of unity. All intercepts were forced to zero in order to achieve the best fit for the regressions.

June (2007)	<i>N</i>	r^2	Slope $m \pm 1-\sigma$
9	237	0.99	1.00±0.003
10	294	0.99	1.10±0.003
11	275	0.99	0.837±0.004
12	281	0.99	1.01±0.002
13	80	0.99	0.93±0.01
14	358	0.99	0.99±0.002
15	349	0.72	0.59±0.015
16	690	0.99	1.30±0.003
17	422	0.99	1.22±0.002
18	717	0.99	1.147±0.002
20	452	0.98	0.95±0.004
21	464	0.99	0.993±0.003

The correlation and regression analysis from the individual experiments show excellent agreement between the UAF and NOAA instruments. However, close inspection of table 3.2 brings to light three distinct categories within the data. First, the correlation slopes on 8 out of 12 days (June 9, 10, 12, 13, 14, 18, 20, and 21) are within 15% of unity, demonstrating high agreement and similar performance between the UAF and NOAA instruments. The experimental conditions of this high-agreement category were quite varied with respect to O₃, NO_x, and water vapor levels in the SAPHIR chamber (see table 3.1). Nevertheless, the data collected on these days show no evidence that the varied chemical conditions produced interferences or systematic differences with the performance of either instrument. In fig. 3.2, 10 June was selected to demonstrate the high agreement between the two instruments under conditions of high relative humidity and elevated NO₂ and O₃.

Second, on experimental days 16 and 17 June the correlation slopes were more than 15% above unity. The data from 16 June is shown as an example of this category as it demonstrates the largest (30%) deviation above unity. Throughout the campaign, flow variation tests were conducted to derive loss estimates for the UAF instrument (as described in chapter 2). Figure 3.3 shows the filter transmissions plotted against filter age. The best fit to the data gave an initial transmission of 91%. Furthermore, the test result suggested that the transmission decreased with a slope of -1.3% per hour of sampling, resulting in a decaying filter transmission. The decaying filter transmissions were used to correct all of the UAF data.

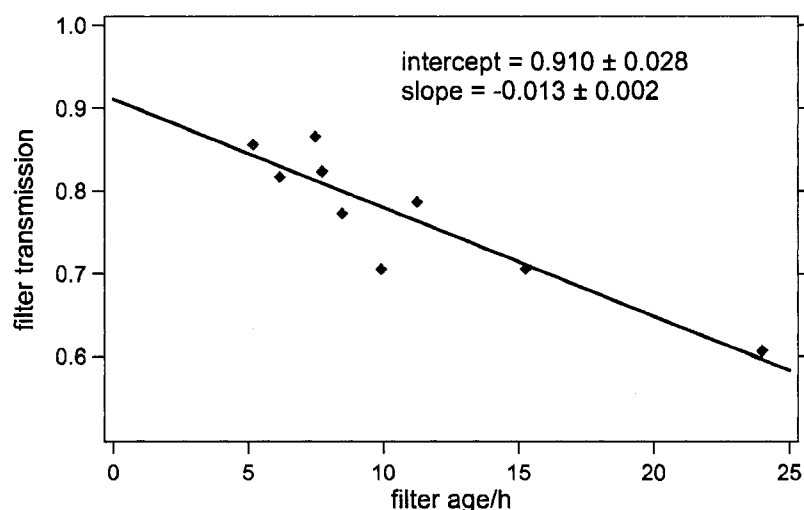


Fig. 3.3 A plot of filter transmission against filter age. The green diamonds are filter transmissions determined while aerosol particles were in the SAPHIR chamber. The red diamonds are filter transmissions collected in the absence of aerosol particles and the black trace is the linear regression. The negative slope of the regression is strongly influenced by the lowest filter transmission (~ 0.60). The results of the regression were used to correct the UAF N_2O_5 data for filter loss (see text).

The higher N_2O_5 levels detected by the UAF instrument on 16, 17, and 18 June are consistent with a correction factor of 1.3% per hour being excessive under the

experimental conditions on these days. The over-correction applied to the UAF data is most clearly noted on 16 June (see fig. 3.2). Here, the duration of the experiment was quite long, resulting in increasing divergence between the UAF and NOAA data as the experiment progressed. It is clear that under these conditions, the filter transmission did not decay during the course of the experiment.

The third and final category consists of the experiments conducted on 11 and 15 June. Here, the correlation slopes were greater than 16% below unity on the 11th and 41% below unity on the 15th. The experiments in this category were conducted with elevated inorganic aerosol and high relative humidity in the SAPHIR chamber. Using 15 June as an example of the low slope category, fig. 3.2 shows that agreement between the two instruments was good early in the experiment on 15 June, but decreased significantly as the experiment progressed. Similar results were seen during the experiment on 11 June. An important note here is that the NOAA inlet filters were replaced once per hour during each experiment, using an automated filter changer. The frequent filter changes in the NOAA instrument prevented significant N₂O₅ loss caused by soiled filters. In contrast, a new filter was placed in the UAF instrument only at the beginning of each experiment. As a result, under the high-aerosol and high-relative humidity conditions on 11 and 15 June, the UAF instrument experienced large N₂O₅ filter losses that increased with increasing filter loading.

Lastly, a correlation and regression analysis of the combined data set for all 12 experimental days shows excellent overall agreement between the instruments (fig. 3.4, left panel). The regression for the campaign-wide data set yields a slope of 0.958 ± 0.002

and a correlation coefficient $r^2 = 0.99$. Of note in the campaign-wide regression (fig. 3.3, left panel) is the decreased agreement between the instruments at N_2O_5 mixing ratios above 6000 pptv, which were measured during the 20 June experiment. The right panel of fig. 3.4 is a correlation plot for all campaign days except for 20 June. By removing the 20 June data, the correlation slope becomes approximately equal to unity, a 4% improvement of the campaign-wide data set.

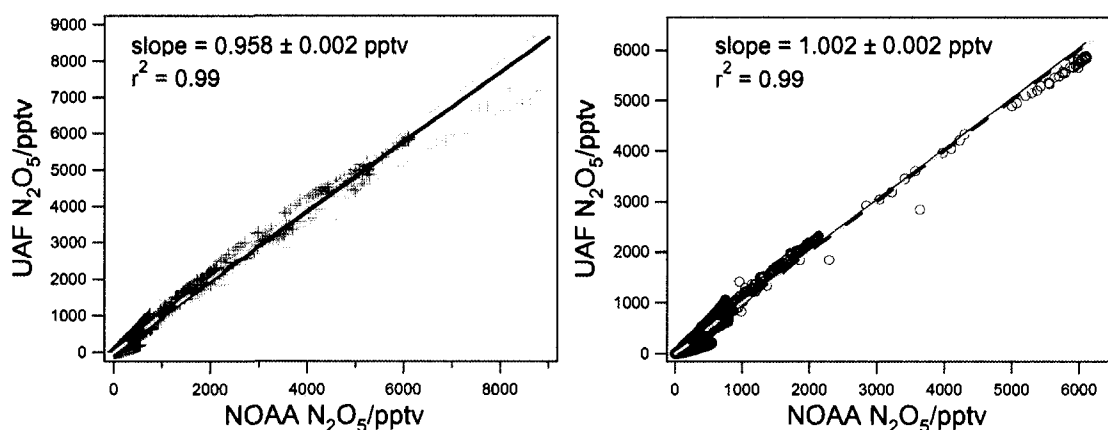


Fig. 3.4 UAF vs NOAA correlations plots. Left panel: Correlation plot of the combined data set from the entire intercomparison. The red crosses are the data, the black line is the regression, and the dashed grey line is the 1:1 ratio. Note the lower agreement between the two instruments at N_2O_5 mixing ratios greater than 6000 pptv. These high N_2O_5 data were collected during the 20 June experiment. Right panel: Correlation plot of the entire campaign, but with the 20 June data removed. The red circles are the data, the black line is the regression, and the dashed grey line is the 1:1 ratio. In both instances, excellent overall agreement between the UAF and NOAA data is observed, but after removing the 20 Jun data the slope is improved by approximately 4%.

While the exact cause of the decreased agreement between the UAF and NOAA instruments at high N_2O_5 mixing ratios is not fully understood, one possible explanation is that the temperature-tuned diode laser (see chapter 2) in the UAF instrument malfunctioned. The UAF instrument was designed for operation under cold conditions at high latitudes, but during the intercomparison campaign it was not uncommon for the air

temperature around the instrument to reach 35°C. The possibility exists that, at times, the peak wavelength of the laser output not centered near 662 nm due to operating at elevated ambient temperatures. Subsequently, the N₂O₅ mixing ratios would be determined with an incorrect absorption cross section, which could potentially result in an under-determination of N₂O₅. As discussed above, excluding the 20 June data set from the regression analysis, due to possible instrument malfunction, results in a slope very close to unity. Future improvements to the UAF instrument should include real-time wavelength monitoring and better temperature control of the diode laser module in order to detect and prevent malfunction of the laser.

3.3.2 Initial 2 hour data

The correlations and regressions of the data shown in fig. 3.5, as well as in table 3.3 were derived using data from the first 2 hours of each experiment. Selecting the data to include only the initial 2 hours of each experiment allows for an instrument comparison that minimizes the effects of the over-correction and N₂O₅ loss due to filter loading seen in the UAF data, as described in the previous section. The regressions conducted on the data from the initial 2 hours of each experiment shows improved agreement, as evidenced by a narrowed range of observed slopes (0.88 ± 0.01 to 1.23 ± 0.01), when compared to the full-duration data described above. Furthermore, with $r^2 = 0.99$ for all experiments, the correlation between the two instruments is also improved.

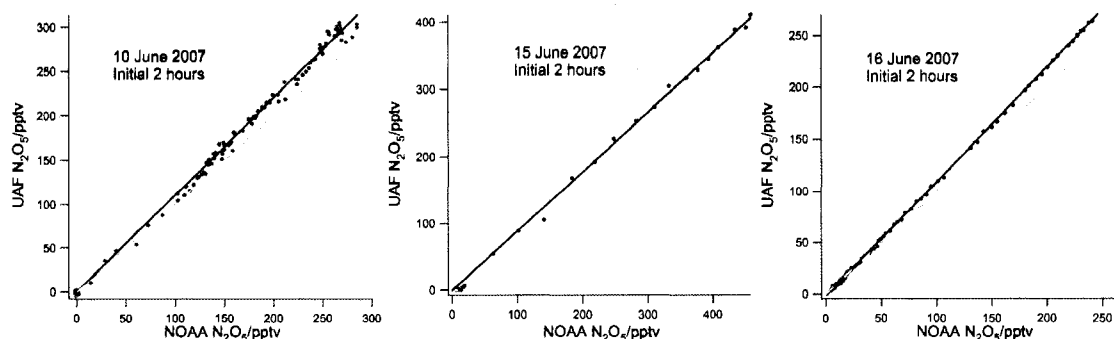


Fig. 3.5 Correlation plots of the initial 2 hours of the experiments conducted on 10, 15, and 16 June. The black lines are the regressions and dashed grey lines represent a 1:1 ratio. The data are colored for progressing time (see text and table 3.3 for slopes).

Table 3.3 Results of the correlations and regression from the initial 2 hours of each experiment. All intercepts were forced to zero in order to achieve the best fit for the regressions.

June (2007)	N	r^2	Slope $m \pm 1-\sigma$
9	132	0.99	0.97 ± 0.01
10	140	0.99	1.10 ± 0.01
11	90	0.99	0.90 ± 0.003
12	96	0.99	0.94 ± 0.01
13	66	0.99	0.90 ± 0.01
14	83	0.99	0.89 ± 0.01
15	60	0.99	0.88 ± 0.004
16	161	0.99	1.10 ± 0.001
17	95	0.99	1.23 ± 0.01
18	309	0.99	1.08 ± 0.004
20	115	0.99	0.96 ± 0.003
21	245	0.99	0.96 ± 0.002

Figure 3.6 shows the correlation and regression for the combined 2 hour data set for all 12 experimental days. Here, the regression yields an improved campaign-wide slope of 0.963 ± 0.001 when compared to the full data set regression. The initial 2 hour data set also produces fewer outliers than the full-duration data set, and has a campaign-wide correlation coefficient of $r^2 = 0.99$.

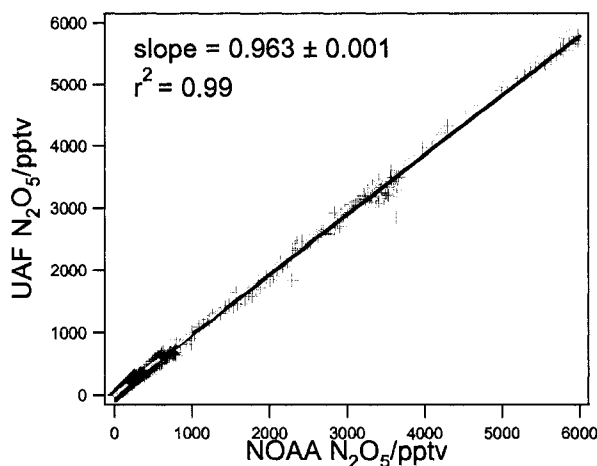


Fig. 3.6 Correlation of the combined 2 hour data set for all 12 experimental days. The red crosses are the data, the black line is the regression, and the dashed grey line is the 1:1 ratio. Improved overall agreement between the UAF and NOAA data is observed as compared to the full-duration combined data set.

3.3.3 Instrument accuracy and detection sensitivities

The accuracy of the UAF N₂O₅ instrument was estimated based on the uncertainties in the transmission efficiency of the measurement cell for N₂O₅ and NO₃, the uncertainty in the peak cross section for NO₃, and the uncertainty of the measurement of L/L_a (see chapter 2) or the percentage of the cell filled with N₂O₅. From the data presented in fig. 3.3, the average value for N₂O₅ transmission is 0.77 with a 1σ uncertainty of 10%. The uncertainty for NO₃ transmission was reported as 17% (Dorn et al., 2008). As discussed in chapter 2, we used temperature dependent cross section values for NO₃ at 662 nm reported by Yokelson et al. (1994), where the stated uncertainty is 10%. Finally, the ratio L/L_a was estimated from physical dimensions of the measurement cell and we assume an uncertainty of 10%. Combining the uncertainties described here, we estimate the total uncertainty of the UAF N₂O₅ measurements to be approximately 25%. For a full description of the N₂O₅ accuracy for the NOAA

instrument, the reader is referred to Dube' et al. (2006), where the N_2O_5 measurement uncertainty is reported to range from 20 to 40%.

Actual detection limits for the UAF and NOAA instruments were determined from data when N_2O_5 was not present in the SAPHIR chamber. Throughout the campaign, it was standard procedure to purge the SAPHIR chamber with zero air between experiments in order to remove residual gases and aerosol particles. To preclude the detection of significant N_2O_5 , we determined instrument detection limits from 2.5 h of data collected on 6 different days subsequent to purge periods. Histograms for the N_2O_5 data during these periods are shown in fig. 3.7. With a 2 s time resolution, the UAF data demonstrate a mean of 0.59 pptv N_2O_5 and a standard deviation of 1.47 pptv N_2O_5 . The NOAA data have a mean of -0.14 pptv N_2O_5 with a standard deviation of 1.72 pptv N_2O_5 in 1 s.

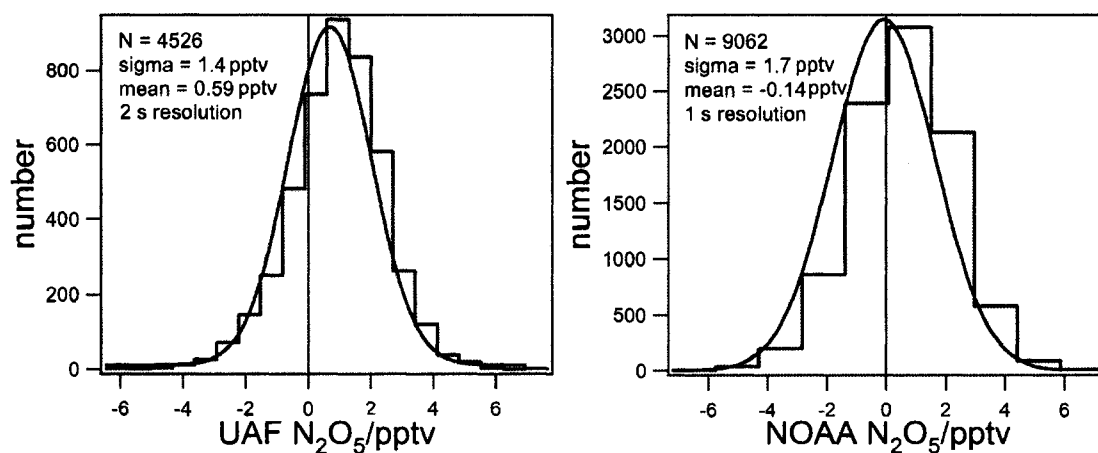


Fig. 3.7 Histograms of N_2O_5 measurements made subsequent to the chamber being purged with zero air, precluding significant levels of N_2O_5 . These histograms represent the noise of each instrument and lead to 2σ detection limits of 2.8 pptv N_2O_5 in 2 s for UAF and 3.4 pptv N_2O_5 in 1 s for NOAA. See text for a comparison of detection limits averaged to the same time base.

While the calculated noise-equivalent detection limits for each instrument were described above, the data in fig. 3.7 allow for the derivation of actual detection limits that are representative of instrument performance under field conditions. Taken at instrument-native time resolutions, the 2σ detection limits are 2.8 pptv N_2O_5 in 2 s for the UAF instrument and 3.4 pptv N_2O_5 in 1 s for the NOAA instrument. When averaged to 2 s, for comparison to the UAF detection limit, the NOAA 2σ detection limit is quite similar at 2.4 pptv.

3.4 Conclusions

We have presented results from the first intercomparison of field instruments designed to measure N_2O_5 . The intercomparison results show that the N_2O_5 measurements made by the UAF oa-CRDS instrument and the NOAA pulsed-CaRDS instrument are in overall excellent agreement. The SAPHIR reaction chamber was an ideal location for conducting the intercomparison, allowing for control over the trace gas composition, relative humidity, aerosol levels and composition, and lighting conditions.

With respect to O_3 , NO_x , and water vapor levels in the SAPHIR chamber, no systematic differences in performance were found between the UAF and NOAA instruments. Both instruments demonstrated time resolutions and measurement ranges that are fully sufficient for making real-time N_2O_5 observations in the atmosphere, even at aircraft flight speeds. Furthermore, the 2σ detection limits reported here show that both the UAF instrument and NOAA instrument are capable of probing ambient air masses to the lower limit of expected N_2O_5 levels.

The UAF data demonstrate that experiments conducted with elevated aerosol levels, particularly inorganic aerosol under high relative humidity conditions, show large N_2O_5 filter losses that increase with increasing loading of aerosol on the filter. The same result is not seen in the NOAA data, which can be attributed to the high frequency with which the filters are replaced in this instrument. Furthermore, similar losses have not been observed in the field data collocated near Fairbanks, AK, with the UAF instrument or with a similar N_2O_5 apparatus employing the same filtering scheme (Simpson, 2003). The non-decaying transmission in the field data is likely the result of lower particulate levels in the Fairbanks air as compared to the levels seen in the SAPHIR reaction chamber. It is also important to note that the inorganic aerosol studies were conducted at elevated relative humidities in the SAPHIR chamber while the Fairbanks studies were conducted on differing relative humidities. Therefore, differences in relative humidity could be the cause of differences in filter decay. Lastly, it is possible that the aerosol generated around Fairbanks is of a significantly different chemical composition than the aerosol observed in this intercomparison. Regardless of the exact loss mechanism, this intercomparison demonstrated that considerations must be made for aerosol loading to filters. The excellent agreement between the UAF and NOAA instruments seen in the first 2 hours (results taken with low aerosol loading on the filter), as well as the general results of the NOAA instrument (with filter changes occurring on an hourly basis), suggest that it is best procedure to change inlet filters frequently while sampling airmasses with elevated aerosol levels.

Lastly, it appears that the filter transmissions do not decay significantly with time in the absence of inorganic aerosol particles at high humidity, nor does the transmission appear to decay rapidly in low-aerosol conditions. The assumption of decaying filters in all experiments lead to an over-correction for filter loss in the UAF data. This over-correction is particularly clear in experiments with long durations.

A few open questions still remain with respect to the impact of aerosol particles on filter transmission. Namely, it is unclear whether it is aerosol chemical composition or aerosol loading that has the greatest impact on filter transmission. Furthermore, it is unclear if filter loss caused by aerosol particles demonstrates a dependence on relative humidity. Careful characterization of filter transmission in the presence of aerosols, under variable relative humidity, would allow for improvements in the operational procedures of N_2O_5 instruments that would subsequently improve instrument performance. Nevertheless, the results of this intercomparison have shown that both oa-CRDS and pulsed-CRDS are highly effective and valuable tools for studying nocturnal nitrogen oxide chemistry by providing a means for reliably measuring ambient N_2O_5 .

3.5 References

- Apodaca, R.L., W. R. Simpson, S. M. Ball, T. Brauers, S. S. Brown, R. C. Cohen, J. Crowley, H.P. Dorn, W. P. Dube, J. Fry, H. Fuchs, R. Haseler, U. Heitmann, S. Kato, Y. Kajii, A. Kiendler-Scharr, I. Labazan, J. Matsumoto, S. Nishida, R. Tillmann, F. Rohrer, E. Schlosser, G. Schuster, A. Shillings, R. Tillmann, A. Wahner, R. Wegener, and P. J. Wooldridge, Intercomparison of N_2O_5 sensors using SAPHIR reaction chamber. In preparation (2008), Atmos. Chem. Phys. Discuss.
- Atkinson, D. B., 2003. Solving chemical problems of environmental importance using cavity ring-down spectroscopy, *Analyst*, 128, 117-125.
- Ayers, J. D.; Apodaca, R. L.; Simpson, W. R.; Baer, D. S., 2005. Off-axis cavity ringdown spectroscopy: application to atmospheric nitrate radical detection. *Applied Optics*, 44, (33), 7239-7242.
- Ball, S. M.; Langridge, J. M.; Jones, R. L., 2004. Broadband cavity enhanced absorption spectroscopy using light emitting diodes. *Chemical Physics Letters*, 398, (1-3), 68-74.
- Ball, S. M.; Povey, I. M.; Norton, E. G.; Jones, R. L., 2001. Broadband cavity ringdown spectroscopy of the NO_3 radical. *Chemical Physics Letters*, 342, (1-2), 113-120.
- Brown S.S., Stark H., Ciciora S.J., McLaughlin R.J., and Ravishankara A.R., 2002. Simultaneous in situ detection of atmospheric NO_3 and N_2O_5 via cavity ring-down spectroscopy. *Rev Sci Instr.* 73 (9): 3291-3301.
- Dorn, H.P., R.L. Apodaca, S. M. Ball, T. Brauers, S. S. Brown, R. C. Cohen, J. Crowley, W. P. Dube, J. Fry, H. Fuchs, R. Haseler, U. Heitmann, S. Kato, Y. Kajii, A. Kiendler-Scharr, I. Labazan, J. Matsumoto, S. Nishida, R. Tillmann, F. Rohrer, E. Schlosser, G. Schuster, A. Shillings, W. R. Simpson, R. Tillmann, A. Wahner, R. Wegener, and P. J. Wooldridge, Intercomparison of NO_3 sensors using SAPHIR reaction chamber. In preparation (2008), Atmos. Chem. Phys. Discuss.
- Dube, W. P.; Brown, S. S.; Osthoff, H. D.; Nunley, M. R.; Ciciora, S. J.; Paris, M. W.; McLaughlin, R. J.; Ravishankara, A. R., 2006. Aircraft instrument for simultaneous, in situ measurement of NO_3 and N_2O_5 via pulsed cavity ring-down spectroscopy. *Rev Sci Instr.*, 77, (3).
- Finlayson-Pitts, B. J. and J. N. Pitts Jr. (2000), *Chemistry of the Upper and Lower Atmosphere*, pp. 969, Elsevier, New York.

- Fuchs, H., S. M. Ball, T. Brauers, S. S. Brown, R. C. Cohen, H.P. Dorn, W. P. Dube, J. Fry, R. Haseler, U. Heitmann, R. Tillmann, F. Rohrer, E. Schlosser, A. Shillings, A. Wahner, R. Wegener, and P. J. Wooldridge, Intercomparison of NO₂ sensors using SAPHIR reaction chamber. In preparation (2008), Atmos. Chem. Phys. Discuss.
- King M.D., Dick E.M., and Simpson W.R., 1999. A new method for the atmospheric detection of the nitrate radical (NO₃), Atmos. Env., 34,683-686.
- Kunde, V. G.; Brasunas, J. C.; Maguire, W. C.; Herman, J. R.; Massie, S. T.; Abbas, M. M.; Herath, L. W.; Shaffer, W. A., 1988. Measurement of nighttime stratospheric N₂O₅ from infrared-emission spectra. Geophysical Research Letters, 15, (11), 1177-1180.
- Matsumoto, J., Ksougi, N., Imai, H., and Kajii, Y. 2005, Development of a measurement system for nitrate radical and dinitrogen pentoxide using a thermal conversion/laser-induced fluorescence technique; Rev Sci Inst. 76 (6).
- Nakayama, T., Tomoyuki Ide, Fumikazu Taketani, Megumi Kawai, Kenshi Takahashi, Yutaka Matsumi. Nighttime measurements of ambient N₂O₅, NO₂, NO and O₃ in a sub-urban area, Toyokawa, Japan. Atmospheric Environment, 2008. 42(9), pp. 1995-2006.
- Noxon, J. F.; Norton, R. B.; Henderson, W. R., 1980a. Comment on the problem of nighttime stratospheric NO₃ Journal of Geophysical Research-Oceans and Atmospheres, 85, (NC8), 4556-4557.
- Noxon, J. F.; Norton, R. B.; Marovich, E., 1980b. NO₃ in the troposphere. Geophysical Research Letters, 7, (2), 125-128.
- Okeefe, A., and Deacon, D. A. G., , 1988. Cavity ring-down optical spectrometer for absorption-measurements using pulsed laser sources, Review of Scientific Instruments, 59, 2544-2551.
- Platt, U., D. Perner, G. W. Harris, A. M. Winer, and J. N. Pitts, 1980. Detection of NO₃ in the polluted troposphere by differential optical absorption, Geophys. Res. Lett., 7, 89-92.
- Rinsland, C. P.; Toon, G. C.; Farmer, C. B.; Norton, R. H.; Namkung, J. S., 1989. Stratospheric N₂O₅ profiles at sunrise and sunset from further analysis of the ATMOS/SPACELAB 3 solar spectra. Journal of Geophysical Research-Atmospheres, 94, (D15), 18341-18349.
- Schlosser, E.; Bohn, B.; Brauers, T.; Dorn, H. P.; Fuchs, H.; MatHaseler, R.; Hofzumahaus, A.; Holland, F.; Rohrer, F.; Rupp, L. O.; Siese, M.; Tillmann, R.; Wahner, A., 2007. Intercomparison of two hydroxyl radical measurement techniques at the

atmosphere simulation chamber SAPHIR. *Journal of Atmospheric Chemistry*, 56, (2), 187-205.

Schulz K.J., and Simpson W.R., 1998. Frequency-matched cavity ring-down spectroscopy. *Chem Phys Lett.* 297:523-529.

Simpson W.R., 2003. Continuous wave cavity ring-down spectroscopy applied to in situ detection of dinitrogen pentoxide (N_2O_5). *Rev Sci Instr.* 74 (7): 3442-3452.

Slusher, D. L.; Huey, L. G.; Tanner, D. J.; Flocke, F. M.; Roberts, J. M., 2004. A thermal dissociation-chemical ionization mass spectrometry (TD-CIMS) technique for the simultaneous measurement. *Geophysical Research-Atmospheres*, 109, (D19).

Wegener, R., Brauers, T., Koppmann, R., Rodriguez Bares, S., Rohrer, F., Tillmann, R., Wahner, A., Hansel, A., 180 Wisthaler, A., 2007. Investigation of the ozonolysis of short chained alkenes in the atmosphere simulation chamber SAPHIR, *J. Geophys. Res.*.

Wood E.C., Wooldridge P.J., Freese J.H., Albrecht T., and Cohen R.C., 2003. Prototype for in situ detection of atmospheric NO_3 and N_2O_5 via laser-induced fluorescence. *Environ Sci Technol.*, 37: 5732-5738.

Wood E.C., Bertram T.H., Wooldridge P.J., and Cohen R.C., 2005. Measurement of N_2O_5 , NO_2 , and O_3 east of the San Francisco Bay. *Atmos Chem Phys*, 4: 6645-6665.

Yokelson, R. J.; Burkholder, J. B.; Fox, R. W.; Talukdar, R. K.; Ravishankara, A. R., 1994. Temperature-dependence of the NO_3 absorption-spectrum. *Journal of Physical Chemistry*, 98, (50), 13144-13150.

Chapter 4:

The role of ice in N_2O_5 heterogeneous hydrolysis at high latitudes¹

4.1. Introduction

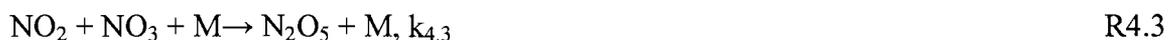
Tropospheric pollutants such as ozone and nitric acid (HNO_3) are of growing concern due to their environmental impacts and associated health concerns. Nitrogen oxides, particularly the rapidly cycling family referred to as NO_x (= nitric oxide, NO + nitrogen dioxide, NO_2), play a critical role in the production of ozone and HNO_3 in the troposphere. During the day, NO_x enters catalytic cycles that produce ozone, and in some locations the amount of ozone produced is considered hazardous to human health (Finlayson-Pitts and Pitts, 2000). NO_x can also destroy ozone at night (Brown et al., 2006a). From an atmospheric chemistry viewpoint, ozone is also important in that it controls many aspects of atmospheric oxidation processes. The ultimate fate of NO_x is to be oxidized to nitric acid and subsequently deposited to the surface of Earth. NO_x oxidation and removal limits the extent to which catalytic production of ozone occurs. Furthermore, deposition of HNO_3 generated by NO_x oxidation results in acid deposition and nitrogen fertilization, potentially altering soil and surface water pH and causing changes in biota in sensitive ecosystems (Andersen and Hovmand, 1995; Heintz et al., 1996; Allan et al., 1999; Bergholm et al., 2003; Fenn et al., 2003).

¹Apodaca, R.L.; D.M. Huff; W.R. Simpson. The role of ice in N_2O_5 heterogeneous hydrolysis at high latitudes. *Atmos. Chem. Phys. Discuss.*, 8, 1–30, 2008.

Atmospheric NO_x removal chemistry is diurnal in nature, with different processes occurring during day and night. Daytime NO_x removal is driven by the presence of the hydroxyl radical (OH) in the following reaction,



Nighttime removal of NO_x proceeds through the formation of the oxidative intermediates nitrate radical (NO_3) and dinitrogen pentoxide (N_2O_5) in what is termed the “dark” oxidation pathway.

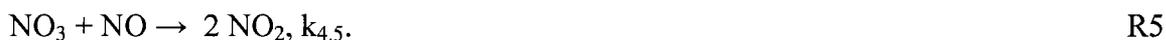


In recent years, multiple optical techniques have been developed to study this pathway (Platt et al., 1980; Geyer and Stutz, 2004; Stutz et al., 2004; King et al., 2000; Brown et al., 2001, 2002, 2003; Simpson, 2003; Wood et al., 2003; Ayers et al., 2005; Brown et al., 2006b; Nakayama et al., 2008). In a number of studies, these techniques have been used to determine NO_3 and N_2O_5 lifetimes, and one study has demonstrated the direct determination of the reactive uptake coefficient of N_2O_5 , $\gamma(\text{N}_2\text{O}_5)$, on ambient aerosol particles (Brown, et al., 2006b).

The landmark modeling study by Dentener and Crutzen (1993) suggests that the dark loss mechanism is the main loss process of nitrogen oxides at high latitudes in winter. Factors that contribute to the prominence of the dark oxidation pathway at high latitudes are outlined below. Long nights allow NO_3 to form without photolysis acting as

a major sink. Short days and low sunlight intensity result in low OH radical abundance that reduces the importance of the daytime NO_x oxidation pathway. Reactions R3 and R3' are half reactions of a temperature dependent equilibrium between NO₃ and N₂O₅.

Thermal dissociation of N₂O₅ (reaction R3') results in similar abundances of NO₃ and N₂O₅ under warm conditions. However, under cold conditions, such as at high latitudes, the dissociation rate of N₂O₅ slows, resulting in increased partitioning towards N₂O₅. As such, if heterogeneous hydrolysis rates are slow, N₂O₅ could potentially be transported long distances in cold air masses such as those found at higher latitudes or high altitudes. A factor that may moderate dark oxidation of NO_x is the fast reaction of NO with NO₃, which acts as a sink of NO₃.



Nitric oxide may be present either from direct emissions, which can persist at night in ozone-titrated air masses, or from photolysis of NO₂ in the day. Away from direct emissions (i.e. outside of a city) and under nighttime conditions, the NO sink is often small.

Ayers and Simpson (2006) have demonstrated that high latitude N₂O₅ lifetimes are significantly shorter than ones reported at lower latitudes. To characterize N₂O₅ removal mechanisms at high latitudes, we measured N₂O₅ using off-axis cavity ring-down spectroscopy, oa-CRDS (Ayers et al., 2005). With these data and measurements of aerosol particles and ice saturation conditions, we demonstrate that ice particles are largely responsible for catalyzing N₂O₅ heterogeneous hydrolysis at high latitudes.

4.2 Measurements

In-situ N_2O_5 mixing ratios were measured using an off-axis cavity ring-down spectroscopy (oa-CRDS) field instrument described in chapter 2, and based on the optical technique developed by Ayers et al. (2005). Briefly, ambient air is continuously pulled through a sampling cell at 8 standard liters per minute (slpm). A Teflon filter (47 mm Pall Teflo membrane, 2.0 μm pore size) is housed at the mouth of the inlet to minimize particulate flow into the cavity and is changed every 3 to 4 hours to prevent sample loss due to contaminated filters. The all-Teflon analysis cell is heated to measure the sum of $\text{NO}_3 + \text{N}_2\text{O}_5$. The sample first passes through a stage where it is heated to 100°C, rapidly dissociating the N_2O_5 to $\text{NO}_3 + \text{NO}_2$ (reaction 3'). The sample then enters the second stage where it is probed by measuring direct absorption of NO_3 at 662 nm. The sample is maintained at 85°C in the second stage to prevent repartitioning back to N_2O_5 .

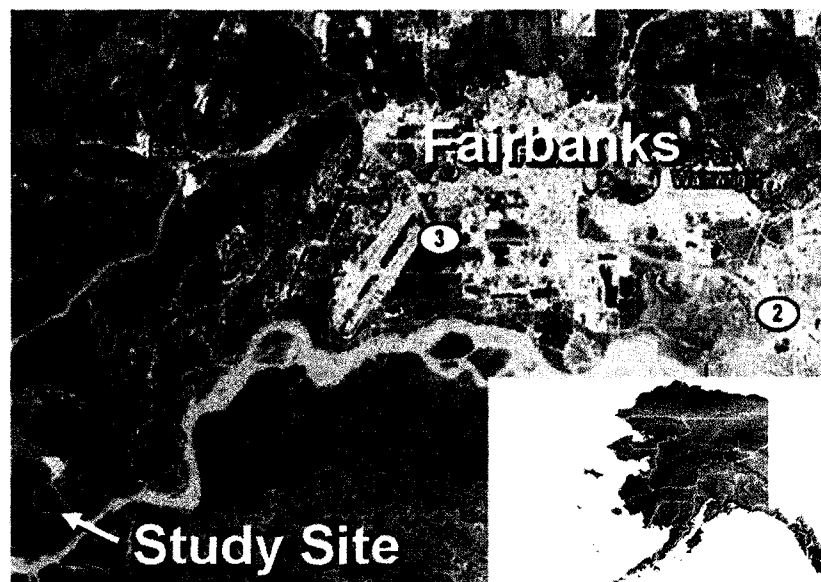


Fig. 4.1 A satellite image showing the study site location and its relationship to Fairbanks and the surrounding area. The map inset shows the location of Fairbanks in interior Alaska.

The measurements were made at a remote field site located about 20 km WSW of downtown Fairbanks, Alaska (Fig. 4.1). Fairbanks and the surrounding area have a population of approximately 80,000 people, making it the second largest population center in Alaska. Fairbanks is geographically isolated, particularly from other NO_x sources, with the nearest major city more than 400 km to the south and separated by the Alaska Range with typical elevations ranging from 2,000 m to 3,000 m. Therefore, the nitrogen oxides measured in this study are generated in the Fairbanks area without contribution from other regional sources. The study site (64.75°N , 148.09°W ; 135 m elev.) was located in a 45-acre agricultural field, cleared of trees and covered by seasonal snow pack throughout the duration of the study. To the north lie the hills of the Tanana uplands with peak elevations of about 1000 m. To the south lie the Tanana River and

expansive Tanana flats with an elevation of about 130 m. The predominant winds during this study were from the NNE, resulting in the site being at least 20 km downwind from the nearest large NO_x source, the city of Fairbanks. Radiative cooling resulted in cold temperatures during the study period with strong temperature inversions and highly stratified air. Strong temperature inversions coupled with the topography and weak winds made the study site ideal for observing the isolated Fairbanks pollution plume after significant transport and aging time.

The study was conducted continuously from 7 November 2007 through 19 November 2007. The oa-CRDS instrument was mounted outdoors and the inlet was maintained at 1 m above the snowpack surface. Ancillary measurements of NO and NO₂ were collected using a Thermo Environmental 42c NO_x analyzer. Ozone measurements were collected using a Dasibi 1008 RS instrument. Aerosol particle number density were made with a condensation particle counter (TSI CPC 3010) that had a lower size cutoff of approximately 10 nm. A 3-stage modified DRUM impactor and ion chromatography analysis were used to estimate a size distribution and determine the chemical composition of aerosol particles (Perry et al., 1999; Cahill, 2003). The DRUM impactor was operated in a mode where aerosol particles were impacted on a spot on a Teflon strip. After two hours of sample acquisition, an automated stepping motor moved the impaction location to a separate spot. The spots were visible on the strip due to black carbon present in the aerosol, and were cut out and eluted in ultra-pure water and analyzed by ion chromatography (Dionex ICS-2000). Wind speed, wind direction, and air temperature data were collected at the 1 m inlet elevation using an onsite meteorological tower

(Campbell Scientific). Relative humidity data were provided by hygrometers (Campbell Scientific Model HMP45C) located near the study site at the Bonanza Creek Experimental Forest and Long-Term Ecological Research station (Chapin, 2007). Relative humidity data used in this study were collected at site LTER2.

4.3 Nocturnal nitrogen oxide partitioning

For simplicity of discussion, we refer to nocturnal nitrogen oxides as NO_N and define them as the sum of $\text{NO}_3 + \text{N}_2\text{O}_5$. The formation of NO_N is the result of oxidation of NO_2 by ozone to form NO_3 , reaction R4.2. Subsequent conversion to N_2O_5 (reaction R3) proceeds rapidly. For example, at NO_2 levels of 5 ppbv, typical conditions during our study, the lifetime of NO_3 with respect to the formation of N_2O_5 is 5 seconds. In comparison, the thermal dissociation lifetime of N_2O_5 to form $\text{NO}_3 + \text{NO}_2$ (reaction R3') is 4 hours at -20°C . The result is that once NO_2 is formed, NO_N spends very little time as the nitrate radical before partitioning to N_2O_5 , and $\text{NO}_N \approx \text{N}_2\text{O}_5$. Under typical study conditions, the NO_3 abundance is negligible and the reactive losses of nitrate radical are generally too slow to compete with partitioning to N_2O_5 . The only processes fast enough to compete for reaction of NO_3 with formation of N_2O_5 is the fast reaction of NO with NO_3 (R5) and to a lesser extent, the daytime photolysis of NO_3 . For NO levels greater than 1 ppbv, the reactive sink NO_3 (with NO) is very important as it becomes faster than formation of N_2O_5 . Thus, only nighttime data at low NO will be considered for detailed lifetime analysis.

4.4 Steady state lifetimes and other considerations

Assuming steady state for N_2O_5 and NO_3 , and negligible losses for NO_3 , the kinetic expression for N_2O_5 is given by,

$$\frac{d[\text{N}_2\text{O}_5]}{dt} = k_3[\text{NO}_2][\text{NO}_3] - k_3'[\text{N}_2\text{O}_5] - k_4[\text{N}_2\text{O}_5]. \quad \text{eqn. 4.1}$$

With rearrangement, this equation becomes

$$\tau(\text{N}_2\text{O}_5)_{\text{SS}} = \frac{1}{k_4} = \frac{[\text{N}_2\text{O}_5]}{k_2[\text{NO}_2][\text{O}_3]}, \quad \text{eqn. 4.2}$$

where, $\tau(\text{N}_2\text{O}_5)$ is the steady state lifetime of N_2O_5 with respect to losses.

Brown, et al. (2003) use a simple box model to demonstrate that the applicability of the steady state approximation to NO_3 and N_2O_5 atmospheric observations depends upon the strength of sinks for NO_3 and N_2O_5 , the concentration of NO_2 , and the ambient temperature. Model results indicate that, in polluted air masses (i.e. large NO_2 mixing ratios) and cold conditions, when NO_3 and N_2O_5 sinks are weak, the approach to steady state can be slow. In their simulations, the timescale of the approach to steady state can exceed the duration of a typical dark period (>12 hours). Under such conditions, the steady state approximation would not be valid. However, as will be shown below, if the losses of N_2O_5 are sufficiently fast, the system achieves steady state on a rapid timescale, and we argue that our data indicate that the system does achieve steady state.

In the case where NO_3 losses can be ignored, the rate-limiting step for loss of N_2O_5 is the heterogeneous hydrolysis reaction (R4.4). Therefore, the kinetic expression for N_2O_5 (eqn. 4.1) simplifies to an exponential approach to steady state with relaxation

time (the time to reach 63% = $1 - e^{-1}$ of steady state) equal to the loss lifetime of N_2O_5 . Generally, the behavior of N_2O_5 can be considered in the context of fast and slow losses. If losses of N_2O_5 are fast, then the system achieves steady state on a fast timescale. If losses of N_2O_5 are slow, then it is useful to consider the source rate of NO_N (reaction R4.1, with a rate of $k_2[NO_2][O_3]$). This source rate is easily calculated from the observed data, and for the case of slow losses, the kinetic expression of N_2O_5 (eqn 4.1) shows that $d[N_2O_5]/dt$ is equal to the source rate. Thus, in the limit of short plume-processing times compared to the N_2O_5 loss lifetime, N_2O_5 should increase as the integral of its source rate. Therefore, we can examine the temporal behavior of N_2O_5 in an aged air mass to determine if it is near steady state or not. If the system has a short inferred lifetime and follows the source rate with lags on the order of the inferred lifetime, we would indicate that it is near steady state. Alternatively, if N_2O_5 increases at as the integral of the source rate, the system is clearly not at steady state.

4.5 Results

Figure 4.2 shows the timeseries of NO , NO_2 , O_3 , N_2O_5 for the entirety of the campaign. All data are recorded at instrument-native time resolutions (typically 1-2 seconds) and averaged to 1 minute data for analysis. N_2O_5 abundance (upper panel) varies from a maximum near 100 pptv (parts per trillion by volume) to sub-detection limit. When N_2O_5 is present, diurnal variation is evident with lower levels during the day (shaded background regions) and highest levels occurring at night. However, note that when NO is low in the day, the low sunlight intensity of late November in Fairbanks ($65^\circ N$) allows significant N_2O_5 levels to exist in the day. NO_2 and NO levels range from

near zero to a maximum of about 20 ppbv. Low levels of fresh pollution at the study site are evidenced by the low levels of NO for most of the study. A notable exception of NO occurring at night was observed during a highly polluted “ozone titration” event on 16 and 17 November. Ozone levels range from below the instrumental detection limit to around 35 ppbv. Regional background ozone levels in the Fairbanks area during November are typically near 35 ppbv, and thus we observe significant O₃ losses, most probably contributed to by the nocturnal ozone loss associated with the dark NO_x oxidation pathway (Brown et al. 2006a).

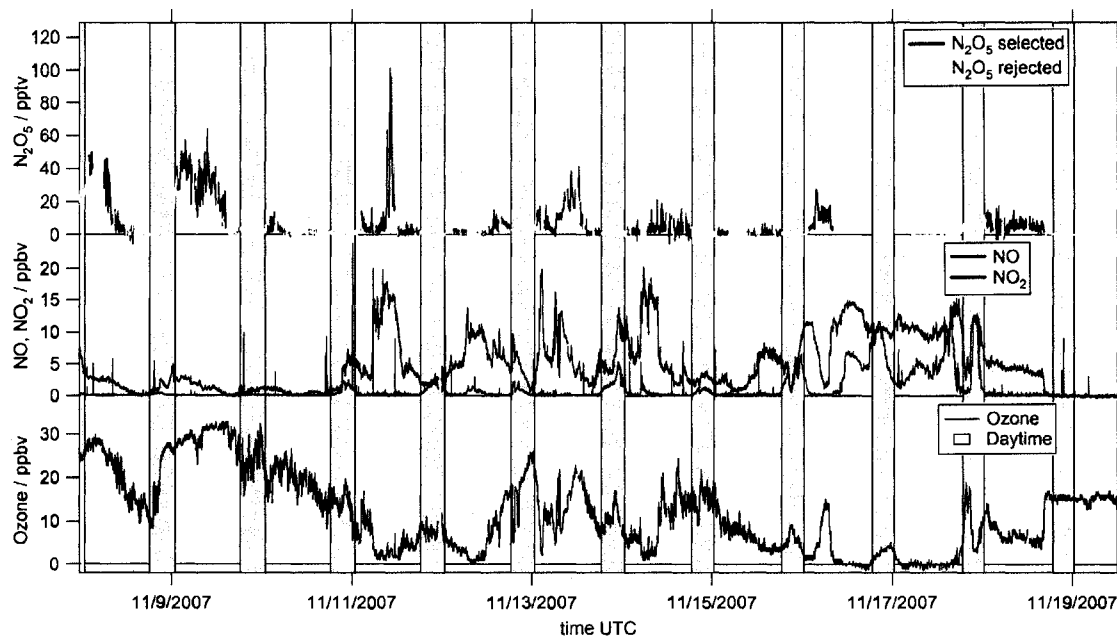


Fig. 4.2 Time series of N₂O₅, NO, NO₂, and ozone mixing ratios from the campaign. N₂O₅ data are filtered as described in section 4.5 and are colored blue for selected data and yellow for rejected data.

As discussed above, certain conditions are amenable to formation of N₂O₅, and thus we want to identify conditions where N₂O₅ should be forming, enabling the observation of its loss processes. We color the N₂O₅ data in Fig. 4.2 and all subsequent

plots by the code of yellow for “rejected” values, where trivial losses of N_2O_5 preclude lifetime analysis, and dark blue for “selected” values, where N_2O_5 should be forming sufficiently rapidly to warrant lifetime analysis. The conditions we use to identify selected data are: 1) The sun is below the horizon. 2) NO is less than 1 ppbv. Exceeding this threshold would indicate that the air mass is titrated of ozone or impacted by a local plume and NO_3 is rapidly lost. 3) Both of these conditions have been valid for at least a half hour. And 4) that the source rate of N_2O_5 is more than 10 pptv/hr, which is meant to preclude analysis of very clean (unpolluted) airmasses.

4.6 Discussion

4.6.1 Validity of the steady state approximation

Steady state lifetimes were calculated for the entirety of the study, using N_2O_5 , NO_2 , and O_3 measurements and estimates for k_2 based on NASA/JPL recommendations (Sander et al., 2006). Lifetimes ranged from sub-minute to roughly 2 hours, with a median value of about 10 minutes. These values are in agreement with previous measurements in Fairbanks (Ayers and Simpson, 2006). Figure 4.3 shows the steady state lifetimes, N_2O_5 source rate, and N_2O_5 abundance for two selected periods during the study and can be used to further confirm the applicability of the steady state approximation.

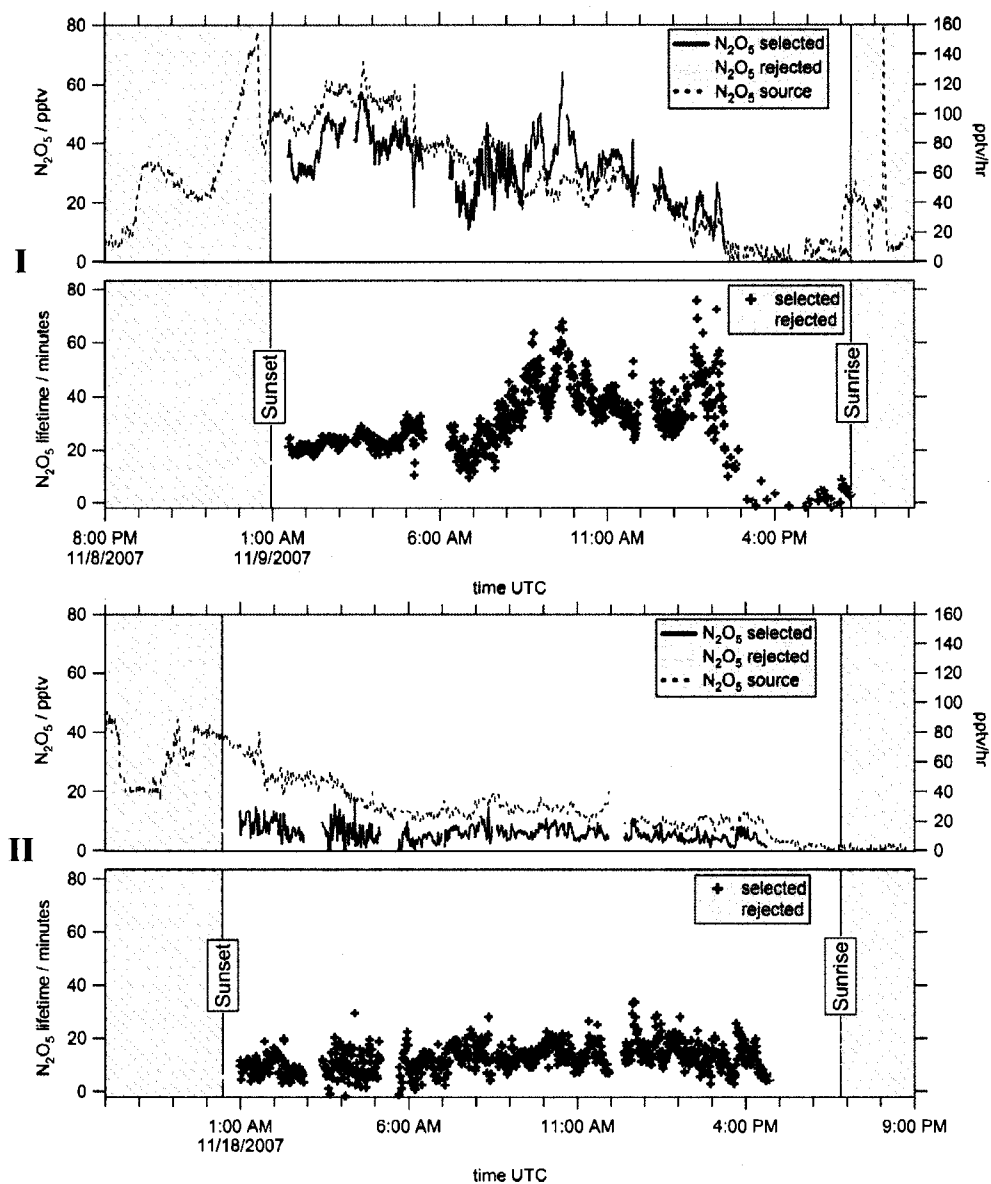


Fig. 4.3 N_2O_5 steady state lifetimes, source rates, and mixing ratios for two representative periods of the campaign. N_2O_5 mixing ratios and $\tau(N_2O_5)$ are colored to differentiate rejected (yellow) and selected (blue) data. Period I is representative of times where N_2O_5 abundance was elevated and $\tau(N_2O_5)$ reached its higher limits. Period II is representative of times where N_2O_5 abundance was suppressed and $\tau(N_2O_5)$ were short. Period I clearly shows N_2O_5 building to steady state levels with the onset of sunset. Note that at no point in either time series does N_2O_5 build at the source rate, an indication of rapid loss of N_2O_5 .

In Fig. 4.3, period I is an example of times where N_2O_5 abundance was elevated (greater than 20 pptv) and when longer steady state lifetimes were observed (20 to 60 minutes). Period II is representative of periods with suppressed N_2O_5 abundance (less than 20 pptv) and short steady state lifetimes (less than 20 minutes). The absence of N_2O_5 in the early times of periods I and II is due to rapid losses associated with daytime conditions (reaction with daytime NO and NO_3 photolysis). As nightfall occurs, the build-up of N_2O_5 progresses until shortly after sunset when N_2O_5 levels stabilize and reach relatively steady conditions, clearly following source rate fluctuations with only small lags.

Multiple lines of arguments support the validity of the steady state analysis. First, during the entirety of the study, wind speeds in the lowest 1200 m of the troposphere were typically below 3 m/s. Thus, the shortest processing times for air masses can be estimated by considering that the nearest NO_x source is minimally 20 km up wind (depending upon actual air mass trajectory). At maximal windspeeds, a minimum transport time of 2 hours is required for the air mass to reach the study site. Therefore, most air masses are more aged than a couple hours, allowing sufficient time for steady state lifetimes of less than a few hours to be observed. However, we observe steady state lifetimes typically on the order of tens of minutes, indicating losses on timescales shorter than typical transport times.

Second, the discussion above indicated that if the actual lifetime of N_2O_5 is long compared to the processing timescale, the temporal behavior of N_2O_5 should be increasing at the integral of the source rate. We do not observe the N_2O_5 mixing ratio

behaving as the integral of the source rate, but instead following the source rate on the timescale of less than an hour. This behavior indicates significant losses of N_2O_5 on the timescale of an hour or less, again validating the idea that these air masses have had sufficient time to reach steady state.

Third, referring to Fig. 4.2, we can consider that nearly all of these air masses have experienced loss of odd oxygen ($\text{O}_x = \text{NO}_2 + \text{O}_3$). For fresh pollution at night, O_x is conserved (Brown et al., 2006a), and thus loss of O_x indicates chemical aging. Considering the fact that polluted plumes experience initial nighttime O_x loss at rates of about 1 ppbv/hr and that many of the observed air masses had significant O_x loss (>10 ppbv O_x loss from the regional background of ~ 35 ppbv), these air masses appear significantly aged, often more than 10 hours.

All of the evidence presented in Figs. 4.2 and 4.3 suggest that N_2O_5 losses are significantly strong to allow NO_x to achieve steady state rapidly (on the same timescale as the lifetime), and that the steady state approximation is valid during our study period.

4.6.2 Loss of N_2O_5 and relative humidity with respect to ice

Time series of N_2O_5 mixing ratios (top trace) covering the duration of the study are presented in Fig. 4.4. The bottom trace is a time series of relative humidity with respect to ice (RH(ice)). Fig. 4.4 shows a clear anti-correlation between N_2O_5 abundance and RH(ice). When RH(ice) is less than 100%, N_2O_5 abundance sometimes reaches its highest levels. Conversely, when RH(ice) is greater than 100%, N_2O_5 abundance is generally suppressed, even though our selection criteria assure that conditions are favorable for formation of N_2O_5 .

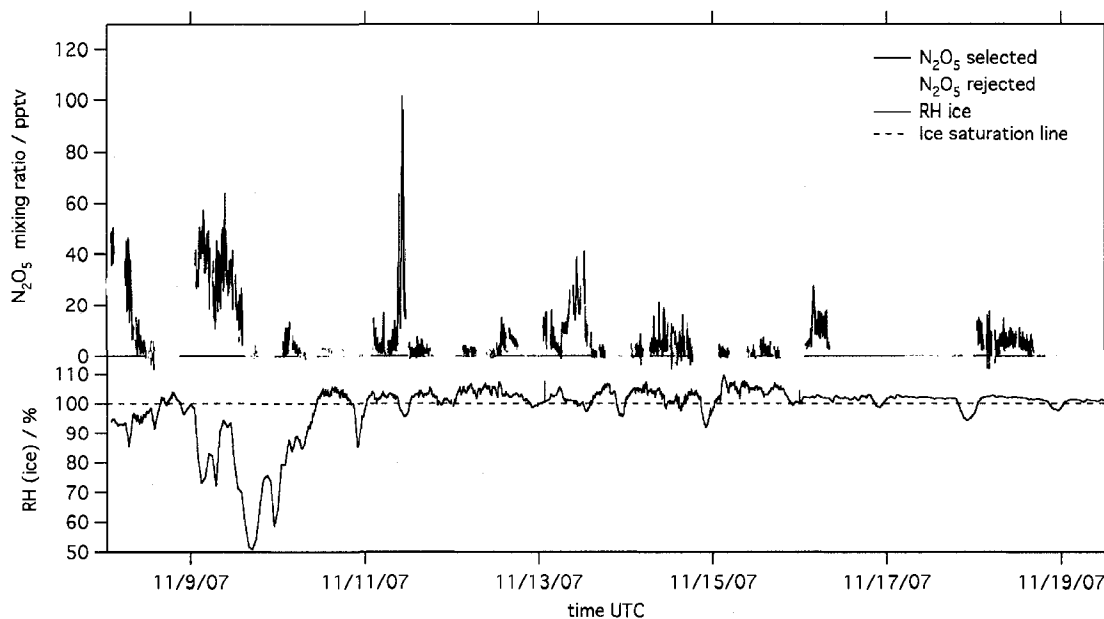


Fig. 4.4 N_2O_5 abundance and relative humidity with respect to ice. The upper panel is a time series of N_2O_5 mixing ratios for the duration of the study. The N_2O_5 data were colored based on the selection criteria described in section 4.5. The lower panel is a time series of relative humidity with respect to ice ($\text{RH}(\text{ice})$). Note the apparent anti-correlation between N_2O_5 abundance and $\text{RH}(\text{ice})$.

For relative humidity with respect to ice less than 100%, ice should evaporate, thermodynamically, and suspended ice particles should not be present. When air cools and $\text{RH}(\text{ice})$ supersaturates, that is, becomes greater than 100%, suspended ice crystals should thermodynamically form. However, nucleation of ice crystals can be a significant barrier to ice crystal formation, allowing $\text{RH}(\text{ice})$ to exceed 100%. Curry et al. (1990) indicate that at cold temperatures, most particles nucleate close to the thermodynamic threshold. Therefore, we use a threshold of 100% to separate conditions that are likely to have suspended ice particles present or absent.

Figure 4.5 shows the dependence of the N_2O_5 steady-state lifetime on the relative humidity with respect to ice. In this and further analysis, we present lifetimes on

logarithmic axes because the distribution of lifetimes is very broad and grouping data in this manner leads to nearly normal (Gaussian) distributions. In this plot, we see that sub-saturated air masses show longer lifetimes than ice-saturated air masses. From the plot, it is clear that there are many points that are ice-saturated but near 100% RH(ice). This behavior is expected because once ice nucleates, water vapor will condense on it, holding the RH(ice) near saturation. On the other hand, sub-saturated air masses will not have ice present, and can take on a wider range of RH(ice) values. We analyze the data in two regions, ice-saturated and sub-saturated, and find nearly a factor of three difference in the mean log-lifetime.

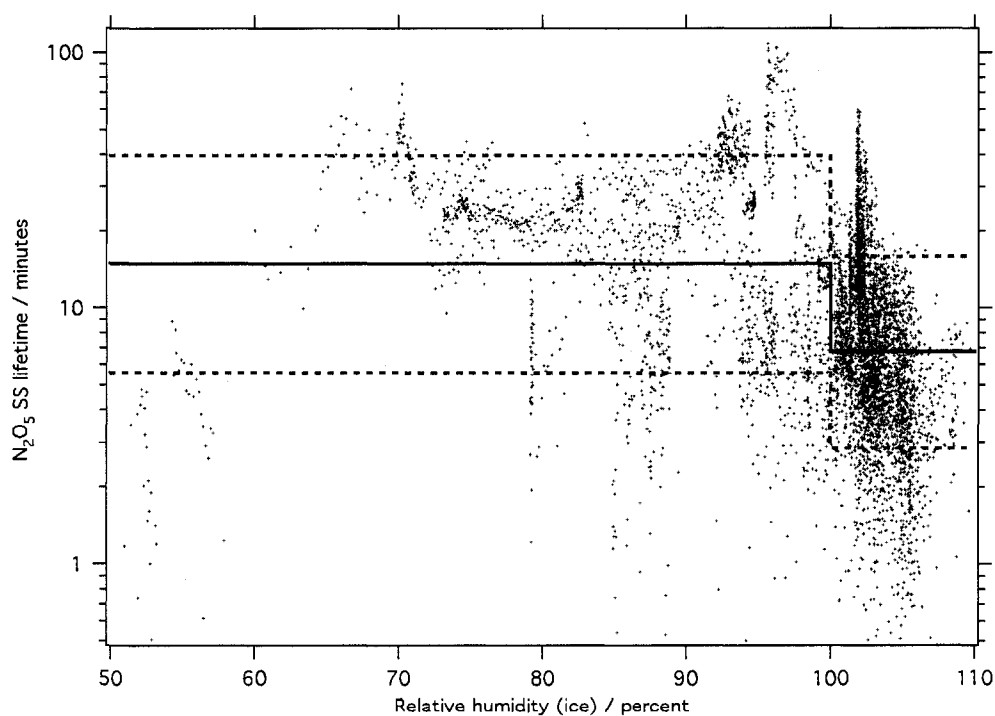


Fig. 4.5 The dependence of $\tau(\text{N}_2\text{O}_5)$ on relative humidity with respect to ice. The red points correspond to individual “selected” N_2O_5 steady-state lifetimes. The black line shows the mean of the log-lifetime distribution within the classes of sub-saturated and ice-saturated airmasses. The dashed line represents the ± 1 -sigma of the distribution of log-lifetimes.

Figure 4.6 shows the same data replotted as normalized histograms of observed N_2O_5 lifetime distributions either at ice-saturated or sub-saturated humidities. The ice-saturated ($\text{RH}(\text{ice}) > 100\%$) population, shown in blue in Fig. 4.6, has a peak value of about 6 minutes. The sub-saturated ($\text{RH}(\text{ice}) < 100\%$) population, shown in red, has a peak value near 20 minutes. Significance testing rejected the null hypothesis that the two populations' means were the same, with a confidence interval at more than 99.9%. Thus, the difference between the ice-saturated and sub-saturated populations is significant and shows that ice formation plays a major role in the loss of N_2O_5 .

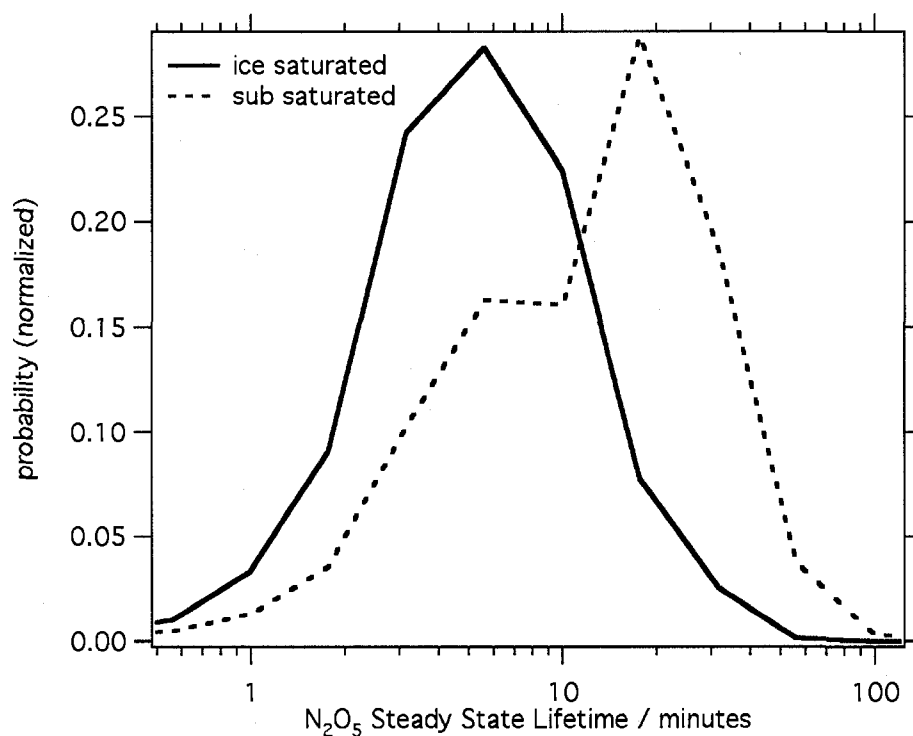


Fig. 4.6 Normalized histograms of $\tau(\text{N}_2\text{O}_5)$. The selected data are split into populations where $\text{RH}(\text{ice})$ was greater than 100% (blue, solid line) and where $\text{RH}(\text{ice})$ was less than 100% (red, dashed line). The peak value for the ice-saturated lifetimes is near 6 minutes and is significantly shorter than the peak value for the sub-saturated lifetimes, which is near 20 minutes.

The observed N_2O_5 lifetimes, in combination with particle surface area can provide an estimate of the N_2O_5 uptake coefficient, $\gamma(\text{N}_2\text{O}_5)$. The uptake coefficient describes the efficiency with which N_2O_5 undergoes heterogeneous hydrolysis per collision with particles. For particles less than $1 \mu\text{m}$, which do not suffer kinetic limitation by mass transport, the reactive uptake coefficient is given by

$$\gamma(\text{N}_2\text{O}_5) = \frac{4}{c_{\text{mean}} A \tau(\text{N}_2\text{O}_5)}. \quad \text{eqn 4.3}$$

Here, c_{mean} is the mean molecular speed of N_2O_5 , and A is the aerosol surface area density.

The ice particle concentrations have been measured to exceed 1000 L^{-1} ($=1 \text{ cm}^{-3}$) in the Arctic (Ohtake et al., 1982; Curry et al., 1990; Girard et al., 2005). Studies of polluted air masses in the Arctic and ice particle size distribution measurements are scarce but have been measured by Benson (1965), who measured ice particles to be between 5 and $10 \mu\text{m}$, and Ohtake and Huffman (1969), who measured ice fog ice particles between 4 and $6 \mu\text{m}$ modal radius. Ice crystal concentration size distributions were used to infer a modal radius of $10 \mu\text{m}$ by Witte (1968) during aircraft measurements in Barrow AK. Gotaas and Benson (1965) cite a radius of $25 \mu\text{m}$ for a radiative cooling study in the Fairbanks area. These values span a fairly wide range but are on the order of a $10\text{-}\mu\text{m}$ modal radius ($20 \mu\text{m}$ diameter) with number densities of a up to ~ 1 particle per cm^3 . Spherical particles with $20 \mu\text{m}$ diameters have a surface area of $\sim 1250 \mu\text{m}^2/\text{particle}$ and non-spherical shapes of the same volume would have higher surface areas per particle, thus suspended ice surface area densities could easily exceed $1000 \mu\text{m}^2/\text{cm}^3$. For our location, the presence of pollution aerosol particles might cause an increased

number of particles to form, which also may be smaller due to spreading the available condensed water across more ice particles. This effect was predicted by Twomey (1974), and has been observed in satellite observations that show pollution suppresses rain and snow (Rosenfeld, 2000; Toon, 2000). Both increased ice particle number and decreased size would increase the surface area significantly and decrease fall rates, resulting in increased atmospheric lifetimes for the particles. Therefore, it is likely that significantly more than $1000 \mu\text{m}^2/\text{cm}^3$ polluted ice surface area density is present in ice-saturated air masses.

Even with some size reduction, ice particles may not be in the submicron size range, and equation 4.3 would then not be directly applicable due to mass transport limitations. However, because the size of the particles is probably near the micron size threshold, we feel it is useful to consider the magnitude of the inferred reactive uptake coefficient (γ) using a lifetime of 6 minutes (the peak of the ice-saturated data) and an A of $\sim 1000 \mu\text{m}^2/\text{cm}^3$. In this limit, one arrives at an estimate of 0.05 for $\gamma(\text{N}_2\text{O}_5)$ on polluted ice particles. While not fully quantitative, this estimate is in reasonable agreement with laboratory and ambient observations of $\gamma(\text{N}_2\text{O}_5)$ with respect to aerosol particles (Hanson and Ravishankara, 1991; Hallquist et al., 2000; Mentel et al., 1999; Leu, 2003; Brown et al., 2006b). It is important to consider the state of the surface of the ice particles. The particles are formed in a polluted air mass that contains at least partially soluble aerosol particles. Measurements of Fairbanks pollution indicate approximately 20% of the aerosol particle mass is sulfate (Fairbanks North Star Borough, 2007). Sulfate that would nucleate or stick to ice particles would be expected to partition

to the surface and locally melt the ice surface. Therefore, ice particles forming in polluted and ice-saturated air masses are unlikely to be pure ice. Instead, the ice particles are likely to have surfaces coated with concentrated aqueous solutions containing sulfate, which have been shown to have relatively high surface reactivity from ambient observations (Brown et al., 2006b). Undoubtedly, further studies characterizing ice particle surface area density are required to quantify the role of ice particles in the removal of N_2O_5 from the atmosphere. However, the significant difference we observe between ice-saturated and sub-saturated N_2O_5 lifetimes clearly indicates that ice has a significant effect on N_2O_5 heterogeneous hydrolysis.

4.6.3 Loss of N_2O_5 with respect to aerosol particles

An alternative hypothesis would be that N_2O_5 losses occur on sub-micron aerosol particles, as has been considered under warm conditions (Brown et al., 2006b). Our observations of aerosol particles did not include a direct measurement of the aerosol surface area density; therefore, other aerosol measurements were used to constrain estimates of the aerosol surface area density and to consider losses of N_2O_5 on aerosol particles. The aerosol particle measurements were carried out in a heated shelter, and thus, any ice particles that may have been sampled would have evaporated, and we would measure only their non-volatile nuclei.

If N_2O_5 losses on aerosol dominate, the expected result would be an anti-correlation between $\tau(\text{N}_2\text{O}_5)$ and aerosol surface area, where lifetimes would be shorter in the presence of higher surface areas. Figure 4.7 shows a timeseries of the N_2O_5 mixing ratio with two directly measured aerosol properties, particle number density and total

submicron sulfate mass concentration. The aerosol data start later than the N_2O_5 measurements and are sometimes missing due to equipment operations or malfunctions. The sulfate data are derived from the modified drum instrument and generally have 2-hour time resolution, leading to a discontinuous appearance. On the 12th of November, the aerosol instrument malfunctioned leading to a single 24-hour sample. While Fig. 4.4 showed a visible anticorrelation between N_2O_5 and ice saturation, these data fail to show clear anticorrelation with aerosol abundance.

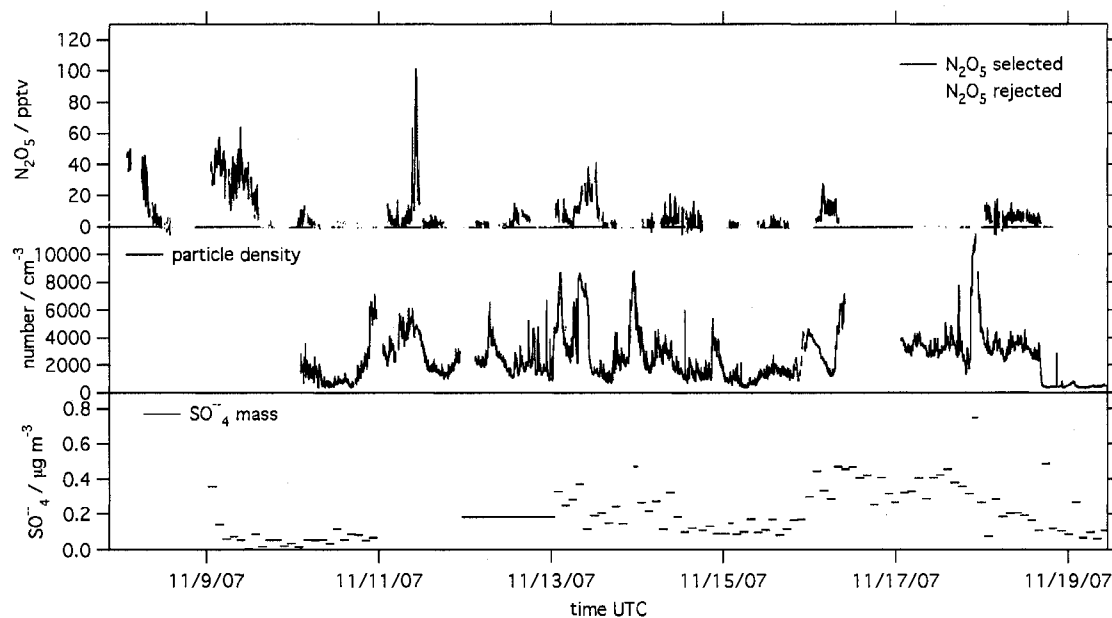


Fig. 4.7 Timeseries of N_2O_5 mixing ratios and aerosol properties.

The size-resolved sulfate mass concentration data were converted to aerosol surface area estimates as described below. Sulfate was only present in the two smaller size bins, which measure particles 0.12 to 0.30 micron diameters (geometric mean diameter 0.19 microns) and 0.30 to 0.84 micron diameters (geometric mean diameter 0.50 microns). The majority, 60%, of the mass was in the smaller size range, with the

remaining 40% in the larger submicron size bin. The raw measurement is the sulfate aerosol concentration ($\mu\text{g}/\text{m}^3$), which is converted to an estimated total particulate concentration in each size bin by dividing by the ratio of sulfate to total particulate mass. Fairbanks pollution data shows that 20% of the aerosol mass is sulfate (Fairbanks North Star Borough, 2007). This total aerosol concentration, for each of the size bins, is then converted to a surface area based upon spherical particles with a density of $1 \text{ g}/\text{cm}^3$ at the mean geometric diameter of the size bin. The surface area is dominated by the smallest bin, which contains 80% of the mass, with a small contribution by the middle bin (20%). The campaign average value aerosol surface area is $24 \mu\text{m}^2/\text{cm}^3$.

Figure 4.8 shows the relationship between the N_2O_5 steady-state lifetime and the aerosol surface area. No obvious anticorrelation is seen in these data, so we attempted to bin the data into four levels of aerosol surface area. The black line shows the median lifetime in each of these four bins, while the dashed lines show ± 1 -sigma of log-lifetime. No significant trending of the lifetime is observed in these data, again indicating that aerosol surface area does not appear to be controlling the N_2O_5 lifetime. It is possible that high variability in the reactive uptake coefficient on aerosol particles would act to mask a direct relationship with aerosol surface area. In fact, Brown et al. (2006b) observed a large variability in $\gamma(\text{N}_2\text{O}_5)$ when changing between Ohio river valley acidic sulfate aerosol and maritime aerosols. However, in our study, there is one dominant source of aerosol, Fairbanks pollution, which would be expected to have more constant aerosol properties than the aircraft-sampled data reported by Brown et al. (2006b).

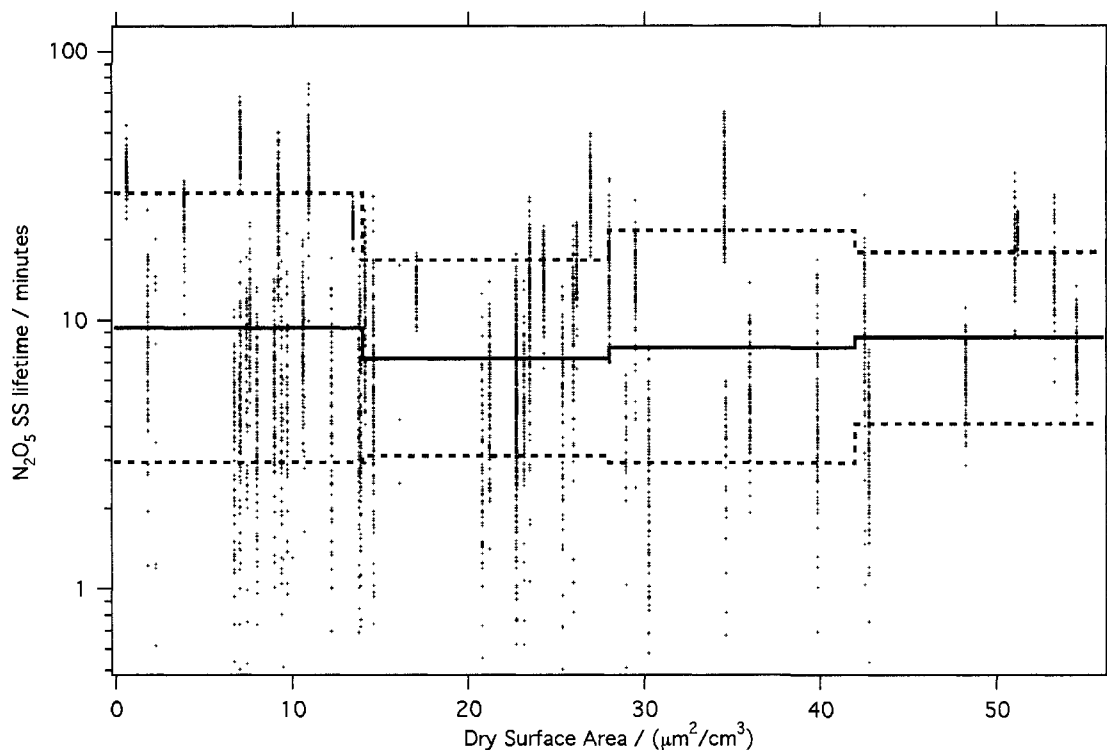


Fig. 4.8 The relationship between aerosol surface area N_2O_5 and lifetime. The red points correspond to individual “selected” N_2O_5 steady-state lifetimes as a function of aerosol surface area derived from the modified drum data. The black line shows the median lifetime within each of four bins covering the observed range of aerosol surface areas, and the dashed lines represent ± 1 -sigma of the distribution of log-lifetimes. The data fail to show an anticorrelation between aerosol surface area and N_2O_5 lifetime. See text for details.

To estimate the N_2O_5 reactive uptake coefficients on aerosol particles, we again refer to equation 4.3. Estimates for aerosol surface area density, A , were arrived at using two independent methods. First, we used the average surface area, $24 \mu\text{m}^2/\text{cm}^3$, calculated from the drum impactor data. Alternatively, as a check of these calculations, we converted the condensation particle counter number density data to an inferred surface area using published tri-modal log-normal particle size distributions. Parameters for this conversion were taken from Seinfeld and Pandis (1998) for “urban” and “rural” pollution. The urban and rural distributions give differing estimates of surface area of 31 and 54

$\mu\text{m}^2/\text{cm}^3$, respectively, and while the estimation is clearly crude, it indicates that dry aerosol surface areas are relatively small.

While these various estimates of aerosol surface area are only semi-quantitative, because of the necessity to make assumptions regarding the aerosol properties, each estimate gives surface area densities that are maximally around $50 \mu\text{m}^2/\text{cm}^3$. The resultant estimates for $\gamma(\text{N}_2\text{O}_5)$, assuming all losses occur on aerosol particles, would be approximately equal to unity, more than an order of magnitude higher than other observed values (Hanson and Ravishankara, 1991, Halliquist et al., 2000, Mental et al., 2006, Leu, 2003, Brown et al., 2006b). Therefore, the large losses of N_2O_5 observed in our study are not readily explained by particulate pollution in the cold Fairbanks pollution plume. Instead, the lack of anti-correlation of N_2O_5 lifetime with particle counts and sulfate mass, in addition to estimates of surface area indicating that aerosol particles are insufficient to explain losses of N_2O_5 using laboratory values of $\gamma(\text{N}_2\text{O}_5)$, supports the idea that other surfaces are important for N_2O_5 losses in cold high-latitude plumes. Our finding of the important role of atmospheric ice surfaces (Section 4.6.2) is clearly one such surface. Furthermore, it is likely that deposition to the seasonal snowpack is a second important loss mechanism for N_2O_5 , particularly when ice particles are not present in the boundary layer.

4.7 Conclusions and atmospheric implications

We have presented the first direct observations implicating ice particles as having the surfaces that catalyze heterogeneous hydrolysis of N_2O_5 in the cold, nighttime boundary layer at high latitudes. The observations show a strong anti-correlation for both

N_2O_5 abundance and $\tau(\text{N}_2\text{O}_5)$ when compared to relative humidity with respect to ice. When the $\text{RH}(\text{ice})$ is greater than 100% and ice is likely present, $\tau(\text{N}_2\text{O}_5)$ is short and N_2O_5 levels are suppressed. On the other hand, when $\text{RH}(\text{ice})$ is less than 100%, ice is probably absent and $\tau(\text{N}_2\text{O}_5)$ is long and N_2O_5 levels are elevated. The difference between the peaks of these two lifetime distributions is more than a factor of three.

The formation of suspended ice particles is a common occurrence in the cold high-latitude boundary layer. Daytime warming of snowpack produces water vapor from snowpack through sublimation of ice. Thus, seasonal snowpack holds the air in the boundary layer nearly saturated with respect to ice for much of the cold season (Andreas et al., 2002). The result of nighttime cooling is the formation of small ice particles that are slow to sediment from the boundary layer. Pollution may also produce increased numbers of ice nuclei that could increase the number and decrease the size of ice particles as well as modify the chemical nature of their surface by presenting soluble impurities to the atmosphere. Simple estimates of ice surface area combined with laboratory values of $\gamma(\text{N}_2\text{O}_5)$ found in the current literature (Hanson and Ravishankara, 1991, Halliquist et al., 2000, Mental et al., 1999, Leu, 2003) are in reasonable agreement with observed N_2O_5 loss rates. Suspended ice particles are ubiquitous in the atmosphere at high latitudes and are responsible for halos, ice pillars, and other well-known optical phenomena (Tape, 2006). Our findings indicate that cold plumes are “self-scrubbing” of nitrogen oxides through an N_2O_5 heterogeneous hydrolysis pathway that uses ice particles as the reactive surface. Dentener and Crutzen (1993) found that in order to reproduce NO_x and nitrate ion deposition patterns observed at high latitude, their model required a $\gamma(\text{N}_2\text{O}_5) = 0.1$ on

aerosol surfaces. That value of $\gamma(\text{N}_2\text{O}_5)$ is higher than what was found in the available literature and suggests other potential N_2O_5 loss mechanisms may be acting. Therefore, our finding that ice particles catalyze N_2O_5 loss helps to resolve this modeling study with recent laboratory and mid-latitude field measurements. Further characterization of polluted ice as a sink for N_2O_5 is critical to understanding NO_x budgets at high latitudes. Careful considerations for suspended ice must be made when modeling seasonal affects on NO_x and ozone pollution in other cold regions. Lastly, characterizing N_2O_5 loss on polluted ice surfaces is important for determining the spatial and temporal footprint of acid deposition and nitrogen fertilization in such sensitive regions as the arctic. As NO_x inputs to the arctic grow from increasing fossil fuel consumption or increasing ship traffic in the Northwest Passage, the ecological impacts of NO_x oxidation and the subsequent nitrogen deposition becomes more important to understand.

4.8 References

- Allan B.J., Carslaw N., Coe H, Burgess R.A., and Plane J.M.C., 1999. Observation of the nitrate radical in the marine boundary layer. *J Atmos Chem*, 33, 129-154.
- Andersen H.V., Hovmand M.F., 1995. Ammonia and nitric acid dry deposition and throughfall. *Water air and soil pollution*, 85 (4): 2211-2216.
- Andreas, E. L.; Guest, P. S.; Persson, P. O. G.; Fairall, C. W.; Horts, T. W.; Moritz, R. E.; Semmer, S. R., 2002. Near-surface water vapor over polar sea ice is always near ice saturation. *J. Geophys. Res*, 107 (C10), 15.
- Apodaca, R.L., W. R. Simpson, S. M. Ball, T. Brauers¹, S. S. Brown, R. C. Cohen, J. Crowley, H.P. Dorn, W. P. Dube, J. Fry, H. Fuchs, R. Haseler, U. Heitmann, S. Kato, Y. Kajii, A. Kiendler-Scharr, I. Labazan, J. Matsumoto, S. Nishida, R. Tillmann, F. Rohrer, E. Schlosser, G. Schuster, A. Shillings, R. Tillmann, A. Wahner¹, R. Wegener, and P. J. Wooldridge, Intercomparison of N₂O₅ sensors using SAPHIR reaction chamber. In preparation (2008).
- Ayers, J. D.; Simpson, W. R., 2006. Measurements of N₂O₅ near Fairbanks, Alaska. *Journal of Geophysical Research-Atmospheres*, 111, (D14).
- Ayers, J. D.; Apodaca, R. L.; Simpson, W. R.; Baer, D. S., 2005. Off-axis cavity ring-down spectroscopy: application to atmospheric nitrate radical detection. *Applied Optics*, 44, (33), 7239-7242.
- Benson, C. S., 1965. Ice Fog: Low temperature air pollution, Tech. rep., Geophys. Inst. Rept. UAG R-173, Univ. of Alaska.
- Bergholm J, Berggren D, Alavi G., 2003. Soil acidification induced by ammonium sulphate addition in a Norway spruce forest in Southwest Sweden. *Water air and soil pollution*, 148 (1-4): 87-109.
- Brown, S. S., Stark, H., Ciciora, S. J., and Ravishankara, A. R., 2001. In-situ measurement of atmospheric NO₃ and N₂O₅ via cavity ring-down spectroscopy, *Geophys. Res. Lett.*, 28, 3227.
- Brown, S. S., Stark, H., Ciciora, S. J., McLaughlin, R. J., and Ravishankara, A. R., 2002. Simultaneous in-situ detection of atmospheric NO₃ and N₂O₅ via cavity ring-down spectroscopy, *Rev. Sci. Inst.*, 73, 3291-3301.
- Brown, S. S.; Stark, H.; Ravishankara, A. R., 2003. Applicability of the steady state approximation to the interpretation of atmospheric observations of NO₃ and N₂O₅. *Journal of Geophysical Research-Atmospheres*, 108, (D17).

Brown, S. S.; J. A. Neuman, T. B. Ryerson, M. Trainer, W. P. Dubé, J. S. Holloway, C. Warneke, J. A. de Gouw, S. G. Donnelly, E. Atlas, B. Matthew, A. M. Middlebrook, R. Peltier, R. J. Weber, A. Stohl, J. F. Meagher, F. C. Fehsenfeld and A. R. Ravishankara, 2006a. Nocturnal odd-oxygen budget and its implications for ozone loss in the lower troposphere, *Geophys. Res. Lett.*, 33, L08801.

Brown, S. S.; Ryerson, T. B.; Wollny, A. G.; Brock, C. A.; Peltier, R.; Sullivan, A. P.; Weber, R. J.; Dube, W. P.; Trainer, M.; Meagher, J. F.; Fehsenfeld, F. C.; Ravishankara, A. R., 2006b. Variability in nocturnal nitrogen oxide processing and its role in regional air quality. *Science*, 311, (5757), 67-70.

Cahill, C. F., 2003. Asian Aerosol Transport to Alaska during ACE-Asia, *J. Geophys. Res.*, 108, 8664.

Chapin, F.S. 2007. Bonanza Creek Experimental Forest: Hourly Relative Humidity (mean, min, max) at 50 cm and 150 cm from 1988 to Present. Fairbanks, AK: Bonanza Creek LTER Database:BNZD:241.
http://www.lter.uaf.edu/data_detail.cfm?datafile_pkey=241; NSF awards DEB-0620579, DEB-0423442, DEB-0080609, DEB-9810217, DEB- 9211769, DEB-8702629 and USDA Forest Service, Pacific Northwest Research Station RJVA-PNW-01-JV-11261952-231.

Curry, J.A., F.G. Meyer, L.F. Radke, C.A. Brock, and E.E. Ebert, 1990. The occurrence and characteristics of lower tropospheric ice crystals in the Arctic. *Int. J. Climatol.*, 10, 749-764.

Dentener F.J., Crutzen P.J., 1993. Reactions of N_2O_5 on tropospheric aerosols: Impact on the global distribution of NO_x , O_3 , and OH. *J Geophys Res*, 98 (D4): 7149-7163.

Fairbanks North Star Borough: Review of Source Contributions to Ambient PM 2.5 Concentrations, Tech. rep., Department of Environmental Conservation, Fairbanks, Alaska, 2007.

Fenn, M. E.; Baron, J. S.; Allen, E. B.; Rueth, H. M.; Nydick, K. R.; Geiser, L.; Bowman, W. D.; Sickman, J. O.; Meixner, T.; Johnson, D. W.; Neitlich, P., 2003. Ecological effects of nitrogen deposition in the western United States. *Bioscience*, 53, (4), 404-420.

Finlayson-Pitts, B. J., , and J. N. Pitts Jr. (2000), *Chemistry of the Upper and Lower Atmosphere*, Elsevier, New York.

Geyer, A., and J. Stutz, 2004. Vertical profiles of NO_3 , N_2O_5 , O_3 , and NO_x in the nocturnal boundary layer: 2. Model studies on the altitude dependence of composition and chemistry, *J. Geophys. Res.*, 109, D12307,

Girard, E., Blanchet, J.-P., and Dubois, Y., 2005. Effects of arctic sulphuric acid aerosols on wintertime low-level atmospheric ice crystals, Alert Nunavut., *Atmos. Res.*, 73, 131–148.

Gotaas, Y. and Benson, C. S., 1965. The effect of Suspended Ice Crystals on Radiative Cooling, *J. Appl. Meteorol.*, 4, 446–453.

Hallquist, M., Stewart, D. J., Baker, J., and Cox, R. A., 2000. Hydrolysis of N_2O_5 on submicron sulfuric acid aerosols, *J. Phys. Chem. A*, 104, 3984–3990.

Hanson, D. R. and Ravishankara, A. R., 1991. The reaction probabilities of ClONO_2 and N_2O_5 on polar stratospheric cloud materials, *J. Geophys. Res.*, 96, 5081–5090.

Heintz F., Platt U., Flentje H., and Dubois R., 1996. Long-term observation of nitrate radicals at the Tor Station, Kap Arkon (Rugen), *J Geophys Res*, 101 (D17): 22891-22910.

King, M. D., Dick, E. M., and Simpson, W. R., 2000. A new method for the atmospheric detection of the nitrate radical (NO_3), *Atmos. Env.*, 34, 685–688.

Leu, M. T., 2003. Laboratory studies of interaction between trace gases and sulphuric acid or sulphate aerosols using flow-tube reactors. *International Reviews in Physical Chemistry*, 22, (2), 341-376.

Mentel, T. F., M. Sohn, and A. Wahner, 1999. Nitrate effect in the heterogeneous hydrolysis of dinitrogen pentoxide on aqueous aerosols, *Phys. Chem. Chem. Phys.*, 1, 5451–5457.

Nakayama, T., Tomoyuki Ide, Fumikazu Taketani, Megumi Kawai, Kenshi Takahashi, Yutaka Matsumi, 2008. Nighttime measurements of ambient N_2O_5 , NO_2 , NO and O_3 in a sub-urban area, Toyokawa, Japan. *Atmospheric Environment*, Volume 42, Number 9.

Ohtake, T. and Huffman, P., 1969. Visual Range in Ice Fog, *J. Appl. Meteor.*, 8, 499–501.

Ohtake, T., Jayaweera, K., and Sakurai, K., 1982. Observation of Ice Crystal Formation in Lower Arctic Atmosphere, *J. Atmos. Sci*, 39, 2898–2904.

- Perry, K. D., Cahill, T. A., Schnell, R. C., and Harris, J. M., 1999. Long-range transport of anthropogenic aerosols to the National Oceanic and Atmospheric Administration baseline station at Mauna Loa Observatory, Hawaii, *J. Geophys. Res.*, 104, 18 521 – 18 533.
- Platt, U., D. Perner, G. W. Harris, A. M. Winer, and J. N. Pitts., 1980, Detection of NO_3 in the polluted troposphere by differential optical absorption, *Geophys. Res. Lett.*, 7, 89–92.
- Rosenfeld, D., 2000. Suppression of rain and snow by urban and industrial air pollution, *Science*, 287, 1793 – 1796.
- Sander, S. P., Friedl, R. R., Golden, D. M., Kurylo, M. J., Moortgat, G. K., Keller-Rudek, H., Wine, P. H., Ravishankara, A. R., Kolb, C. E., Molina, M. J., Finlayson-Pitts, B. J., Huie, R. E., and Orkin, V. L., 2006. Chemical kinetics and photochemical data for use in atmospheric studies, JPL Publication 06-2.
- Seinfeld, J. H., and S. N. Pandis, (1998). *Atmospheric Chemistry and Physics*, John Wiley, Hoboken, N. J..
- Simpson, W. R., 2003. Continuous wave cavity ring-down spectroscopy applied to in situ detection of dinitrogen pentoxide (N_2O_5), *Rev. Sci. Instrum.*, 74, 3442– 3452.
- Stutz, J. B., Ackermann, R., Geyer, A., White, A., and Williams, E., 2004. Vertical profiles of NO_3 , N_2O_5 , O_3 , and NO_x in the nocturnal boundary layer: 1. Observations during the Texas Air Quality Study 2000, *J. Geophys. Res.*, 109, D12 306.
- Tape, W., 2006. *Atmospheric Halos and the Search for Angle X*, American Geophysical Union, Washington, D.C..
- Toon, O. B., 2000. How pollution suppresses rain, *Science*, 5459, 1763 – 1765.
- Twomey, S., 1974. Pollution and the planetary albedo, *Atmos. Environ.*, 8, 1251 – 1256.
- Witte, H. J., 1968. Airborne observations of cloud particles and infrared flux density (8–14 μm) in the Arctic, Master's thesis, University of Washington.
- Wood, E. C., P. J. Wooldridge, J. H. Freese, T. Albrecht, and R. C. Cohen., 2003. Prototype for in situ detection of atmospheric NO_3 and N_2O_5 via laser-induced fluorescence, *Environ. Sci. Technol.*, 37, 5732–5738.

Chapter 5:

Vertical profiles of N_2O_5 in the Fairbanks pollution plume

5.1 Introduction

Nitrogen oxides play a central role in essentially all aspects of atmospheric chemistry, particularly at night when the oxidizing capacity of the nocturnal boundary layer is controlled by reactions of O_3 , NO , NO_2 , NO_3 and N_2O_5 (Finlayson-Pitts and Pitts, 2000). Throughout this thesis we have discussed the important roles played by N_2O_5 in removing nitrogen oxides from the unique, high-latitude nighttime atmosphere. The nighttime atmosphere possesses several characteristics that can affect the chemistry of N_2O_5 near the Earth's surface. First, the nocturnal boundary layer is often quite shallow and can extend to less than 100 m from the surface under cold conditions (Finlayson-Pitts and Pitts, 2000), such as those seen at high latitudes. Second, vertical transport is inhibited at night due to diminished turbulent mixing (Stull, 1988; Wayne, 2000). The result of the shallow boundary layer and diminished vertical mixing is that nitrogen oxides emitted near the ground tend to be more concentrated and stratified than daytime emissions (Brown et al., 2007a).

Modeling studies, as well as a limited number of field studies, have demonstrated that strong vertical gradients in NO_3 and N_2O_5 can exist in the nocturnal boundary layer (Galimardini et al., 1997; Fish et al., 1999; Geyer et al., 2004; Stutz et al., 2004; Brown et al., 2007a; b). The nighttime vertical gradients in NO_3 and N_2O_5 can show large variability due to stratification of their sources and sinks. Figure 5.1, adapted from

Brown et al. (2007a) shows example vertical profiles of NO_3 , N_2O_5 , and O_3 measured near Boulder, Colorado.

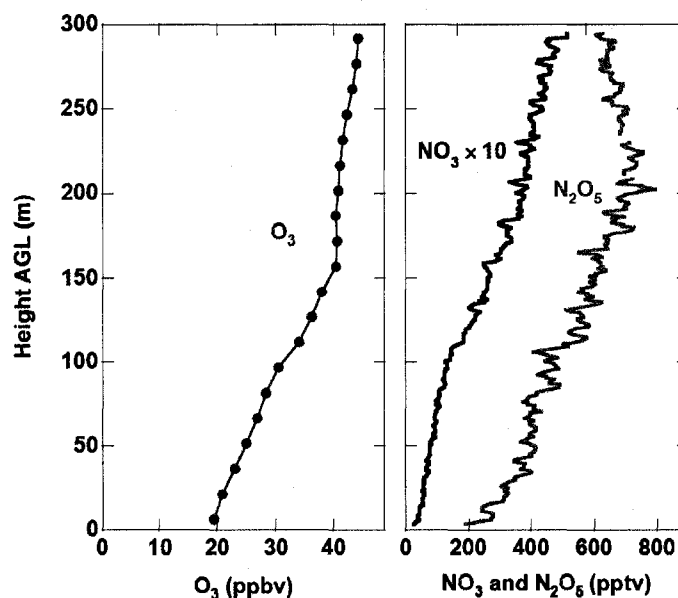


Fig. 5.1 Examples of vertical gradients in O_3 , NO_3 , and N_2O_5 adapted from Brown et al. (2007a). Height AGL refers to the height of the measurement above ground level (AGL). This figure demonstrates that mixing ratios of O_3 , NO_3 , and N_2O_5 typically increase with elevation, albeit nonlinearly, in the nocturnal boundary layer.

Figure 5.1 demonstrates that N_2O_5 mixing ratios tend to increase with elevation. Below 10 m elevation, N_2O_5 mixing ratios have been reported to range from near zero to several hundred parts per trillion by volume (pptv). Aloft, near the top of the nocturnal boundary layer, N_2O_5 mixing ratios have been reported as high as a few parts per billion by volume, denoted ppbv (Geyer et al., 2004; Stutz et al., 2004; Brown et al., 2007a, b). Similarly, gradients in NO_3 have been observed in the nocturnal boundary layer and typically increase with elevation (Stutz et al., 2004; Brown et al., 2007a, b). NO_3 concentrations near the ground are often near zero (often due to reaction with NO or volatile organic compounds, denoted VOC), particularly in the lowest 10 m of the

boundary layer where NO and VOC sources can be quite strong (Stutz et al., 2004; Brown et al., 2007a, b)

As a part of our investigation into the processes controlling nocturnal NO_x oxidation at high latitudes, we conducted the Spring 2007 field campaign at the University of Alaska Fairbanks (UAF) Experimental Farm. The over-arching goal of this study was to characterize the nocturnal NO_x oxidation process in the freshly-emitted Fairbanks pollution plume. Furthermore, as part of the characterization process, we probed the lowest 4 meters of the nocturnal boundary layer for gradients in N₂O₅. Here, we present the results from vertical profiling measurements made from 21 to 30 March 2007.

5.2 Experimental

Vertical profiles of N₂O₅ were measured using the oa-CRDS instrument characterized in previous chapters of this thesis. The oa-CRDS instrument was housed in a small warming shed located at the UAF Experimental Farm. The UAF Experimental Farm (64.85°N, 147.86°W; 140 m elev.) is located on the outer edge of the city of Fairbanks (top panel, fig. 5.2) and consists of a large, ~100-acre agricultural field, cleared of vegetation and covered by a seasonal snow pack throughout the duration of the study. In order to obtain ambient air samples that were not perturbed by the warming shed, a high volume pump was used to deliver ambient air along a 10 m-long bypass manifold and into the building for sampling by the N₂O₅ instrument. A schematic representation of the sampling system is shown in the bottom panel of fig. 5.2. The bypass manifold was constructed of 1/2" O.D., 3/8" I.D. Teflon tubing and was attached to the high volume

pump, drawing air at about 115 slpm. The inlet of the manifold was attached to a pulley system, allowing for sampling at adjustable elevations above the snow pack. The oa-CRDS N_2O_5 instrument sampled from the manifold using a $\frac{1}{2}$ " Teflon T-union at a rate of 8 slpm, and was operated as described in chapter 2.

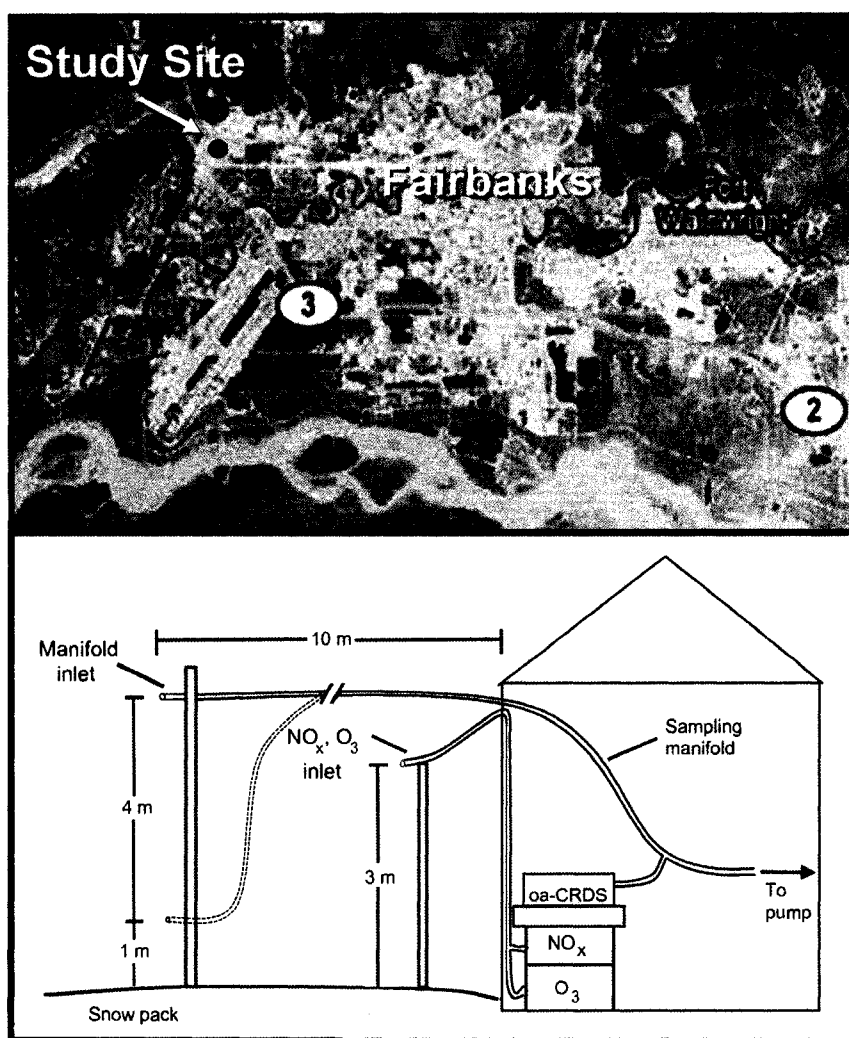


Fig. 5.2 Study site and experimental set up. Top panel: A satellite image showing the study site location and its relationship to Fairbanks and the surrounding area. Bottom panel: Schematic representation of the sampling manifold for the oa-CRDS N_2O_5 instrument. The N_2O_5 manifold inlet was mounted to a 4.5 m pole with a pulley system. N_2O_5 profiling measurements were conducted by using the pulley system to place the inlet at 4 and 1 m above the snow pack. The NO_x - O_3 sampling manifold is also shown in the bottom panel. The NO_x - O_3 inlet was stationary, at 3 m above the snow pack.

Each night, after sunset and the subsequent formation of N_2O_5 , we measured N_2O_5 mixing ratios at 4 and 1 meters above the snow pack. Using the single manifold/single N_2O_5 instrument set up, the measurements were made sequentially by alternating the height of the manifold inlet between 4 and 1 m. First, the manifold inlet was positioned at 4 m, where N_2O_5 was measured for 120 s. Next, during an NO-titration period (described in chapter 2), the manifold inlet was lowered to 1 m and allowed to measure for 120 s. Lastly, during the next NO-titration, the manifold inlet was returned to the 4 m position. This vertical profiling procedure was repeated for 1-2 hours after the first appearance of N_2O_5 . In addition to the N_2O_5 measurements, air temperatures were continuously recorded at 4 and 1 m, with temperature sensors (Analog Devices Inc., AD22100) fixed directly adjacent to the manifold inlet opening.

Measurements of NO and NO_2 were collected using a Thermo Environmental 42c NO_x analyzer, and O_3 measurements were collected using a Dasibi 1008 RS instrument. The NO_x and O_3 analyzers were located in the warming shed and sampled ambient air through a common 1/4" O.D., 1/8" I.D. Teflon inlet. This common inlet was approximately 8 m long and was maintained 3 m above the snow pack.

5.3 Results

Figure 5.3 shows time series measurements of N_2O_5 vertical profiles from the 10 day campaign. March 23rd data are not available as measurements were temporarily suspended due to inclement weather. The N_2O_5 data in fig. 5.3 are reported at about 3 Hz and are colored red for measurements taken at 4 m and blue (with shaded background) for measurements taken at 1 m. Furthermore, the N_2O_5 data were corrected for sampling

inlet loss as described in chapter 2. Concurrent measurements of O_3 (purple), NO_2 (brown), and NO (green) were averaged to 1 minute and are shown in the upper panel of the daily time series in fig 5.3. Typical N_2O_5 levels ranged from below instrument detection limits to more than 100 pptv throughout the profiling studies. Typical O_3 and NO_2 levels ranged from a few ppbv to near 40 ppbv, with average levels of about 25 and 5 ppbv, respectively.

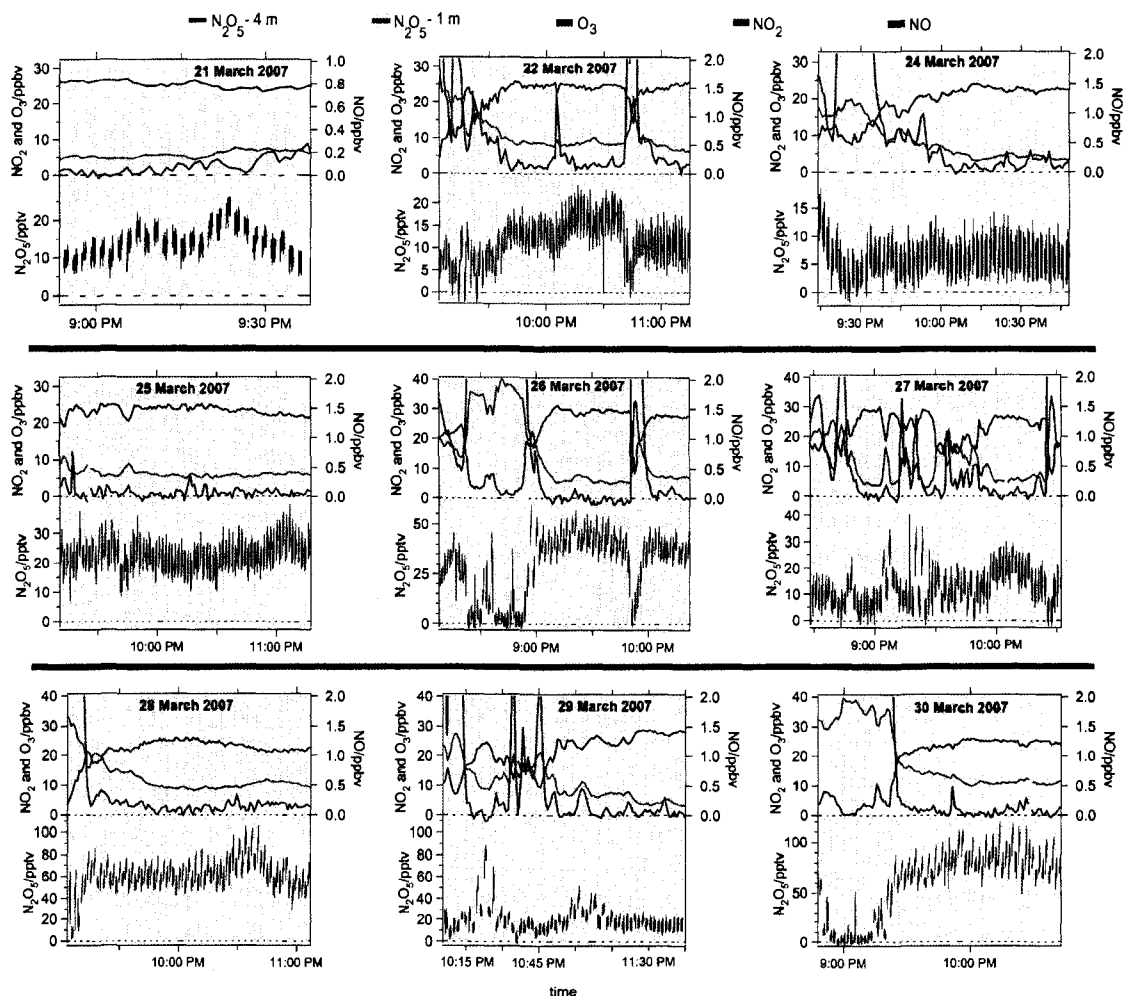


Fig. 5.3 N_2O_5 vertical profiles. The time series showing N_2O_5 measurements at 4 m (red) and 1 m (blue), as well as O_3 (purple), NO_2 (brown), and NO (green) observations. Note the presence of vertical gradients in N_2O_5 on most nights.

Examination of fig. 5.3 reveals clear differences between N_2O_5 abundance measured at 1 and 4 m on most days. Ozone titration events, by freshly emitted NO, is evident on most days as NO levels ranged from below instrument detection limits to more than 100 ppbv. The large, transient, NO events are the result of local sources (e.g. trains and snow machines) passing by the study site on nearby train tracks or snow machine trails. When elevated NO is present, large perturbations in N_2O_5 are observed and the N_2O_5 mixing ratio often drops to near zero. This observation is expected and is the result of the reactive sink of NO_3 , reacting with NO, being faster than the formation of N_2O_5 . To prevent the NO-induced N_2O_5 perturbations from biasing potential gradient observations, all subsequent N_2O_5 analysis is conducted at NO levels ≤ 0.2 ppbv.

5.4 Ratios of N_2O_5 levels at 1 m and 4 m

The ratio of N_2O_5 at 1 m versus 4 m, or simply 1 m:4 m, provides a measure of the different N_2O_5 abundances observed between the two elevations. Table 5.1 summarizes the average ratio between the two elevations for each profiling study and is organized in order of increasing ratio. The averaged ratios listed in table 5.1 show that, with the possible exception of March 22nd, the 4 m N_2O_5 measurements are 5 to 30% higher than the 1 m measurements.

Table 5.1 A summary of the average ratio of N_2O_5 (1 m:4 m) for the nightly profiling studies. Also shown are the averaged observed N_2O_5 abundance, the average ambient temperature, and the average temperature difference between 1 m and 4 m observations.

March 2007	Average ratio (1m:4m)	Average N_2O_5 (pptv)	Average temperature ($^{\circ}\text{C}$)	Average temperature difference ($^{\circ}\text{C}$) (1 m - 4 m)
29	0.70	30	-13.4	-3.0
27	0.80	20	-17.6	-2.1
30	0.83	90	-9.8	-1.0
28	0.84	70	-15.8	-0.2
26	0.85	45	-15.1	-0.5
21	0.86	20	-10.6	0
25	0.90	20	-20.6	0
24	0.95	8	-21.4	-0.1
22	0.99	20	-18.7	0

Also listed in table 5.1 are the average N_2O_5 mixing ratios (8 to 90 pptv), the average air temperatures (-10 to -20°C), and the average difference between the 1 m temperatures and 4 m temperatures observed during each profiling study. The average temperature difference column indicates that the 1 m temperatures were lower than the 4 m temperatures on most nights. Figure 5.4 shows an example of the difference in temperature observed between the 1 m (solid black trace) and 4 m (dashed black trace) elevations during a profiling study conducted on 30 March 2007.

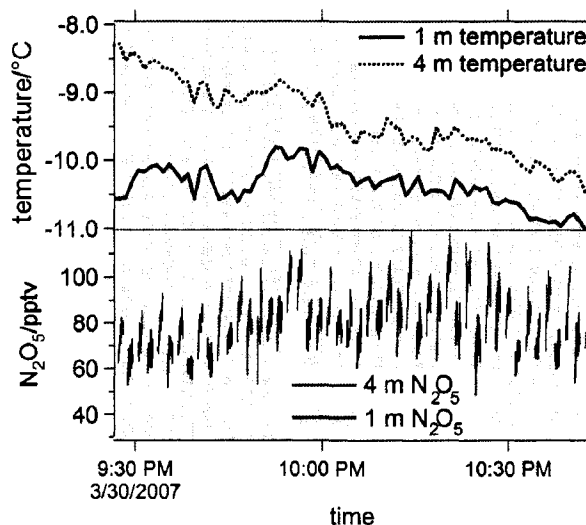


Fig. 5.4 An example of the temperature difference between the 1 m and 4 m elevations taken from the profiling study conducted on 30 March 2007. The average temperature difference on this day was -1°C . An example N_2O_5 vertical profile is included in the bottom panel.

The data presented in this section, particularly those shown in Table 5.1, reveal several important observations about N_2O_5 vertical profiles. First, the ratio of N_2O_5 at the two elevations clearly decreases as the magnitude of the average temperature difference increases. Figure 5.5 illustrates the relationship between the average ratio and the average temperature difference. The best fit to the data suggests that the ratio of N_2O_5 at 1 m versus 4 m decreases by 7% per $^{\circ}\text{C}$ of temperature difference. The presence of less N_2O_5 at 1 meter than at 4 m, coupled with the temperature profiles, suggests increased stratification and decreased mixing of the lowest 4 m of the boundary layer.

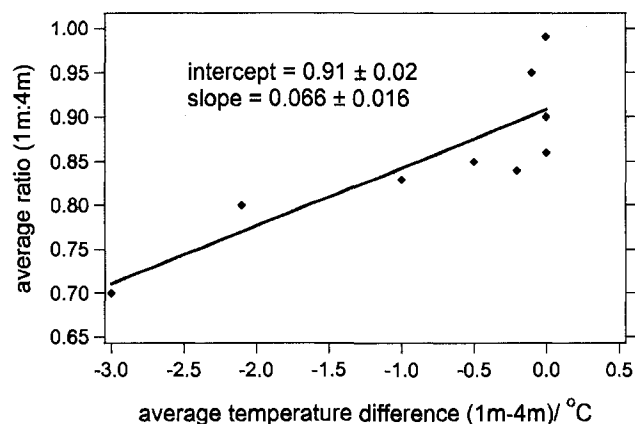


Fig. 5.5 The relationship between the average ratio of N_2O_5 and the average temperature difference measured at the two elevations. The red diamonds are the data and the black line is the linear regression.

Second, the magnitude of the 1 m:4 m ratio appears to have a small dependence on the average observed temperature as illustrated in fig. 5.6. Colder temperatures appear to lead to higher 1 m:4 m ratios than those observed at warmer times. The linear regression illustrated in fig. 5.6 suggests that the ratio of N_2O_5 between the two elevations decreases by approximately 1% per °C as the ambient temperature cools.

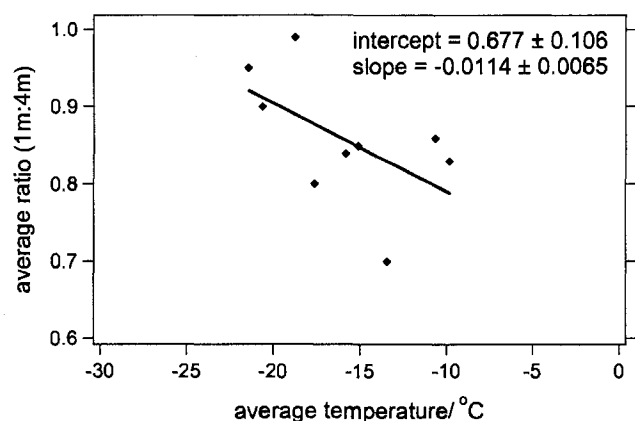


Fig. 5.6 The relationship between the average ratio of N_2O_5 and the average temperature measured during the individual profiling experiments. The red diamonds are the data and the black line is the linear regression.

Finally, the ratio between the two elevations shows no clear dependence on N_2O_5 abundance. Figure 5.7 is a plot of the relationship between the average ratio and the average N_2O_5 abundance measured during each profiling experiment. The best fit of the data reveals a slope of approximately zero and examination of the data (red diamonds) reveals that similar ratios are observed throughout the spectrum of observed N_2O_5 abundance.

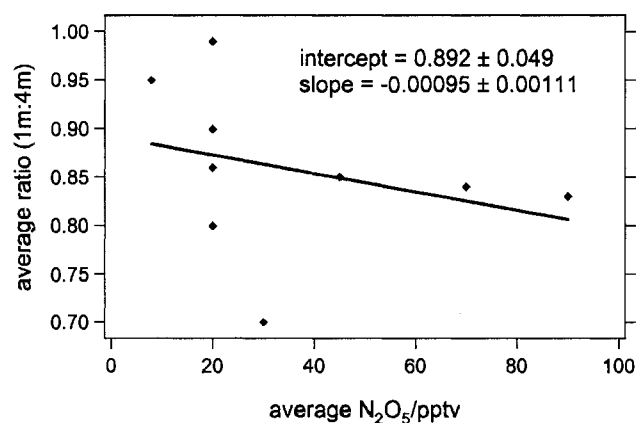


Fig. 5.7 The relationship between the average ratio of N_2O_5 and the overall average N_2O_5 abundance measured during the individual profiling studies. The red diamonds are the data and the black line is the linear regression.

5.5 Conclusions

We have presented vertical profiles of N_2O_5 measured in the Fairbanks pollution plume. Our observations show that N_2O_5 abundance is often less at 1 m above the seasonal snow pack than at 4 m. The data suggests that the ratio of N_2O_5 at 1 m versus 4 m has a small temperature dependence in that the ratios appear to decrease as the overall average temperature warms. Furthermore, our observations show that the ratio of N_2O_5 between 1 m and 4 m decreases as the difference in temperature (between 1 m and 4 m) increases. The observed N_2O_5 and temperature profiles are consistent with stratification

of the lowest 4 meters of the boundary layer, and suggest the presence of vertical gradients in the chemical composition of this region.

The presence of gradients between 1 m and 4 m N_2O_5 levels suggest that different chemical processes are affecting the two elevations' data differently. For example, the observed vertical gradients in N_2O_5 could be produced by rapid surface loss of N_2O_5 . In chapter 4 we presented data implicating ice as having the surfaces that catalyze heterogeneous hydrolysis of N_2O_5 in the cold, high latitude, nighttime atmosphere. The profiling studies discussed in the current chapter were conducted above a well-established snow pack and it is clearly conceivable that the lower N_2O_5 levels at 1 m are the result of chemical loss to ice surfaces in the snow. Comparing the N_2O_5 lifetimes would be an important way to look for deposition to surface. However, it should be noted that the lifetime estimates are essentially equivalent to N_2O_5 abundance because they can only be made in these data using NO_2 and O_3 measurements from a fixed 3 m elevation. Nevertheless, the qualitative examination of the data suggests gradients in the N_2O_5 lifetime are present and that our observations are in line with lifetime gradients reported in other locations (Brown et al., 2007a, b).

Another possible explanation for observed gradients in N_2O_5 would be gradients in O_3 . We first discussed the source rate of N_2O_5 in chapter 4, but briefly, the source rate is defined as $k_1[\text{NO}_2][\text{O}_3]$. Surface deposition of O_3 or diminished boundary layer mixing could result in vertical gradients of O_3 . Helmig et al. (2007) report the common occurrence of vertical gradients in O_3 above the snow pack at Summit, Greenland, where 10 m O_3 levels can be 1 to 9 ppbv higher than at 0.5 m. Simple estimations show that a

10% reduction in O_3 (equivalent to about 2.5 ppbv) at 1 m versus 4 m would subsequently decrease the 1 m N_2O_5 source rate by 10%. The decreased source of N_2O_5 at 1 m could potentially explain the N_2O_5 vertical profiles observed in our study. Because we do not have vertically resolved measurements of O_3 and NO_2 , quantification of vertically resolved N_2O_5 source rates is not possible.

Our N_2O_5 profiling observations are consistent with others who have measured N_2O_5 gradients over snow-free surfaces in that they suggest the gradients result from complex interactions between the stratified nighttime atmosphere and the variability in the spatial distribution and the types of N_2O_5 sinks (Geyer et al., 2004; Stutz et al., 2004; Brown, et al., 2007a; b). A more quantitative explanation of the processes governing the establishment of vertical N_2O_5 gradients over ice surfaces would require a more comprehensive suite of chemical, particulate, and meteorological measurements. An inclusive study of this nature would aid in delineating the roles of snow pack and suspended ice particles in nocturnal nitrogen oxide processing. Nevertheless, this study has demonstrated that N_2O_5 is quantifiable as low as 1 m above the snow surface and that high resolution vertical profiling is possible to this same scale. Furthermore, we have demonstrated the presence of N_2O_5 vertical gradients over an established seasonal snow pack.

5.6 References

- Brown, S. S.; Dube, W. P.; Osthoff, H. D.; Wolfe, D. E.; Angevine, W. M.; Ravishankara, A. R., 2007a. High resolution vertical distributions of NO_3 and N_2O_5 through the nocturnal boundary layer. *Atmospheric Chemistry and Physics*, 7, 139-149.
- Brown, S. S.; Dube, W. P.; Osthoff, H. D.; Stutz, J.; Ryerson, T. B.; Wollny, A. G.; Brock, C. A.; Warneke, C.; De Gouw, J. A.; Atlas, E.; Neuman, J. A.; Holloway, J. S.; Lerner, B. M.; Williams, E. J.; Kuster, W. C.; Goldan, P. D.; Angevine, W. M.; Trainer, M.; Fehsenfeld, F. C.; Ravishankara, A. R., 2007b. Vertical profiles in NO_3 and N_2O_5 measured from an aircraft: Results from the NOAA P-3 and surface platforms during the New England Air Quality Study 2004. *Journal of Geophysical Research-Atmospheres*, 112, (D22).
- Finlayson-Pitts, B. J. and J. N. Pitts Jr. (2000), *Chemistry of the Upper and Lower Atmosphere*, 969 pp. Elsevier, New York.
- Fish, D. J.; Shallcross, D. E.; Jones, R. L., 1999. The vertical distribution of NO_3 in the atmospheric boundary layer. *Atmospheric Environment* 33, (5), 687-691.
- Galmarini, S.; Duynkerke, P. G.; deArellano, I. V. G., 1997. Evolution of nitrogen oxide chemistry in the nocturnal boundary layer. *Journal of Applied Meteorology*, 36, (7), 943-957.
- Geyer, A.; Stutz, J., 2004. Vertical profiles of NO_3 , N_2O_5 , O_3 , and NO_x in the nocturnal boundary layer: 2. Model studies on the altitude dependence of composition and chemistry. *Journal of Geophysical Research-Atmospheres*, 109, (D16).
- Helmig, D., Bocquet, F., Cohen, L., and Oltmans, S. J. 2007. Ozone uptake to the polar snowpack at summit, greenland, *Atmospheric Environment*, 41, 5061-5076.
- Stull, R.B. (1988), *An introduction to boundary layer meteorology*, 670 pp., Kluwer Acad., Norwell, MA.
- Stutz, J.; Alicke, B.; Ackermann, R.; Geyer, A.; White, A.; Williams, E., 2004. Vertical profiles of NO_3 , N_2O_5 , O_3 , and NO_x in the nocturnal boundary layer: 1. Observations during the Texas Air Quality Study 2000 (vol 109, art no D12306, 2004). *Journal of Geophysical Research-Atmospheres*, 109, (D16).
- Wayne, R.P. (2000), *Chemistry of atmospheres : an introduction to the chemistry of the atmospheres of earth, the planets, and their satellites*, 775 pp., Oxford University Press, New York.

Chapter 6:

Conclusions and future outlook

6.1 High latitude nocturnal nitrogen oxide oxidation

Global NO_x emissions are not likely to decline appreciably in the foreseeable future due to the fact that fossil fuel combustion is the primary energy source around the world. More likely, because NO_x emissions have a strong correlation with anthropogenic sources, the global distribution and magnitude of NO_x sources will increase for years to come. As NO_x pollution grows in magnitude, it becomes increasingly important to understand the chemical transformations of NO_x and how these transformations serve as inputs to related environmental problems. Nocturnal oxidation of nitrogen oxides, including reactions of NO_3 and N_2O_5 , is one important transformation pathway.

We have described the configuration, operation, and intercomparison-testing of an NO_3 - N_2O_5 field instrument that was developed for probing the nocturnal NO_x oxidation pathway. Additionally, we have demonstrated that the field instrument is capable of capturing the spatial and temporal heterogeneity of NO_3 and N_2O_5 ambient mixing ratios. The instrument was designed to withstand significant fluctuations in temperature and weather and has demonstrated a $2\text{-}\sigma$ detection limit near 2 pptv in 2 s. The performance of our instrument compares well with another instrument with similar capabilities; but due to its light-weight, compact, and inexpensive construction, our instrument has the added advantage of being highly portable. Because of the many desirable features of the instrument, it has proven to be an excellent tool for probing the nocturnal NO_x oxidation pathway during two field campaigns near Fairbanks, AK.

Using the $\text{NO}_3\text{-N}_2\text{O}_5$ instrument to make direct observations in the Fairbanks pollution plume, we have uncovered evidence that ice plays a primary role in removing NO_x , via heterogeneous hydrolysis of N_2O_5 , from the cold, high latitude nighttime atmosphere. Our observations show a strong anticorrelation for N_2O_5 abundance and lifetime when compared to relative humidity with respect to ice ($\text{RH}(\text{ice})$). When the relative humidity with respect to ice is above 100% and ice is likely present, we observe N_2O_5 lifetimes on the order of 6 minutes and suppressed N_2O_5 abundances. Conversely, when ice particles are likely to be absent ($\text{RH}(\text{ice}) < 100\%$) we observe N_2O_5 lifetimes on the order of 20 minutes and elevated N_2O_5 abundances.

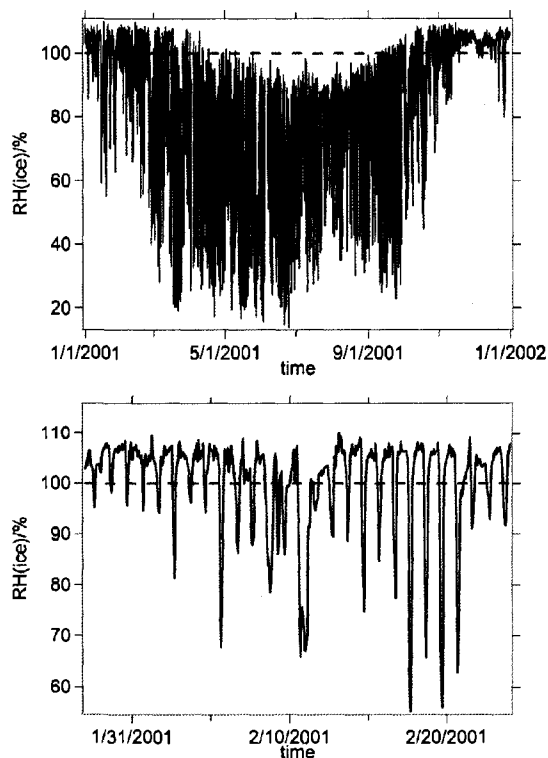


Fig. 6.1 Annual relative humidity with respect to ice in Fairbanks, AK. Top panel: Relative humidity with respect to ice $RH(\text{ice})$ for the year 2001. Data provided by Chapin (2007). From the data available, it is clear that $RH(\text{ice})$ is greater than 100% for the majority of the coldest months of 2001 (January, March, October, November, December). Bottom panel: A blow-up of $RH(\text{ice})$ for a 27 day period in January and February 2001. The bottom trace is colored blue for when the sun is below the horizon and red for when the sun is above the horizon. It is clear that the ice-saturated periods typically coincide with night and the dark NO_x oxidations pathway.

Using data from Chapin et al. (2007), fig. 6.1 shows the relative humidity with respect to ice observed in the Fairbanks airshed for the year 2001. Figure 6 illustrates the possibility that, because $RH(\text{ice})$ is commonly greater than 100%, ice is ubiquitous in the boundary layer during the cold months at high latitudes. Our observations suggest that during these high $RH(\text{ice})$ periods, ice acts as the primary surface for catalyzing heterogeneous hydrolysis of N_2O_5 . The observations implicating ice as catalyzing N_2O_5

heterogeneous hydrolysis are the first of their kind and open up many new questions related to the nocturnal NO_x oxidation process.

One such question pertains to the role played by seasonal snow pack versus suspended ice particles in the removal of N_2O_5 from the nocturnal boundary layer. The hypothesis that the formation of ice particles (due to high $\text{RH}(\text{ice})$) in the atmosphere results in the removal of N_2O_5 does not preclude the snow pack from acting as a similar sink for N_2O_5 . We have presented results from vertical profiling studies that show decreased abundance of N_2O_5 at 1 m above the snow pack as compared to 4 m. This apparent vertical gradient in N_2O_5 would seem to indicate that airmasses in contact with the snow pack lose N_2O_5 via heterogeneous hydrolysis on ice surfaces in the snow. If this were the case, the shortened N_2O_5 lifetimes and diminished N_2O_5 abundances that were observed in high relative humidity airmasses could have resulted from loss to the snow pack instead of loss to suspended ice particles. Clearly, future studies are required to delineate the roles played by suspended ice particles and seasonal snow pack in removing N_2O_5 from cold, nocturnal airmasses.

Future work should include a larger suite of measurements than were included in the studies presented here. The measurements should be aimed at testing the hypothesis that suspended ice particles are present when N_2O_5 lifetimes and abundances are suppressed. Furthermore, emphasis should be placed on confirming that N_2O_5 is lost due to reaction on ice particles. Quantifying a reactive uptake coefficient for N_2O_5 on suspended ice particles, through direct measurements of ice particle count or surface area, would be an ideal test of this hypothesis. Furthermore, considerable effort should be

focused on quantifying the ability of the snow pack to remove N_2O_5 from the atmosphere. Such an effort would include vertical profiling studies with highly resolved vertical ancillary measurements of NO_x , O_3 , wind speed, wind direction, and air temperature. From these data, N_2O_5 deposition fluxes could be estimated and constraints could be placed on the extent to which N_2O_5 is lost to the snow pack.

Lastly, it would be of considerable interest to examine the nocturnal NO_x oxidation process in the Fairbanks pollution plume when temperatures were warm enough to prevent ice from being present in the atmosphere or in the seasonal snow pack. The short N_2O_5 lifetimes that have been reported during these studies with ice present imply that the length-scale of atmospheric nitrogen transport is limited by the formation of NO_N (defined in chapter 4). For example, at 40 ppbv O_3 , 1 atm, and -20°C , the lifetime of NO_2 with respect to the formation of NO_N is approximately 30 hours. Once NO_N forms, based on representative lifetimes discussed in this thesis, it only last for about 10 minutes before being oxidized to HNO_3 . Thus, under cold, snow-covered conditions, NO_x would persist and be transported for essentially 30 hours before being removed from the atmosphere. Using an average wind speed of about 2 m/s, the cold plume would scrub itself of nitrogen (resulting from nocturnal nitrogen oxide oxidation) within about 215 km. In comparison, Brown et al. (2006) have observed N_2O_5 lifetimes in the absence of snow cover that exceed 8 hours. Under these conditions, N_2O_5 can persist through the night and act as a source of NO_x as the sun rises and warms the atmosphere the following day. The end result under these warmer conditions is that atmospheric nitrogen is transported distances much greater than 215 km. Therefore,

capturing seasonal fluctuations in the nocturnal NO_x oxidation process would allow for better quantification of the nitrogen deposition footprint that results from the Fairbanks pollution plume.

In conclusion, gaining insight into the chemistry of nocturnal nitrogen oxides through the application of our $\text{NO}_3\text{-N}_2\text{O}_5$ field instrument, promises to be an exciting and rewarding process far into the future.

6.2 References

Andreas, E. L.; Guest, P. S.; Persson, P. O. G.; Fairall, C. W.; Horts, T. W.; Moritz, R. E.; Semmer, S. R., 2002. Near-surface water vapor over polar sea ice is always near ice saturation. *J. Geophys. Res.*, 107 (C10), 15.

Brown, S. S.; Ryerson, T. B.; Wollny, A. G.; Brock, C. A.; Peltier, R.; Sullivan, A. P.; Weber, R. J.; Dube, W. P.; Trainer, M.; Meagher, J. F.; Fehsenfeld, F. C.; Ravishankara, A. R., 2006. Variability in nocturnal nitrogen oxide processing and its role in regional air quality. *Science*, 311, (5757), 67-70.

Chapin, F.S. 2007. Bonanza Creek Experimental Forest: Hourly Relative Humidity (mean, min, max) at 50 cm and 150 cm from 1988 to Present. Fairbanks, AK: Bonanza Creek LTER Database:BNZD:241.

http://www.lter.uaf.edu/data_detail.cfm?datafile_pkey=241; NSF awards DEB-0620579, DEB-0423442, DEB-0080609, DEB-9810217, DEB- 9211769, DEB-8702629 and USDA Forest Service, Pacific Northwest Research Station RJVA-PNW-01-JV-11261952-231.

Appendix A:**Off-axis cavity ring-down spectroscopy: Application to atmospheric nitrate radical detection¹****Abstract:**

Nitrate radical (NO_3) is detected for the first time using off-axis cavity ring-down spectroscopy (oa-CRDS) with a room-temperature cw diode laser operating near 662 nm. A prototype instrument was constructed and achieved a $1\text{-}\sigma$ absorption sensitivity of $5 \times 10^{-10} \text{ cm}^{-1} \text{ Hz}^{-1/2}$, corresponding to a 1.4 pptv $2\text{-}\sigma$ detection limit in 4.6 seconds at 80 °C. This sensitivity is a significant improvement over a recent implementation of off-axis cavity-enhanced absorption spectroscopy (oa-CEAS) and comparable to that of the most advanced continuous-wave CRDS (cw-CRDS) and pulsed CRDS applications for atmospheric detection of NO_3 . A comparison of measurements of ambient air in Fairbanks, AK recorded using the oa-CRDS instrument and a previously characterized conventional cw-CRDS instrument showed very good agreement ($R^2 = 0.97$).

Ayers, J. D., Apodaca, R. L., Simpson, W. R., and Baer, D. S., 2005. Off-axis cavity ringdown spectroscopy: Application to atmospheric nitrate radical detection, *Applied Optics*, 44, 7239-7242.

Cavity ring-down spectroscopy (CRDS) and variant techniques are a promising new technologies for measuring atmospheric absorbers in field situations. The sensitivity of CRDS and its ability to quantify gases at low concentrations have been known since its inception¹. This high sensitivity is achieved by increasing sample path length with a multi-reflection cell and using a temporal-domain measurement that is insensitive to intensity variations of the light source. CRDS has become increasingly popular in atmospheric applications^{2, 3}, both to detect products in laboratory atmospheric kinetics studies and to measure trace gas concentrations in field applications.

Nitrate radical (NO_3) and dinitrogen pentoxide (N_2O_5) are two molecules recently measured with CRDS. Strong electronic absorption transitions at 662 nm ($\sigma = 2.18 \times 10^{17}$ $\text{cm}^2/\text{molecule}$ at 662 nm and 298 K)⁴ permit detection of NO_3 using optical spectroscopy techniques. Thermal dissociation of N_2O_5 (to form NO_3) has been utilized in a heated flow cell to detect this previously undetected species. Instruments have been developed and field-deployed to detect these species using both pulsed⁵ and continuous-wave⁶ CRDS techniques. Additionally, studies of NO_3 in the lab have been conducted using cavity enhanced absorption spectroscopy (CEAS)⁷ and broadband cavity ring-down spectroscopy⁸, two new variations of the CRDS technique. Here we demonstrate the first application of oa-CRDS to the detection of NO_3 and N_2O_5 in ambient air.

The most mature high-finesse cavity absorption spectroscopy for detection of atmospheric absorbers is cavity ring-down spectroscopy. CRDS uses either pulsed or continuous wave sources and requires spatial and spectral mode matching of the laser light with the optical cavity for reliable time-domain absorbance measurements. The

technique is promising for use in atmospheric field work; however, it is not without disadvantages. Pulsed CRDS laser systems are typically larger and require more power than modern diode lasers. Continuous-wave CRDS systems can use small, portable diode lasers but require rigorous vibration isolation and temperature stability to operate with high sensitivity. These limitations for both techniques pose engineering challenges for field deployment. Integrated cavity output spectroscopy (ICOS, also called CEAS)^{9, 10} retains the high finesse cavity for pathlength extension but instead uses an intensity-domain measurement. For ICOS measurements, in general, the signal to noise ratio of the measured steady-state transmission is limited by excessive cavity resonances.

Off-axis alignment can be used in conjunction with ICOS to increase the reentrant length and produce a denser cavity mode structure. For a laser with a sufficiently broad spectral bandwidth, a reentrant length greater than the laser coherence length can be achieved, and the interference in the cavity becomes statistical rather than coherent. The result is cavity transmission that is quasi-independent of wavelength, albeit with a substantially reduced throughput intensity. Off-axis ICOS reduces the sensitivity to vibration and temperature and can employ small, power-efficient lasers. However, instabilities in light source intensity may decrease the signal-to-noise.

In this letter, we report recent demonstrations of oa-CRDS-based instrument for N_2O_5 and NO_3 measurement. This technique retains the temporal domain ring-down measurement of CRDS but couples the light into the cavity in an off axis fashion to reduce the mode-matching requirements on cavity alignment. High data rates can be maintained because there is no need to couple light actively into a single cavity mode, as

is required in CRDS. In the current work, the data repetition rate is limited only by the ring-down time of the cavity. Small, portable diode lasers and small, high-sensitivity detectors improve instrument portability. Less restrictive alignment requirements facilitate operation in a vibration-rich environment that might be encountered in field work (for example, on board aircraft).

Our apparatus for measuring nitrate radical using oa-CRDS is depicted in Fig. 1. Light at 662 nm from a diode laser (Power Technologies) was directed into a 66-cm long optical cavity consisting of two highly reflective mirrors ($R > 0.99995$ at 662 nm, Los Gatos Research). The output of the cavity was collected by an aspheric lens ($f = 2$ cm) and directed into a photomultiplier tube (Hamamatsu). The output of the photomultiplier was digitized (at a 5 megasample s^{-1} sampling rate) using a 12-bit Gage 1250 Compuscope card mounted in a personal computer. The computer also controlled the diode laser operation through a data acquisition and control card (NI PCI-6023E) that modulated the laser output intensity on-off repetitively at a 500-Hz rate. Baseline ring-down times were on the order of 130 μs . A straightforward alignment procedure was used⁹.

Sampling of ambient air (at 8 slpm flow rate) was accomplished through a measurement cell constructed of 1" steel tubing (2.39 cm ID) coated with halocarbon wax (Halocarbon Corp.) as shown in Fig. 1. The cavity mirrors were mounted on the two ends of the cell. The mirrors were adjusted using o-ring mounts and 3 fine pitched screws. The sample gas first flowed through a Teflon filter to remove particulate matter. New filters were installed before each night of measurement to reduce NO_3 and N_2O_5

losses through possibly dirty filters. This gas then flowed through a heated inlet (95 °C) for 30 cm, then through the optical cavity. The mirrors were purged with 200 sccm house air filtered for particles with a HEPA filter (Gellman Sciences 12144). The main flow cell was heated to 85 °C to allow detection of N_2O_5 , which dissociates stoichiometrically to form NO_3 at this temperature. Sample gas residence time in the instrument was 4 seconds. Nitric oxide (NO) was added to the flow for a 40 second period out of every 160 seconds so that the mixing ratio of NO is 50 ppbv. Because NO reacts with NO_3 quickly to remove it from the flow, this “chemical zero” was used to provide a baseline ring-down time.

This instrument is compared to one using an external cavity diode laser and cw-CRDS described in detail by Simpson⁶. Both instances used heated cells to detect the sum of NO_3 and N_2O_5 as NO_3 in the cavity. The two instruments differ in several important ways. First, oa-CRDS samples a significantly larger portion of the flow cell than cw-CRDS, which samples only the axis of the flow cell. The sampling area can be estimated by observing the size of the light exiting the optical cavity. The cross sectional area of light exiting the oa-CRDS instrument is 100 mm², whereas the cw-CRDS instrument spot size is on the order of 1 mm². Second, in an effort to simplify assembly, the flow cell was constructed using standard tubing with conflat flanges. This change unfortunately increased turbulence in the cell and thus the increased possibility of wall losses.

The two instruments sampled outdoor air for two weeks through ports at the International Arctic Research Center in Fairbanks, AK. NO_3 was detected on three

nights. Fig. 2 shows a time-series plot of these measurements. All data are averaged to a 5 minute time resolution for comparison. High noise on the cw-CRDS instrument was caused by temperature fluctuations in the lab of 4 °C. The off axis instrument was only marginally affected by these temperature variations. Agreement of measurements between the two instruments is outstanding and is illustrated in the correlation plot in Fig. 3. A correlation R^2 value of 0.97 with a slope of 1.01 ± 0.02 shows that the two instruments agree within experimental uncertainty.

The noise-equivalent optical sensitivity of our prototype instrument is estimated using²

$$\alpha_{\min} = \frac{L}{L_{\text{abs}} c} \frac{\Delta\tau_{\min}}{\tau_0^2}, \quad (1)$$

where α_{\min} is the minimum detectable absorbance, L is the cavity length, L_{abs} is the length of the cavity filled with absorber, τ_0 is the baseline ring-down time, and $\Delta\tau_{\min}$ is the smallest measurable difference between τ and τ_0 . We estimate $\Delta\tau_{\min}$ to be the 2- σ uncertainty in the measure of τ_0 times $2^{1/2}$. Using this formalism, the 2- σ sensitivity of the oa-CRDS instrument is $1.0 \times 10^{-9} \text{ cm}^{-1} \text{ Hz}^{-1/2}$ (for $\Delta\tau_{\min} = 4.95 \text{ } \mu\text{s}$, $\tau_0 = 130 \text{ } \mu\text{s}$, $L/L_{\text{abs}} = 1.2$, 500 Hz data rate), comparable to other instruments using traditional CRDS. The noise-equivalent detection limit is calculated by multiplying the minimum optical absorbance by the absorption cross section of NO_3 at the cell operation temperature. For operation at 80 °C (NO_3 cross section estimated to be $1.7 \times 10^{-17} \text{ cm}^2/\text{molec}$), we obtain a 2- σ detection limit of $2.9 \times 10^7 \text{ molecules cm}^{-3}$ (1.4 pptv at 1 atm, 80 °C) in 4.6 seconds.

This detection limit is more than two orders of magnitude lower than the reported 1- σ noise-equivalent detection limit using off-axis CEAS in Ref. 7 (5.5×10^9 molecules cm^{-3} in 3 seconds), highlighting the future promise of oa-CRDS in NO_3 detection. Similar performance calculations for two field-deployed CRDS instruments yielded 2- σ detection limits of 1.6 pptv in 25 seconds (cw-CRDS)⁶ and 0.5 pptv in 5 seconds (pulsed CRDS)⁵. Preliminary static cell measurements at room temperature using oa-CRDS have achieved noise statistics a factor of three lower than reported here, although these changes have not yet been implemented or tested under field operation conditions. The simplicity of this instrument permits excellent performance without significant engineering and makes oa-CRDS an ideal candidate for future field studies.

In conclusion, we have demonstrated that off-axis cavity ring-down spectroscopy can be used to detect ambient NO_3 and N_2O_5 with high sensitivity. We compared the performance of the new oa-CRDS instrument to a previously characterized cw-CRDS instrument and found that the two measurements agree within the instrumental uncertainty. The simplicity of the off-axis ring-down technique is promising for applications in atmospheric field studies in which simple alignment, small size, insensitivity to vibration, and low power consumption are critical features.

We would like to acknowledge funding under NSF grant CHE-0094038 and DOE SBIR grant DE-FG02-03ER83695.

References

- A. O'Keefe and D. A. G. Deacon, "Cavity Ring-Down Optical Spectrometer For Absorption-Measurements Using Pulsed Laser Sources," *Rev. Sci. Instrum.* 59(12), 2544-2551 (1988).
- S. S. Brown, "Absorption spectroscopy in high-finesse cavities for atmospheric studies," *Chem. Rev.* 103(12), 5219-5238 (2003).
- D. B. Atkinson, "Solving chemical problems of environmental importance using cavity ring-down spectroscopy," *Analyst* 128, 117-125 (2003).
- J. Orphal, C. E. Fellows, and P. M. Flaud, "The visible absorption spectrum of NO₃ measured by high-resolution Fourier transform spectroscopy," *J. Geophys. Res.* 108(D3), 4077 (2003).
- S. S. Brown, H. Stark, S. J. Ciciora, R. J. McLaughlin, and A. R. Ravishankara, "Simultaneous in situ detection of atmospheric NO₃ and N₂O₅ via cavity ring-down spectroscopy," *Rev. Sci. Instrum.* 73(9), 3291-3301 (2002).
- W. R. Simpson, "Continuous wave cavity ring-down spectroscopy applied to in situ detection of dinitrogen pentoxide (N₂O₅)," *Rev. Sci. Instrum.* 74(7), 3442-3452 (2003).
- V. L. Kasyutich, C. E. Canosa-Mas, C. Pfrang, S. Vaughan, and R. P. Wayne, "Off-axis continuous-wave cavity-enhanced absorption spectroscopy of narrow-band and broadband absorbers using red diode lasers," *Appl. Phys. B* 75(6-7), 755-761 (2002).
- S. M. Ball, J. M. Langridge, and R. L. Jones, "Broadband cavity enhanced absorption spectroscopy using light emitting diodes," *Chem. Phys. Lett.* 398(1-3), 68-74 (2004).
- J. B. Paul, L. Lapson, and J. G. Anderson, "Ultrasensitive absorption spectroscopy with a high-finesse optical cavity and off-axis alignment," *Appl. Opt.* 40(27), 4904-4910 (2001).
- R. Engeln, G. Berden, R. Peeters, and G. Meijer, "Cavity enhanced absorption and cavity enhanced magnetic rotation spectroscopy," *Rev. Sci. Instrum.* 69(11), 3763-3769 (1998).

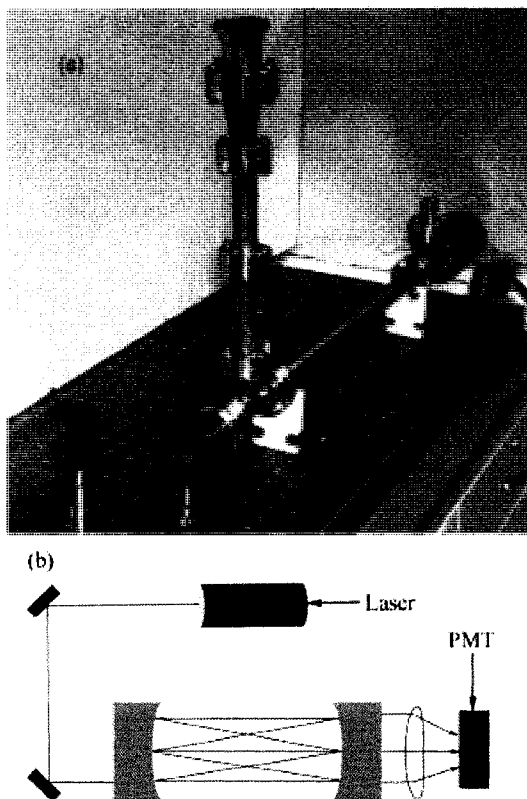
Figures

Fig. 1. (a) A photograph of the off-axis CRDS instrument. (b) A schematic of instrument, showing laser light entering the high-finesse cavity off axis. The cavity output light is focused onto a photomultiplier tube by an aspheric lens.

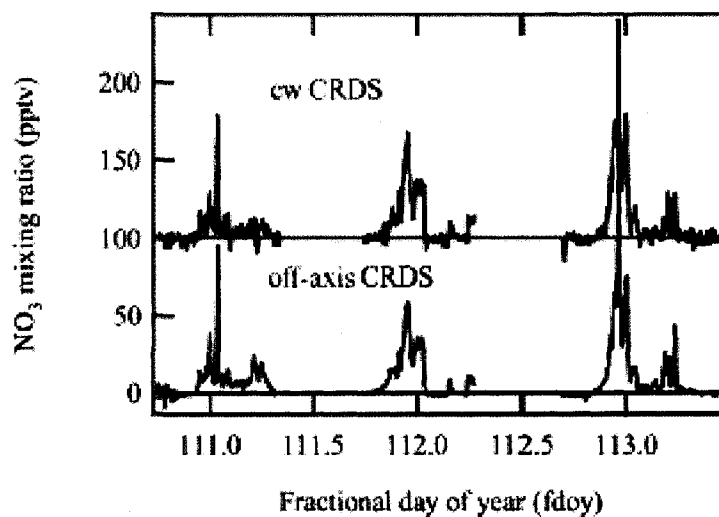


Fig. 2. Measured $\text{NO}_3+\text{N}_2\text{O}_5$ mixing ratios as a function of time (given in fractional day of year, noon 1 Jan 05 AKDT = fday 1.50). The top trace represents the cw-CRDS implementation, while the bottom trace represents the oa-CRDS. The top trace is offset 100 pptv with respect to the bottom trace for clarity. Excellent agreement between the three nights' data is observed.

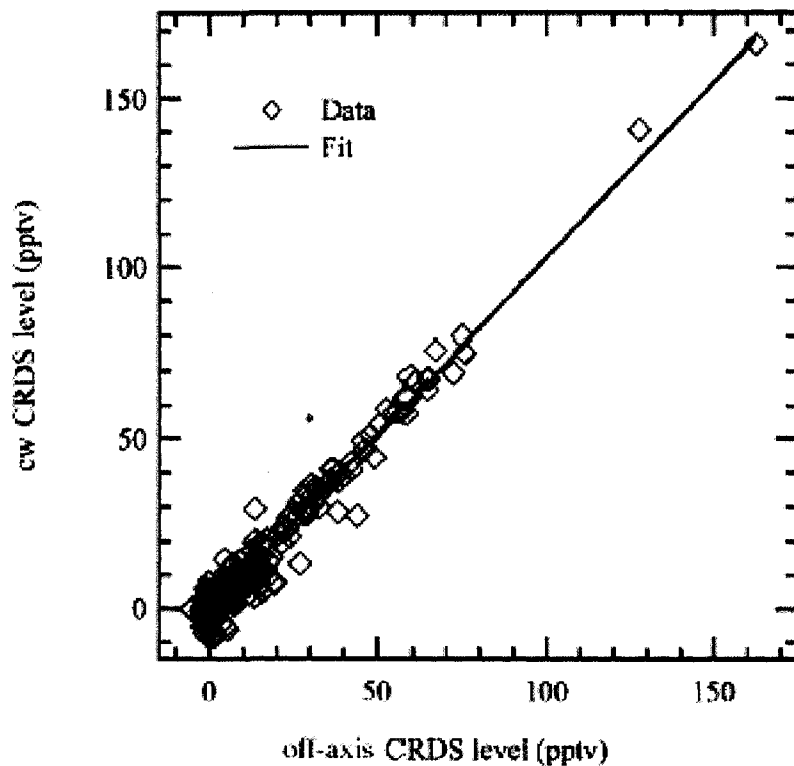


Fig. 3. Correlation between measurements made with oa-CRDS (bottom axis) and cw-CRDS (left axis). The linear regression fit gives $y = 1.01x - 0.85$ pptv, where y is the mixing ratio given by the cw-CRDS instrument, and x is the mixing ratio of the new oa-CRDS instrument. The correlation coefficient $R^2 = 0.97$.

July 30, 2008

To whom it may concern,

I give Randy Apodaca permission to include the below referenced manuscripts as a chapters in his Ph.D. dissertation. Furthermore, I give ProQuest Information and Learning permission to supply copies on demand.

Apodaca, R.L.; D.M. Huff; W.R. Simpson. The role of ice in N_2O_5 heterogeneous hydrolysis at high latitudes. Atmos. Chem. Phys. Discuss., 8, 1–30, 2008.

Ayers, J. D., Apodaca, R. L., Simpson, W. R., and Baer, D. S., 2005. Off-axis cavity ring-down spectroscopy: Application to atmospheric nitrate radical detection, Applied Optics, 44, 7239-7242.

Sincerely,



William R. Simpson

July 28, 2008

To whom it may concern,

I give Randy Apodaca permission to include the below referenced manuscript as a chapter in his Ph.D. dissertation. Furthermore, I give ProQuest Information and Learning permission to supply copies on demand.

Apodaca, R.L.; D.M. Huff; W.R. Simpson. The role of ice in N_2O_5 heterogeneous hydrolysis at high latitudes. *Atmos. Chem. Phys. Discuss.*, 8, 1–30, 2008.

Sincerely,

A handwritten signature in black ink, appearing to read "D. Huff", with a long horizontal flourish extending to the right.

Deanna M. Huff



Randy Apodaca <randy.apodaca@gmail.com>

permission

1 message

Douglas Baer <d.baer@lgrinc.com>

Wed, Jul 30, 2008 at 12:03 AM

To: Randy Apodaca <randy.apodaca@gmail.com>

To whom it may concern,

I give Randy Apodaca permission to include the referenced manuscript in his Ph.D. dissertation.
Furthermore, I give ProQuest Information and Learning permission to supply copies on demand.

Ayers, J. D., Apodaca, R. L., Simpson, W. R., and Baer, D. S., 2005. Off-axis cavity ring-down spectroscopy: Application to atmospheric nitrate radical detection, Applied Optics, 44, 7239-7242.

Sincerely,

Douglas S. Baer
President
Los Gatos Research



Randy Apodaca <randy.apodaca@gmail.com>

Urgent: Author permission

James Ayers <jayers@mesastate.edu>
To: randy.apodaca@gmail.com

Wed, Jul 30, 2008 at 3:37 AM

Hi Randy- Here is the permission letter as requested.

james

James D. Ayers
Assistant Professor of Chemistry
Mesa State College
Grand Junction, CO 81501

To whom it may concern,

I give Randy Apodaca permission to include the referenced manuscript in his Ph.D. dissertation.
Furthermore, I give ProQuest Information and Learning permission to supply copies on demand.

Ayers, J. D., Apodaca, R. L., Simpson, W. R., and Baer, D. S., 2005. Off-axis cavity ring-down spectroscopy: Application to atmospheric nitrate radical detection, *Applied Optics*, 44, 7239-7242.

Sincerely,

7/30/2008 7:39 PM